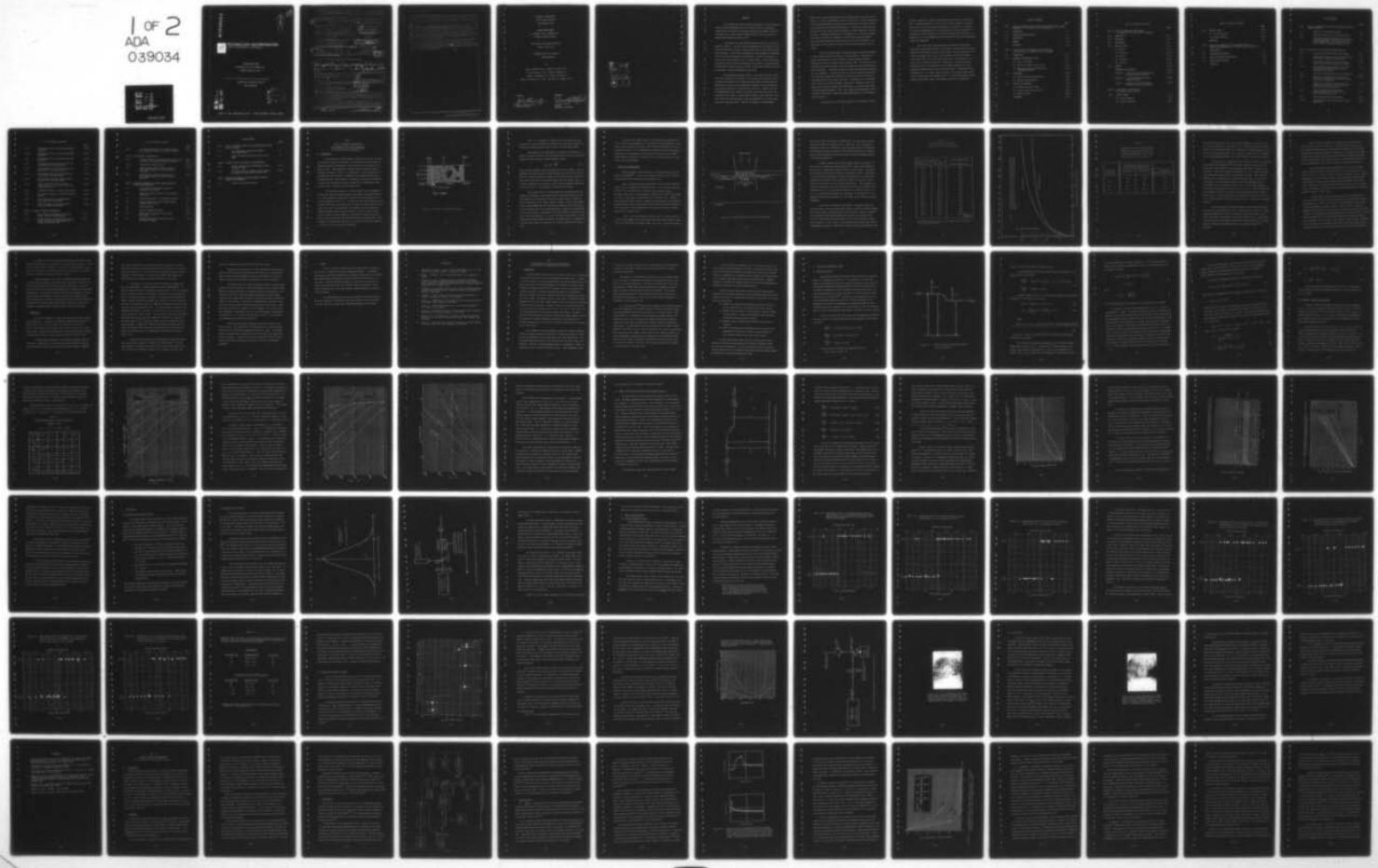
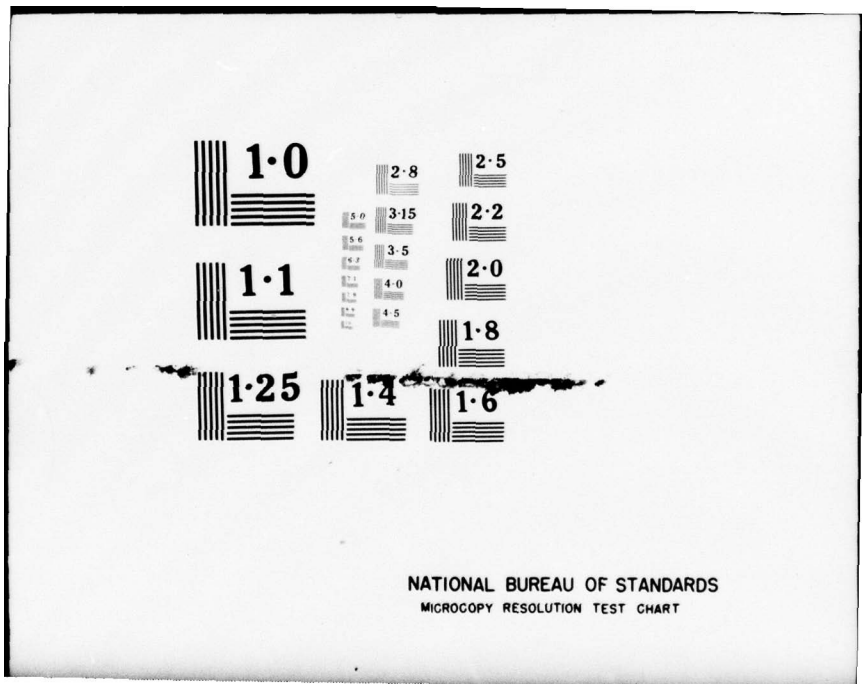
AD-A039 034 TECHNOLOGY INC SAN ANTONIO TEX LIFE SCIENCES DIV F/G 6/18
RESEARCH ON THE OCULAR EFFECTS OF LASER RADIATION.(U)
FEB 75 J S CONNOLLY, J A ZUCLICH F41609-73-C-0017
UNCLASSIFIED TI-75-0561-02 NL

1 OF 2
ADA
039034




1·0
2·8
2·5
3·15
2·2
3·5
2·0
4·0
4·5
1·8
1·1
1·25
1·4
1·6
NATIONAL BUREAU OF STANDARDS
MICROCOPY RESOLUTION TEST CHART

ADA039034



(1)

TECHNOLOGY INCORPORATED

LIFE SCIENCES DIVISION

SECOND ANNUAL REPORT

16 FEBRUARY 1974 to 15 FEBRUARY 1975

CONTRACT F41608-73-C-0017

Approved for public release; distribution unlimited.

RESEARCH ON THE OCULAR EFFECTS OF LASER RADIATION

AD No. /
DDC FILE COPY

DDC
RECEIVED
MAY 3 197
B

8531 N. NEW BRAUNFELS AVE. • SAN ANTONIO, TEXAS 78217

UNCLASSIFIED

SECURITY CLASSIFICATION OF THIS PAGE (When Data Entered)

REPORT DOCUMENTATION PAGE

READ INSTRUCTIONS BEFORE COMPLETING FORM

1. REPORT NUMBER: Technology Incorporated-75-0561-02
2. GOVT ACCESSION NO.
3. RECIPIENT'S CATALOG NUMBER

4. TITLE (and Subtitle): RESEARCH ON THE OCULAR EFFECTS OF LASER RADIATION.
5. TYPE OF REPORT & PERIOD COVERED: SECOND ANNUAL REPORT, 16 Feb 1974 - 15 Feb 1975
6. PERFORMING ORG. REPORT NUMBER

7. AUTHOR(s): J. S. Connolly, Ph.D.; J. A. Zuclich, Ph.D.; A. D. Mavrocki, Ph.D.; H. W. Hemstreet, Ph.D.; V. E. Sanders, Ph.D.; W. H. Bowie, M.S.
8. CONTRACT OR GRANT NUMBER(s): F41609-73-C-0017

9. PERFORMING ORGANIZATION NAME AND ADDRESS: Technology Incorporated, Life Sciences Division, 8531 N New Braunfels Avenue, San Antonio, Texas 78217
10. PROGRAM ELEMENT, PROJECT, TASK AREA & WORK UNIT NUMBERS: 62202F; 6301-00-34

11. CONTROLLING OFFICE NAME AND ADDRESS: USAF School of Aerospace Medicine (RAL), Aerospace Medical Division (AFSC), Brooks Air Force Base, Texas 78235
12. REPORT DATE: 15 February 1975
13. NUMBER OF PAGES: 137

14. MONITORING AGENCY NAME & ADDRESS (if different from Controlling Office): Rept. no. 2 (Annual) 16 Feb 74 - 15 Feb 75;
15. SECURITY CLASS. (of this report): Unclassified
15a. DECLASSIFICATION/DOWNGRADING SCHEDULE

16. DISTRIBUTION STATEMENT (of this Report)

Approved for public release; distribution unlimited.

John S. Connolly, Joseph A. Zuclich, David A. Mavrocki, Harold W. Hemstreet

17. DISTRIBUTION STATEMENT (of the abstract entered in Block 20, if different from Report)

18. SUPPLEMENTARY NOTES: Virgil E. Sanders

TI-75-0561-02

19. KEY WORDS (Continue on reverse side if necessary and identify by block number)
Laser-induced ocular damage, rhesus monkey
Choroidal blood flow
Wavelength and spot size dependence
Retinal temperature measurement/ocular probe
UV-induced retinal damage

6301

00

20. ABSTRACT (Continue on reverse side if necessary and identify by block number)

This second annual report summarizes research on ocular effects of radiation in five distinct but inter-related research areas. The first deals with experimental verification of theoretical predictions on effects of ocular blood flow on laser-induced retinal burn thresholds.

The second major research effort is concerned with ocular effects of UV laser radiation in the cornea and lens. Continuous wave output from a krypton-ion laser (350.7 and 356.4 nm) produces corneal lesions with an energy dose threshold near 66 J/cm^2 for single-pulse exposures of 10, 30, and 45 sec duration. (Cont.)

DD FORM 1 JAN 73 1473 EDITION OF 1 NOV 65 IS OBSOLETE

401 650

UNCLASSIFIED

SECURITY CLASSIFICATION OF THIS PAGE (When Data Entered)

With amplitude-modulated laser radiation at 2 and 0.5 KHz (50% duty cycle), the threshold is increased to ≈92 J/cm^2; whereas at pulse repetition rates of 25 and 0.5 Hz (also 50% duty cycle), the thresholds are in close agreement with single pulse data.

The third research project involves *in situ* microprobe measurements of laser-induced retinal temperatures in living primates. The approach involves visually-guided, surgical insertion of microthermocouple probes through the sclera in the region of the posterior pole. Preliminary surgical procedures were undertaken and some improvements over previous methods were accomplished.

The fourth part of this report summarizes histological investigations conducted in support of research on ocular effects of laser radiation. Pathology reports on a series of large retinal lesions, for animals sacrificed at 1 hour to 90 days postexposure, are summarized.

Part five of this report summarizes the final results of experiments undertaken to determine the effect of wavelength on retinal damage thresholds induced by laser radiation in the visible region. Data were obtained at four visible wavelengths (647.1, 568.2, 520.8, and 476.2 nm) for both minimal retinal image radii (≈25 μm) and larger spot sizes (≈440 μm radius) at exposure times of 40 msec and 250 msec, respectively.

TECHNOLOGY INCORPORATED

LIFE SCIENCES DIVISION

SAN ANTONIO, TEXAS

SECOND ANNUAL REPORT

16 FEBRUARY 1974 to FEBRUARY 1975

CONTRACT F41609-73-C-0017

USAF School of Aerospace Medicine

Brooks AFB, Texas

"RESEARCH ON THE EYE EFFECTS OF LASER RADIATION"

by

John S. Connolly, Ph.D., Joseph A. Zuclich, Ph.D.,

A. David Nawrocki, Ph.D., William H. Bowie, M.S.,

Ronald F. Lemberger, B.S., John A. Strickford,

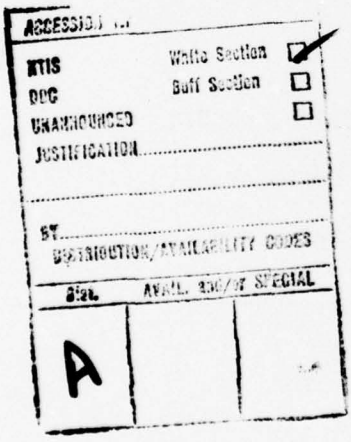
Harold W. Hemstreet, Jr., Ph.D., and Virgil E. Sanders, Ph.D.

Approved:

John S. Connolly, Ph.D.
Research Director

Approved:

T. Gerald Stafford
Manager
San Antonio Laboratory


ACCESSION
NTIS
White Section
DDC
Buff Section
UNANNOUNCED
JUSTIFICATION
BY
DISTRIBUTION/AVAILABILITY CODES
Dist.
AVAIL. and/or SPECIAL
A

ABSTRACT

This second annual report summarizes research on ocular effects of laser radiation conducted by the Life Sciences Division of Technology Incorporated at the School of Aerospace Medicine, USAF SAM/RAL, Brooks Air Force Base, Texas, under Contract F41609-73-C-0017 during the period 16 February 1974 through 15 February 1975.

Five distinct but inter-related research projects are being conducted in parallel. The first deals with experimental verification of theoretical predictions on effects of ocular blood flow on laser-induced retinal burn thresholds. A new surgical procedure has been developed, in collaboration with veterinary surgeons of USAF SAM/VSS, to implant inflatable, occlusive cuffs near the aortic arch of a rhesus monkey. Initial blood flow measurements using fluorescein angiography reveal that this procedure shows a great deal of promise, but final details of this drastic method are yet to be developed. Further experiments are discussed.

The second major research effort is concerned with ocular effects of UV laser radiation, in particular in the corneal and lenticular layers. Continuous wave output from a krypton-ion laser (350.7 and 356.4 nm) produces corneal lesions with an energy dose threshold near 66 Joules/cm^2 for single pulse exposures of 18, 30 and 45 sec duration. However, with amplitude-modulated laser radiation at 2 and 0.5 KHz (50% duty cycle), the threshold is increased to ~92 Joules/cm^2; whereas at pulse repetition rates of 25 and 0.5 Hz (also 50% duty cycle), the thresholds are in close agreement with single pulse data. These results suggest a straightforward

modification of the proposed photochemical damage mechanism involving a short-lived (τ ~ 1-5 msec) intermediate, perhaps a free-radical. Analog computations of the coupled differential equations are presented and the results are shown to be consistent with observed threshold data. In addition we have observed, for the first time, retinal lesions induced by UV laser radiation in the 350 nm region. Preliminary threshold data (10 exposures in a single eye) suggest that retinal lesions can be induced at corneal energy densities somewhat lower than those required to induce lesions in the corneal epithelium. The implications of this finding in terms of existing safety standards are discussed.

The third research project involves in situ microprobe measurements of laser-induced retinal temperatures in living primates. The approach involves visually-guided, surgical insertion of microthermocouple probes through the sclera in the region of the posterior pole. Preliminary surgical procedures have been undertaken and an improvement over previous methods has been accomplished. In addition, design of an improved experimental apparatus has been undertaken. The principal features of this new design include drastic reduction in vibrational instabilities and more precise calibration of laser beam profiles presented at the cornea. Experiments will be conducted over a wide range of laser parameters (power level, repetition rate, pulse-width) and the results compared with predictions of a computer model based on thermal damage mechanisms. Also, direct temperature measurements will be correlated with retinal lesions using both ophthalmological and histopathological criteria.

The fourth part of this report summarizes our histological inves-

tigations conducted in support of research on ocular effects of laser radiation. Pathology reports on a series of large retinal lesions, for animals sacrificed at 1 hour to 90 days post-exposure, are summarized. In addition to retinal histopathology, which is now routine, the first microscopic investigations of laser-induced corneal lesions have now been carried out. The procedures for tissue preparation are described briefly and initial pathology reports are summarized.

Part five of this report summarizes the results of experiments undertaken to determine the effect of wavelength on retinal damage thresholds induced by laser radiation in the visible region. Data were obtained at four visible wavelengths (647.1, 568.2, 520.8 and 476.2 nm) for both minimal retinal image radii (~25 μm) and larger spot sizes (~140 μm radius) at exposure times of 40 msec and 250 msec, respectively. The results show no significant effect of wavelength on retinal damage thresholds, in close agreement with predictions of the IITRI thermal model. Preliminary results (obtained by Dr. V.E. Sanders) were discussed in the previous annual report; since the experiments were completed (by Dr. H.W. Hemstreet) during the term covered by the present report, the complete results are included here.

TABLE OF CONTENTS

		PAGE
PART I - EFFECT OF CHOROIDAL BLOOD FLOW ON LASER-INDUCED RETINAL DAMAGE THRESHOLDS: J.S. Connolly and H.W. Hemstreet, Jr.		
I-A	INTRODUCTION	I-1
I-B	THEORETICAL CONSIDERATIONS	I-4
I-C	EXPERIMENTAL	I-12
I-D	SUMMARY	I-15
	REFERENCES	I-16
PART II - OCULAR EFFECTS OF ULTRAVIOLET LASER RADIATION: J.A. Zuclich, J.S. Connolly and J.A. Strickford		
II-A	INTRODUCTION	II-1
II-B	THEORETICAL PHOTOCHEMICAL MODEL	II-4
	(1) Three Level Scheme	II-4
	(2) Numerical Examples and Discussion	II-9
	(3) Three Level Scheme with Long-Lived Intermediate Species	II-16
II-C	EXPERIMENTAL	II-25
	(1) Subject Preparation and Handling	II-25
	(2) Apparatus and Procedures	II-26
II-D	RESULTS AND DISCUSSION	II-30
	(1) Corneal Epithelial Lesions	II-30
	(2) Stromal and Lenticular Lesions	II-41
	(3) Retinal Lesions	II-43
	REFERENCES	II-52

TABLE OF CONTENTS (continued)

		PAGE
PART III - RETINAL TEMPERATURE MEASUREMENTS: A.D. Nawrocki, W.H. Bowie and R.F. Lemberger		
III-A	INTRODUCTION	III-1
III-B	BACKGROUND	III-1
III-C	EXPERIMENTAL	III-3
III-D	RESULTS TO DATE	III-5
	(1) Thermal	III-5
	(2) Electrical	III-10
	(3) Optical	III-11
	(4) Mechanical	III-15
	(5) Surgical	III-16
III-E	SUMMARY	III-18
	REFERENCES AND FOOTNOTES	III-19
	Appendix A: Limits of Scanner Resolution and Detector System Sensitivity	III-A-1
	Appendix B: Microthermocouple Resistance-Measuring Circuit	III-B-1
	Appendix C: Spatial Filtering of Gaussian Distribution by Finite Detector	III-C-1
PART IV - HISTOLOGICAL INVESTIGATIONS: W.H. Bowie and J.A. Zuclich		
IV-A	RETINAL LESIONS	IV-1
	(1) Tissue Preparation	IV-1
	(2) Retinal Pathology	IV-6

TABLE OF CONTENTS (continued)

		PAGE
IV-B	CORNEAL LESIONS	IV-13
	(1) Tissue Preparation	IV-13
	(2) Corneal Pathology	IV-14
	REFERENCES	IV-17
PART V -	WAVELENGTH DEPENDENCE OF RETINAL DAMAGE INDUCED BY VISIBLE LASER RADIATION: V.E. Sanders and H.W. Hemstreet, Jr.	
V-A	INTRODUCTION	V-1
V-B	EXPERIMENTAL PROCEDURES	V-2
V-C	SUBJECT PREPARATION AND HANDLING	V-12
V-D	RESULTS AND DISCUSSION	V-13
	REFERENCES	V-21

LIST OF FIGURES

		PAGE
PART I - EFFECT OF CHOROIDAL BLOOD FLOW ON LASER-INDUCED RETINAL DAMAGE THRESHOLDS		
I-1	Schematic of Chorioretinal Region	I-2
I-2	Idealized Blood Flow in the Choriocapillaris	I-5
I-3	Calculated Temperature Increases at Center of Retinal Image during 1 Second Exposure. (Retinal image diameter 850 μm; laser power 425 mW at 647.1 nm; depth in pigment epithelium 6 μm).	I-8
PART II - OCULAR EFFECTS OF ULTRAVIOLET LASER RADIATION		
II-1	Three Level Electronic Energy Level Diagram	II-5
II-2	Photoproduct Formation for Various Pulse-Widths as Function of Absorbed Light Intensity	II-11
II-3	Photoproduct Formation for Various Absorbed Light Intensities as Function of Pulse-Width	II-13
II-4	Relative Threshold Intensities as Function of Pulse-Width for Various Assumed Critical Photoproduct Populations	II-14
II-5	Three-Level Scheme with Transient Intermediates	II-17
II-6	Populations of Ground State, Triplet State, Transient Intermediate and Photoproduct Formed by Continuous Irradiation	II-20
II-7	Populations of Transient Intermediate Species Formed by Irradiation Trains of 1-msec and 20-msec Pulses (50% Duty Cycle)	II-22
II-8	Relative Populations of Photoproduct Formed by Irradiation Trains of Various Pulse-Widths (50% Duty Cycle)	II-23
II-9	Typical Beam Scan of UV Laser Output	II-27
II-10	Block Diagram of Laser Apparatus for Corneal Irradiations	II-28

LIST OF FIGURES (continued)

		PAGE
II-11	Dose-Response Plot for 45-second Continuous Exposures	II-32
II-12	Dose-Response Plot for 30-second Continuous Exposures	II-33
II-13	Dose-Response Plot for 18-second Continuous Exposures	II-34
II-14	Dose-Response Plot for 30-second Trains of 1-second Pulses (50% Duty Cycle)	II-36
II-15	Dose-Response Plot for 30-second Trains of 20-msec Pulses (50% Duty Cycle)	II-37
II-16	Dose-Response Plot for 30-second Trains of 1-msec Pulses (50% Duty Cycle)	II-38
II-17	Dose-Response Plot for 30-second Trains of 250-μsec Pulses (50% Duty Cycle)	II-39
II-18	Corneal Epithelial Thresholds (ED_{50}) for Single Pulses and for 30-second Pulse Trains (at 50% Duty Cycle)	II-42
II-19	Transmission Spectra of Rhesus Ocular Media	II-45
II-20	Experimental Apparatus for Inducing UV Retinal Lesions	II-46
II-21	Fundus Photograph of UV-Induced Retinal Lesion; One Hour Post-Exposure	II-47
II-22	Fundus Photograph of UV-Induced Retinal Lesions; 18 Hours Post-Exposure	II-49

PART III - RETINAL TEMPERATURE MEASUREMENTS

III-1	Block Diagram of Experimental System for Retinal Thermal Probe Measurements	III-4
III-2	Thermal Responses of Microthermocouple near Pigment Epithelium of Rhesus Monkey Eye Irradiated with Argon Laser	III-7

LIST OF FIGURES (continued)

		PAGE
III-3	Unit-Normalized Modulus of Frequency Response vs. Frequency for Serially Cascaded RC Stages	III-9
PART IV - HISTOLOGICAL INVESTIGATIONS		
IV-1	Photomicrographs of Suprathreshold Retinal Lesions at Various Time Intervals Following Exposure	IV-8 IV-9
IV-2	Macular Map of Exposure Sites	IV-12
IV-3	Photomicrograph (280x) of Rhesus Cornea 18 Hours after Exposure to UV Laser Radiation (70 J/cm^2)	IV-16
IV-4	Photomicrograph (148x) of Rhesus Cornea 18 Hours after Exposure to UV Laser Radiation (90 J/cm^2)	IV-16
PART V - WAVELENGTH DEPENDENCE OF RETINAL DAMAGE INDUCED BY VISIBLE LASER RADIATION		
V-1	Block Diagram of Experimental Apparatus for Retinal Irradiations	V-4
V-2	Schematic of Optical System for Large Retinal Image Sizes	V-5
V-3	Spatial Distribution of Undiverged Laser Beam	V-6
V-4	Spatial Distribution of Laser Beam Diverged through a Positive Lens	V-7
V-5	Calibrated Probe	V-9
V-6	Exposure Placement in Macula	V-11
V-7	ED_{50} Retinal Thresholds at Four Visible Wavelengths	V-16
V-8	Predicted Temperature Increase in Pigment Epithelium (TI Model)	V-18

LIST OF TABLES

		PAGE
PART I - EFFECT OF CHOROIDAL BLOOD FLOW ON LASER-INDUCED RETINAL DAMAGE THRESHOLDS		
I-1	Peak Temperature Increases Predicted by IITRI Thermal Model	I-7
I-2	Damage Thresholds Predicted by IITRI Thermal Model	I-9
PART II - OCULAR EFFECTS OF ULTRAVIOLET LASER RADIATION		
II-1	Relative Populations of Photoproducts Formed through S_1 State	II-10
II-2	Thresholds (ED50) for Corneal Lesions Induced by Krypton-Ion Laser (350.7 and 356.4 nm)	II-40
PART V - WAVELENGTH DEPENDENCE OF RETINAL DAMAGE INDUCED BY VISIBLE LASER RADIATION		
V-1	Summary of Experimental Results	V-14

PART I

EFFECT OF CHOROIDAL BLOOD FLOW ON LASER-INDUCED RETINAL DAMAGE THRESHOLDS

J.S. Connolly and H.W. Hemstreet, Jr.

A. INTRODUCTION

The production of retinal damage by radiation from lasers and other high intensity light sources emitting in the visible and near infrared has undergone extensive investigation, both theoretical and experimental, for a number of years. Most theoretical treatments have been based on thermal mechanisms of damage, in which it is assumed that a large percentage of the light focused onto the retina is absorbed by the pigment epithelium and is dissipated as heat. Experimentally, the concept of retinal burn thresholds is based on the assumption that when the induced local temperature exceeds a certain level, irreversible tissue damage occurs.

The choroidal vasculature is characterized[1] by an arrangement of arteries and veins which supply and drain the capillary bed (choriocapillaris) located adjacent to the pigment epithelium (PE) and separated from it by Bruch's Membrane (Figure I-1). In contrast to most other anatomical sites, where the arteries and veins branch out by stages into progressively smaller vessels and finally into capillaries, the choroidal vascular system more closely resembles a manifold type structure.[2] That is, the capillaries feed from and drain to the relatively large choroidal arteries and veins, both of which are located on the posterior side of the capillary bed. This structure is evidently more conducive to the high blood flow rates required to fulfill the retina's metabolic requirements.

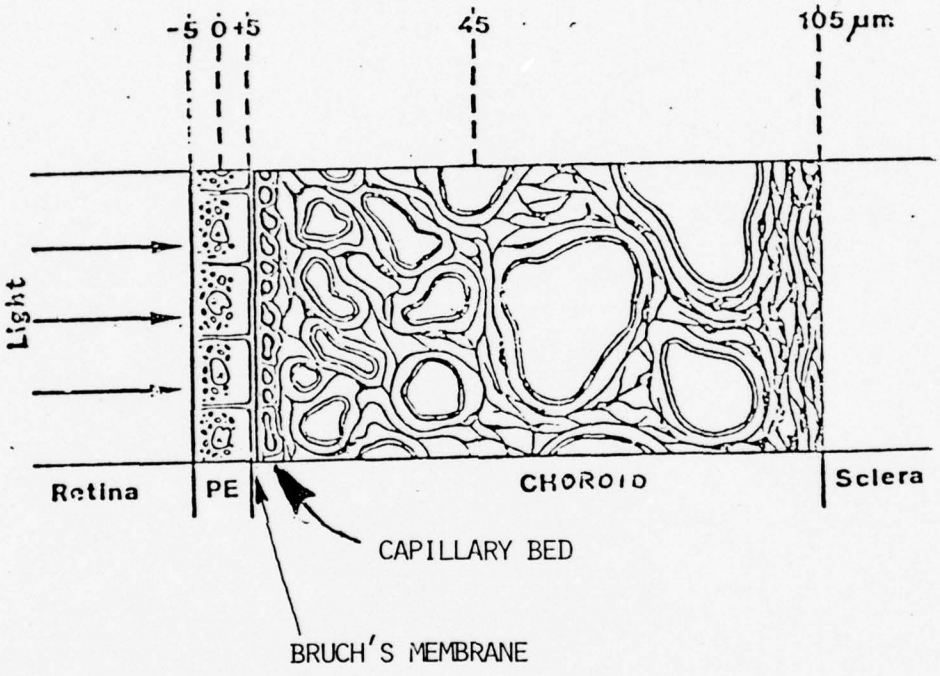


Figure I-1. Schematic of Chorioretinal Region

Thus, it is reasonable to assume that the choriocapillaris can function as a fairly efficient heat exchanger, utilizing forced convection of blood to transport heat from the PE to the large choroidal vessels.

Calculations of the temperatures (T) induced in the retina as a function of space and time (t) are usually performed by numerical solution of the heat diffusion equation in three dimensions namely:

$$\frac{\partial T}{\partial t} = \frac{A}{\rho\sigma} - \frac{K\nabla^2 T}{\rho\sigma} \qquad \text{(I-1)}$$

The two general parameters governing temperature are the geometry- and time-dependent heat source term $A/\rho\sigma$, which represents the rate of heat input to each local volume element of the region; and the heat dissipation term $K/\rho\sigma$, which governs the rate at which heat diffuses into the surround. Here ρ, σ K denote, respectively, the density, specific heat and thermal conductivity of the tissue; and ∇ is the gradient in cylindrical coordinates.

Most thermal models of retinal damage have assumed that the heat induced by irradiation is dissipated solely by the thermal conduction; the contribution to this dissipation from forced convection due to choroidal blood circulation has been largely ignored. However, current thermal models in use at USAF SAM/RAL take into account both conduction and forced convection in removing heat from the irradiated region. Moreover the contribution of convective cooling is implemented in the newer models by simulating blood flow in the choriocapillaris. In effect, the thermal conductivity, K, which determines the rate of heat flow from the irradiated region, is augmented by a factor which reflects the increased rate of heat conduction due to blood flow.

The goal of the present project is to determine the quantitative effect of blood flow experimentally by measuring the retinal thresholds in test animals (rhesus monkeys) with normal blood flow and with temporary occlusion of the ocular arteries. The differences in thresholds measured under the two conditions will be compared with the differences predicted by the IITRI[3] thermal model to determine its reliability in simulating the effect of blood flow on laser-induced damage.

B. THEORETICAL CONSIDERATIONS

Average volumetric blood flow rates in the choriocapillaris of primates are estimated[4-8] to be in the range of 8 to 20 $\mu l\ sec^{-1}\ cm^{-2}$ which is equivalent to blood velocities of 80 to 200 $\mu m\ sec^{-1}$.

Blood is supplied to the choriocapillaris from the larger choroidal arteries and is returned via the choroidal veins. If the principal direction of flow in the choriocapillaris is parallel to the adjacent pigment epithelium layer, then a volume element of blood will flow across the diameter of a 100 μm laser image in approximately 0.5 sec (Figure I-2). However, if the principal direction of flow is assumed to be perpendicular to the pigment epithelium layer, then a volume element from the larger choroidal vessels will flow into and out of the choriocapillaris (a round trip distance of approximately 20 μm) in about 0.1 sec.

Thus, if the approximation of parallel flow is correct, then for a retinal image diameter of 100 μm one would expect the cooling effect of blood flow to be significant for exposure times of $\geq$ 0.5 sec. On the other hand, if

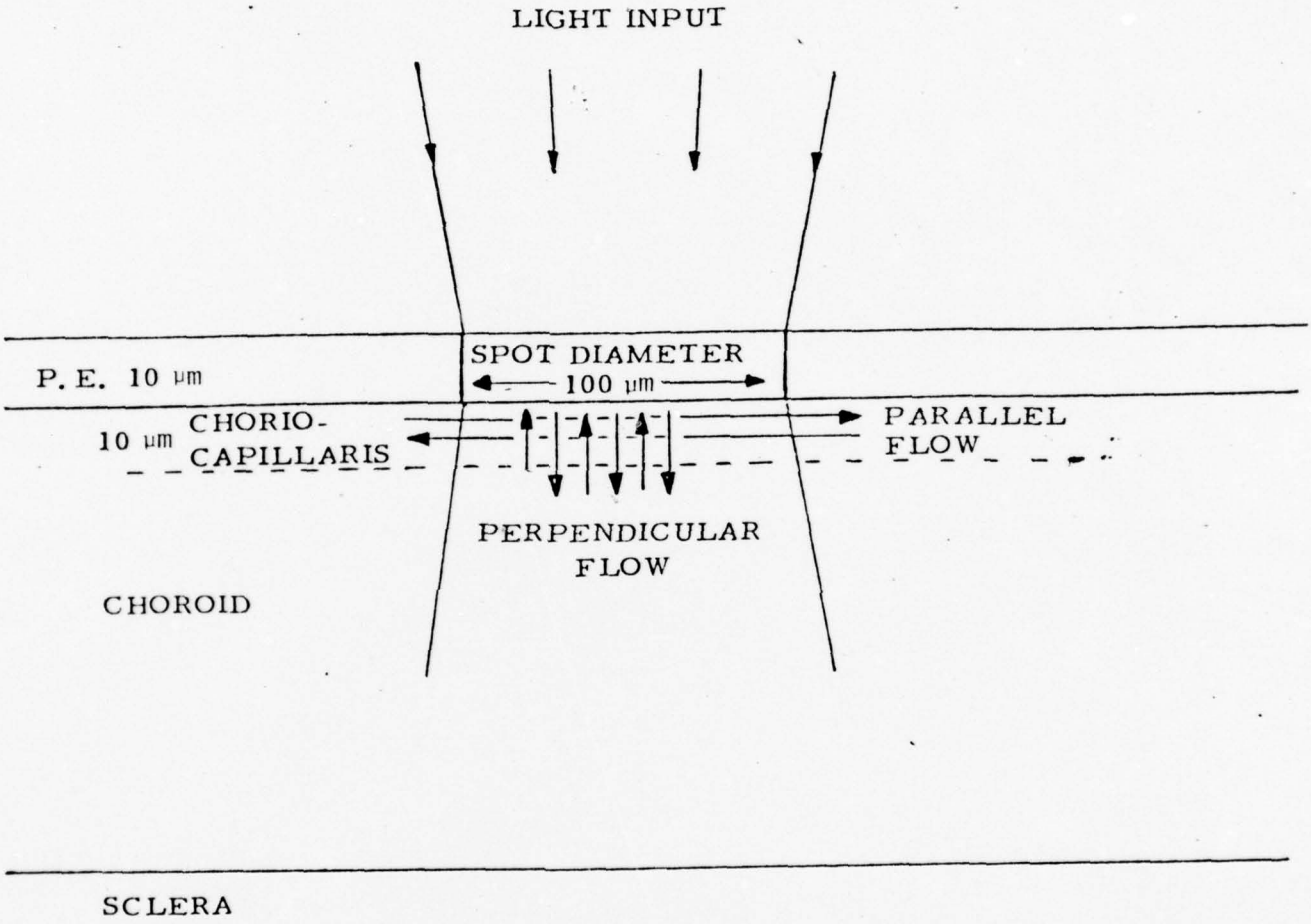


Figure I-2. Idealized Blood Flow in the Choriocapillaris

the principal direction of flow is perpendicular, one would expect a noticeable cooling effect for exposure times as short as 0.1 sec, essentially independent of spot size. Admittedly, these two approximations of choriocapillaris blood flow are overly simplified, but they provide a basis on which to make the above estimates of the exposure times at which the damage threshold is affected by blood flow.

A computer study using the IITRI thermal model was undertaken for the case of a 1-second laser pulse exposure with a retinal image diameter of 850 μm ($1/e^2$); a laser power of 425 mW at 647.1 nm was assumed. The temperature increases predicted by the model are summarized in Table I-1 and Figure I-3, which show the temperature increases at a depth of 6 μm in the pigment epithelium at the center of the retinal laser image as a function of time, both for zero-flow and for normal blood flow conditions. These computer calculations indicate that the relative temperature difference at exposure times shorter than 0.1 sec is less than 10%; whereas in the interval from 0.1 sec to 1.0 sec, the difference becomes more pronounced. At the end of a 1.0 sec exposure, the zero-flow temperature is ~27% higher than the normal blood flow temperature.

In addition to temperature calculations, the computer model also yields estimates of the laser beam power required to induce irreversible damage over various retinal areas under given input conditions. Table I-2 presents the calculated corneal powers required to cause lesions of various radii. The first column lists the lesion radius, R, which is calculated to be maximal at a depth of ~6 μm in the PE. The second and third columns list the calculated powers required to induce that size lesion with and without blood flow;

Table I-1

Peak Temperature Increases

Predicted* by IITRI Thermal Model

Temperature Increase (^{o}C)		Time Elapsed From
No Blood Flow	Blood Flow	Start of Exposure (Sec)
29.9	29.6	.008
36.7	36.0	.012
43.3	42.2	.017
50.0	48.4	.022
60.8	58.1	.033
76.9	72.2	.053
90.0	83.3	.074
103.6	94.3	.102
136.0	118.8	.209
154.7	131.8	.312
168.3	140.6	.418
176.9	148.3	.508
184.9	150.5	.617
192.4	154.6	.749
195.9	156.4	.825
199.3	158.1	.908
202.5	159.7	1.000 (End of Exposure)

*Retinal image diameter 850 m ($1/e^2$); laser power 425 mW at 647.1 nm; depth in PE 6 µm.

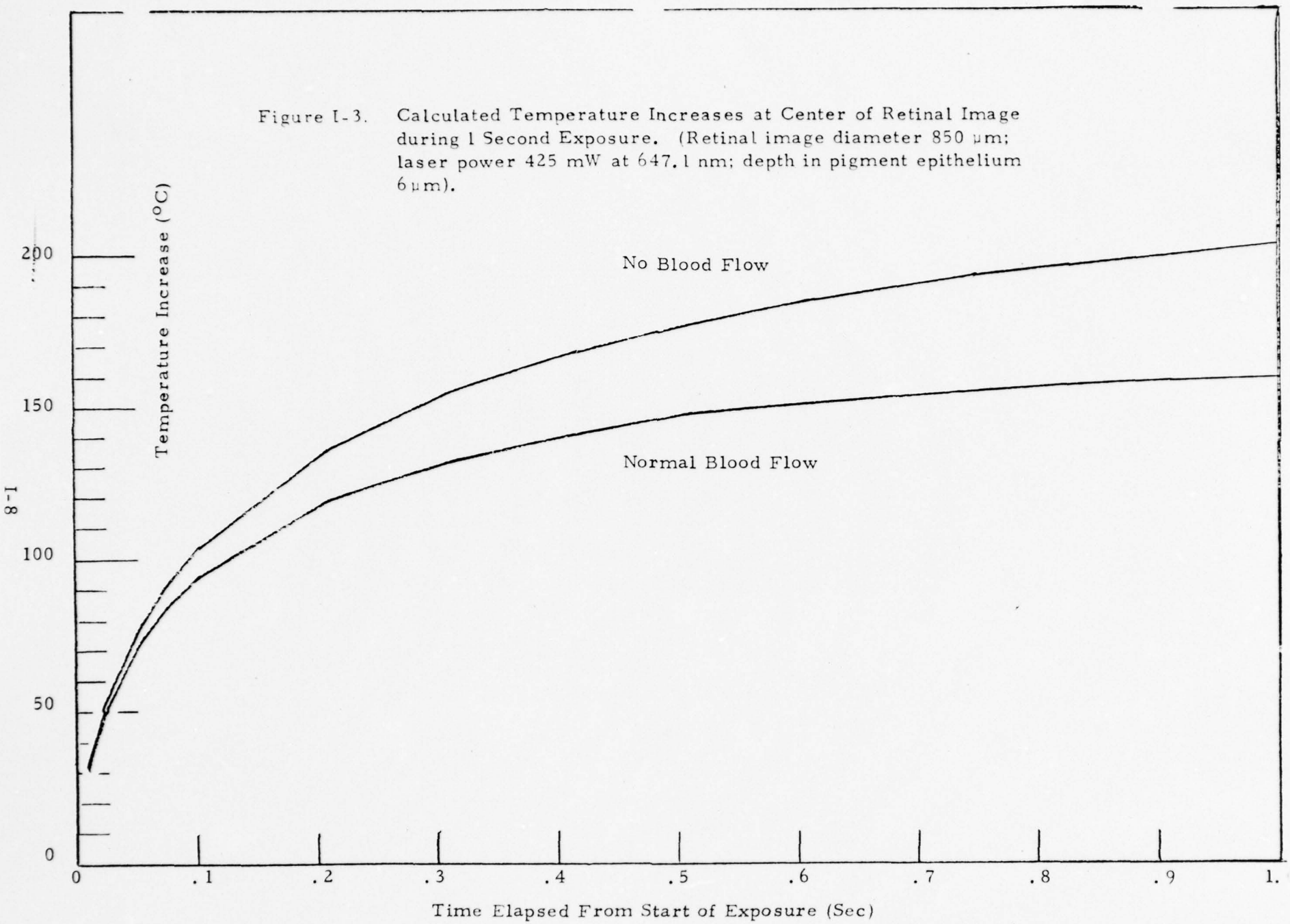


Figure I-3. Calculated Temperature Increases at Center of Retinal Image during 1 Second Exposure. (Retinal image diameter 850 μm; laser power 425 mW at 647.1 nm; depth in pigment epithelium 6 μm).

Table I-2

Damage Thresholds Predicted by IITRI Model for 1 Sec Exposure and 850 μm Retinal Image Diameter ($1/e^2$). Input Laser Power 425 mW at 647.1 nm.

	Laser Power at Cornea (mW) To Cause Irreversible Damage		
Radius of Lesion (μm)	Blood Flow	No Blood Flow	% Difference 100 x (Col. 2-Col. 3)/Col. 3
0	58.7	46.3	26.8
131	71.1	55.7	27.6
262	106	80.8	31.2
394	194	146	32.9

and the fourth column lists the increased power required for normal blood flow over zero flow conditions. Note that at R = 0, the calculated power difference (26.8%) is of the same magnitude as the temperature difference predicted at the end of a 1.0 sec exposure (Table I-1). However for larger lesions, corresponding to suprathreshold conditions, the power differences become more pronounced.

Only one previous experimental study to measure the effect of choroidal blood flow has been undertaken.[9] In this study, the test animals were Chinchilla Grey rabbits rather than rhesus monkeys, which have a different ocular vasculature. Blood flow thresholds were measured in live, anesthetized animals using unfiltered radiation from a high pressure xenon lamp. Zero-blood flow thresholds were then measured by irradiating the same animals 2 to 3 minutes after death. The actual damage evaluations were made ophthalmoscopically approximately 5 to 6 minutes after death. Using a retinal image diameter of 750 μm and various exposure times from 0.08 sec to 2.7 sec, the measured threshold differences, before and after death, decreased markedly for the longer exposure times. At 0.08 sec exposures, the difference was only 14%, but at 2 sec to 2.7 sec the apparent effect of zero-blood flow was a ~58% decrease in damage threshold.

The presumption that the lower thresholds obtained after death were due primarily to zero-ocular blood flow is certainly open to question. Retinal coagulation properties as well as ocular media clarity could change significantly after death. Nevertheless, the trend of these data, i.e., small threshold differences at short exposures progressing to larger differences at longer exposures, suggests a significant effect of blood flow on retinal burn thresholds.

Roulier[10] devised a theoretical thermal model incorporating the cooling effect of choroidal blood flow. His model was based on the usual heat conduction equation which was modified by an additional term to account for heat flow by convection as well as conduction. The convection term (heat transport due to blood flow) was based on the two-fold assumption that blood flow is unidirectional (non-radial) and laminar in the choriocapillaris, and that the distribution of flow rates is Gaussian, decreasing toward the PE.

Since the 3-dimensional heat equation (Eq. I-1) with a spatially-varying energy source term is not easily solved in closed analytic form, the usual practice is to resort to numerical solution by computer. Roulier, however, undertook special case analytic solutions after making several mathematical simplifications. Damage thresholds were empirically derived from the theoretical temperatures obtained both with and without blood flow in his analytic model. He compared his results with the experimental measurements of Geeraets, et al.[9] on Chinchilla Grey rabbits.

Roulier's model predicted significantly smaller threshold differences between normal blood flow and zero-blood flow cases than those observed by Geeraets et al. Roulier had to assume a rather high peak blood flow rate in the choriocapillaris, namely 2 cm/sec, in order to obtain a reasonable agreement with the results of Geeraets et al. Since this flow rate is at least a factor of 100 higher than most estimates given in the literature[4-8], Roulier's theoretical model does not satisfactorily explain the limited experimental data. Moreover, it must be borne in mind that the "zero-flow" data of Geeraets et al. were taken some 5-6 minutes after death of the test subjects and thus the lower thresholds almost certainly reflect factors other than blood flow.

In summary, the role of convective blood flow in the cooling of the retina during and after laser exposures is at present highly uncertain. Since the IITRI thermal model incorporates a simulation of choriocapillaris blood flow, it is important to test the validity and, if necessary, to refine this aspect of the model in light of experimental results.

Thus the purpose of this study is to measure retinal thresholds of live rhesus monkeys exposed to long-pulse laser light under two distinct conditions--normal ocular blood flow and zero-ocular blood flow. In this way the effect of blood flow on damage threshold power or energy can be determined quantitatively. The difference between retinal lesion thresholds with normal blood flow and the thresholds with zero-blood flow can be related to peak retinal temperatures. Both the threshold power increments and the temperature differences can be compared with thermal model predictions to adjust model parameters and provide greater agreement between theory and experiment.

C. EXPERIMENTAL

Our initial attempts to occlude ocular blood flow in rhesus monkeys were unsuccessful. In particular, although the common carotid arteries in these primates are readily accessible, the vertebral arteries are not. Hence, in order physically to occlude arterial flow to the eye, it is necessary to place a suitable constricting device either around the optic nerve and associated blood vessels or around arterial branches of the aortic arch.

The former method employed a loop surgically implanted around the optic nerve. Manipulation of this loop caused excessive motion of the eye, and in one case, the optic nerve and blood vessels were severed. Although

other devices implanted at this location might be successful, the surgical procedure was found to be time-consuming and severely traumatic to the animal, especially to the eyes. It is possible that the surgical procedure might be improved, but severe trauma to the eyes clearly would render suspect any quantitative data on laser burn thresholds obtained in this manner.

Consequently, an alternative surgical procedure was developed by Maj. Earl Jones USAF-VC, a senior veterinary surgeon in USAF SAM VSS. Dr. Jones performed two surgical explorations on acute animals. The first revealed that the vertebral sources of ocular blood are located such that neither temporary nor chronic occlusion is feasible. The second surgical procedure involved a thoracic approach and revealed that collateral flow can be halted by occlusion of the subclavian arteries. Moreover, the carotid arteries are also accessible via the same surgical route. Dr. Jones developed a unique surgical procedure and implanted 3 inflatable, occlusive cuffs on the carotid and subclavian arteries of a rhesus monkey. The post-surgical recovery of the animal was entirely satisfactory and, when recovery was complete (ca. 10 days), an attempt was made to verify occlusion of ocular blood flow employing fluorescein angiography. Conventional fluorescein angiography techniques were employed, first under normal blood flow conditions and then with the cuffs inflated with distilled water, as recommended by the manufacturer (In Vivo Metrics, Inc.).

Examination of the resulting fundus photographs revealed that while ocular flow had been impeded, it clearly had not been stopped. The time-lapse photographs indicated that with the cuffs inflated, the bolus of fluorescein solution was elongated, resulting in the appearance of normal flow

onset but prolonged exit of the dye from the retinal vessels.

Subsequent discussions with Dr. Jones revealed that the most probable cause for lack of total occlusion was that one or more occlusive cuffs was too large (4 mm lumen diameter) or that, when inflated, the cuffs were unable to overcome systolic pressure which may be as high as 160 mm Hg.

Three weeks after the initial angiography studies, a second attempt was made to verify occlusion. By this time sufficient scar tissue had formed between the arteries and cuffs to overcome possible size deficiencies. Test inflation of the cuffs, while the anesthetized subject was being aligned relative to the fundus camera, indicated a significant decrease in the blood supply to ocular muscles. Specifically, immediately upon inflation of the third cuff, the eye showed a marked bilateral movement (down and in). After positioning the animal to compensate for this movement, the occlusive cuffs were reinflated. Unfortunately, one of the cuffs developed a leak resulting in injection of 1-2 cc of water into the thoracic cavity. This experiment was terminated and the animal was sacrificed.

Post-mortem examination confirmed the presence of water in the thoracic cavity. The examination also revealed that scar tissue had compensated for the size deficiency suggested earlier by Dr. Jones. In addition, there was evidence that occlusion of blood flow on that day had induced myocardial infarctions. There was also an older infarction in the left lung, which may have been caused during the course of the earlier angiography experiment.

D. SUMMARY

Clearly, occlusion of blood flow to the upper body of a primate is, at the least, a traumatic and possibly dangerous procedure. If meaningful quantitative data are to be derived from experiments employing such a procedure, the techniques must be developed carefully in order to minimize trauma. In particular, a specific inflation sequence of the occlusive cuffs must be devised, including careful control of inflation timing and pressures. Also, smaller occlusive cuffs (3 mm lumen diameter) should be employed to preclude size deficiencies.

The experimental protocol has been revised to include these factors. After the occlusive cuff method has been tested further to verify occlusion of ocular blood flow, in vivo laser threshold measurements will continue.

REFERENCES

1. Duke-Elder, S. and K. C. Wybar, System of Ophthalmology, Vol. II, "The Anatomy of the Visual System", C.V. Mosby Co. (1961).

2. Wolff, E., Anatomy of the Eye and Orbit, 6th Ed., W.B. Saunders Co. (1968).

3. Takata, A.N., et al., "Thermal Model of Laser-Induced Eye Damage", Illinois Institute of Technology Research Institute, Final Technical Report, Contract No. F41609-74-C-0005, USAF School of Aerospace Medicine, Brooks AFB, Texas (October 1974).

4. Friedman, E., H.H. Kopald, and T.R. Smith, "Retinal and Choroidal Blood Flow Determined with Krypton-85 Anesthetized Animals", Investigative Ophthal. 3, 539 (1964).

5. Friedman, E., and T.R. Smith, "Estimation of Retinal Blood Flow in Animals", Investigative Ophthal. 4, 1122 (1965).

6. Trokel, S., "Measurement of Ocular Blood Flow and Volume by Reflective Densitometry", Arch. Ophth. 71, 88 (1964).

7. Trokel, S., "Effect of Respiratory Gases on Choroidal Hemodynamics", Arch. Ophth. 73, 838 (1965).

8. Trokel, S., "Quantitative Studies of Choroidal Blood Flow by Reflective Densitometry", Investigative Ophth. 4, 1129 (1965).

9. Geeraets, W.J., R.C. Williams, W.T. Ham and D. Guerry, III, "Rate of Blood Flow and Its Effect on Chorioretinal Burns", Arch. Ophthal. 68, 58 (1962).

10. Roulier, A., "Calculation of Temperature Increases in the Eye Produced by Intense Light", Bull. Math. Biophys. 3, 403 (1970).

PART II

OCULAR EFFECTS OF ULTRAVIOLET LASER RADIATION

J.A. Zuclich, J.S. Connolly and J.A. Strickford

A. INTRODUCTION

An investigation into the effects of ultraviolet (UV) laser irradiation on ocular media has been in progress throughout the contract year. A number of UV laser systems are currently commercially available and widespread use of these and systems still under development is anticipated in the near future. Although the inherent sensitivity of biological systems to UV radiation has long been recognized, the safety standards developed for non-coherent UV sources are minimal and did not anticipate the range of parameters associated with laser systems. For example, there is little basis for meaningful safety standards for such situations as high intensity, short pulse-width UV exposures or repetitive-pulse exposures. Therefore, there is a critical need for analyzing the nature of the damage that UV lasers can cause in living matter and for providing guidelines for protection against such damage. The need is especially acute with regard to ocular exposures where grave personnel hazards are created by low damage thresholds coupled with the high potential for accidental exposure due to the victim not having any immediate physical awareness of the exposure.

The UV segment of the electromagnetic spectrum is somewhat arbitrarily divided into three wavelength regions which in common terminology are called the near UV (300-400 nm), far UV (200-300 nm) and vacuum UV(4-200 nm). This investigation deals specifically with ocular hazards from near UV and far UV radiation. Radiation in these wavelength regions is absorbed by a number of chromophoric sites of proteins and nucleic acids. These chromophores belong

to the class of aromatic molecules which are characterized by delocalization or sharing of electrons by several chemical bonds resulting in low-lying electronic energy levels.

The energy of a single photon in the near or far UV wavelength range may be such that it can promote an electron of the absorbing aromatic chromophore to an excited energy level. The resulting excited state of the absorbing molecule is highly labile and the molecule may subsequently engage in a number of chemical reactions with its molecular neighbors. The resulting photo-induced products may be incompatible with the normal functioning of the exposed system and may, in time, lead to some biological damage which is observable on the macroscopic level.

In a previous report[1] the molecular composition and absorption properties of the components of the primate eye were discussed and potential damage sites from 200-400 nm radiation were pointed out. The formulation of a quantitative model for a photochemical damage mechanism was begun through a consideration of the electronic energy level schemes associated with aromatic molecules and the kinetics involved with UV-induced transitions between the energy levels. An approximate solution was presented for the number of photoproducts or "molecular lesions" formed as functions of the laser beam parameters. This solution was valid, however, only in the limits of long pulse-widths, so that the differential equations for the populations of the electronic energy levels could be solved in the steady state and with intensities sufficiently low that only a negligible fraction of the absorbing molecules were promoted to an excited state at any given time.

Realizing that this approximate solution would not suffice for the entire spectrum of beam parameters associated with operational lasers, development of the theoretical model was continued and in this report a general solution is presented for a molecular electronic energy level scheme consisting of a ground state and excited singlet and triplet states. Numerical examples are included to illustrate explicitly the complicated dependence of photoproduct formation on the laser beam parameters.

Although the basic three level electronic energy level scheme is thought to be an adequate representation of the absorbing molecule, the exact formalism to be used for quantitative photochemical predictions in any given case will depend upon:

(1) whether the formation of photoproducts proceeds through the excited singlet state, the excited triplet state or both;

(2) whether the final product is formed directly from one or both excited states or if there are intermediate steps (and hence additional transient species) involved;

(3) whether single or multiple-photon absorption processes are involved;

(4) whether the absorbing species themselves are involved in the photochemical reactions or if there is energy transfer to other molecules which are then the reactive species.

The experimental program being carried out concurrently with the theoretical modeling has been designed to distinguish among the various possibilities outlined above. The results discussed in this report have already answered some of the questions posed above and have provided feedback for modifying and refining the theoretical model.

B. THEORETICAL PHOTOCHEMICAL MODEL

(1) Three Level Scheme

The electronic energy level diagram used to represent the absorbing molecule is reproduced in Figure II-1. The rationale for choosing this energy level scheme was discussed at length in the previous annual report.[1] The possible photochemical reactions which may occur directly from the S_1 or T_1 states are indicated by the rate constants k_s and k_t, respectively. Reactions which may occur only after absorption of a second photon are represented by $C_s(\lambda)I$ and $C_t(\lambda)I$.[1] The remaining rate constants describe the various transitions between energy levels. The rate constants for the photochemical reactions are considered to be negligible compared to these remaining rates and are ignored in the initial solution of the rate equations. They are later re-introduced into the problem as pertubations to the solutions.

If $S_0(t)$, $S_1(t)$ and $T_1(t)$ are taken as the time-dependent populations of the S_0, S_1 and T_1 states, respectively, the rate equations for the populations are:

$$\frac{dS_0(t)}{dt} = -C(\lambda)I\ S_0(t) + k_f\ S_1(t) + k_p\ T_1(t)$$

$$\frac{dS_1(t)}{dt} = C(\lambda)I\ S_0(t) - (k_f + k_c)\ S_1(t) \qquad (1)$$

$$\frac{dT_1(t)}{dt} = k_c S_1(t) - k_p\ T_1(t)$$

At any given time the sum of the populations will be:

$$S_0(t) + S_1(t) + T_1(t) \simeq N^0 \qquad (2)$$

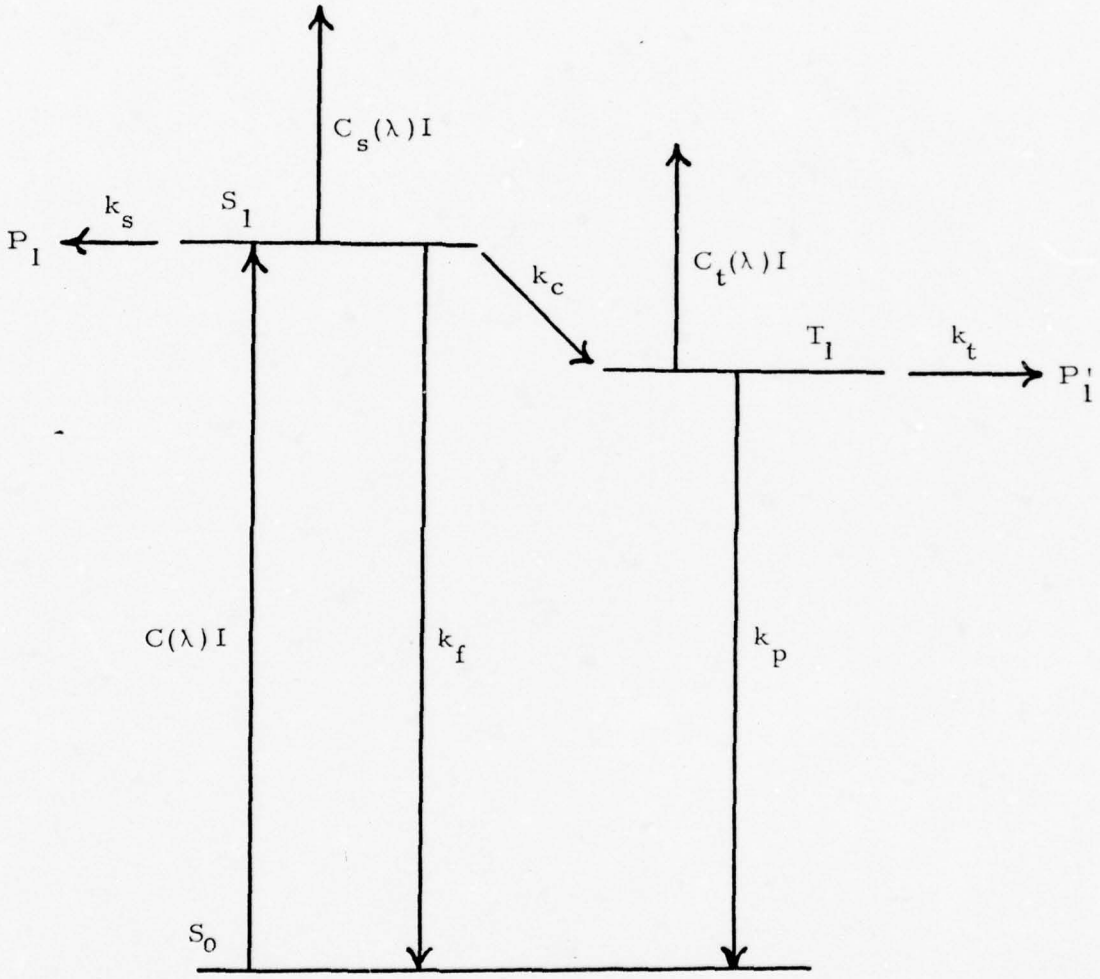


Figure II-1. THREE LEVEL ELECTRONIC ENERGY LEVEL DIAGRAM

where N^o is the total number of absorbing molecules.

This relationship can be used to eliminate one of the variables, say $S_o(t)$, from Eq. (1) to yield:

$$\frac{dS_1(t)}{dt} = C(\lambda)I\, N^o - C(\lambda)I\, T_1(t) - (k_f + k_c + C(\lambda)I)\, S_1(t)$$

$$\frac{dT_1(t)}{dt} = k_c\, S_1(t) - k_p\, T_1(t) \qquad (3)$$

A general solution for Eq. (3) can be found by established mathematical techniques.[2] The result is of the form:

$$S_1(t) = C_1 \exp(\lambda_- t) + C_2 \exp(\lambda_+ t) + m \qquad (4a)$$

$$T_1(t) = \frac{C_1 k_c}{\lambda_+ + k_p} \exp(\lambda_+ t) + \frac{C_2 k_c}{\lambda_- + k_p} \exp(\lambda_- t) + n \qquad (4b)$$

where,

$$\lambda_{\pm} = \frac{-(k_p + k_f + k_c + C(\lambda)I) \pm \sqrt{(k_p + k_f + k_c\, C(\lambda)I)^2 - 4k_c C(\lambda)I - 4k_p(k_f + k_c + C(\lambda)I)}}{2} \qquad (5)$$

and C_1, C_2, m and n are constants which are determined by the boundary conditions of the problem.

With continued irradiation, the populations $S_1(t)$ and $T_1(t)$ approach steady state values S_1^o and T_1^o, respectively, in times comparable to the excited state lifetimes (nanoseconds for S_1 states and microseconds for T_1 states). Thus, for pulse-widths very long compared to the excited state life-

times the populations are treated as constants. It was previously shown, for instance, that the number of photoproducts which may be formed directly from the S_1 state is simply

$$P_1(I,\tau,C(\lambda)) = \int_0^\infty k_s\, S_1(t)\, dt \simeq k_s\, S_1{}^0 \int_0^\tau dt$$

$$\simeq k_s\, S_1{}^0 \tau \tag{6}$$

where

$$S_1{}^0 = m \simeq \frac{C(\lambda) I N^0}{k_f + k_c} \tag{7}$$

in the limit where negligible depletion of the S_0 population is assumed.

In the above case the functional dependence of P_1 on I, τ and $C(\lambda)$ is straightforward. However, in considering the case of shorter pulse-widths the populations do not reach steady state during the course of the irradiation and the time-dependent terms of equations (4a) and (4b) must be integrated to find the populations of the photoproducts. Further, with short-pulse, high-power lasers, some depletion of the ground state population may occur so that this assumption, employed in the derivation of equations (6) and (7), is no longer valid. Finally, for short, high intensity pulses, the number of photoproducts formed after termination of the pulse cannot be neglected, since the excited states will maintain a non-negligible population for several lifetimes after the irradiation. Equations (4a) and (4b) are valid for the time interval $0 \leq t \leq \tau$, but additional expressions must be derived for the time interval $\tau \leq t \leq \infty$.

The applicable differential equations and their solutions are extremely lengthy, hence we present here the solution for only one of the four possible pathways proposed for the photochemical reaction, namely the mechanism for direct production of photoproducts from the S_1 state.

The number of photoproducts formed via this mechanism is given by,

$$P\ (I,\ \tau,\ C(\lambda)) = \int_0^{\tau} k_S\ S_1(t)\ dt + \int_{\tau}^{\infty} k_S\ S_1'(t)\ dt \tag{8}$$

where $S_1(t)$ is the population given in equation (4a) and $S_1'(t)$ is of the form

$$S_1'(t) = C_3 e^{-(k_f + k_c)t} \tag{9}$$

which represents the decay of the S_1 population after the termination of the irradiation. The constant C_3 is determined by equating $S_1(t)$ and $S_1'(t)$ at τ, the instant when the irradiation is terminated. Solving for the constants and carrying out the integrations indicated in Eq. (8) the resulting expression for P_1 is found to be,

$$P_1(I,\tau,C(\lambda)) = k_s\ S_1^{\ o}\ \left[\ \tau + \frac{1}{k_f + k_c} - b_1 e^{\ \lambda_- \tau} + b_2 e^{\ \lambda_+ \tau} + b_3\ \right] \tag{10}$$

where λ_+ and λ_- are given in Eq. (5) and,

$$S_1^{\ o} = \frac{C(\lambda) I N^o}{\frac{k_c}{k_p} C(\lambda) I + k_f + k_c + C(\lambda) I} \tag{11}$$

$$b_1 = \frac{\lambda_+(\lambda_- + k_p)}{k_p(\lambda_+ - \lambda_-)} \left\{ \frac{1}{\lambda_-} + \frac{1}{k_f + k_c} \right\} \tag{12}$$

$$b_2 = \frac{\lambda_-(\lambda_+ + k_p)}{k_p(\lambda_+ - \lambda_-)} \left\{ \frac{1}{\lambda_+} + \frac{1}{k_f + k_c} \right\} \tag{13}$$

and

$$b_3 = \frac{1}{k_p} + \frac{\lambda_+ + \lambda_-}{\lambda_+ \lambda_-} . \tag{14}$$

Similar solutions may be derived for the formation of photoproducts directly from the T_1 state or following absorption of a second photon by the S_1 or T_1 states.

(2) Numerical Examples and Discussion

In order to obtain any meaningful interpretation of the dependence of P_1 on I, τ and $C(\lambda)$ as expressed in Equations (10-14), a number of numerical examples are considered. The singlet state lifetime, $1/kf$, is regarded as an unknown molecular constant as is k_s, the rate constant for photoproduction. The calculated values of P_1 are expressed in units of $\frac{k_s}{k_f} N^o$, where N^o is the total number of absorbing molecules.

The rate constant k_c is set equal to k_f, and k_p is taken to be $10^{-3} k_f$. These relationships are known to be approximately true for each of the aromatic chromophores which absorb UV radiation in biological systems.[3] It is of interest to consider a range of pulse-widths beginning with much longer than the singlet state lifetime and progressing to much shorter than this lifetime. Therefore we consider the cases for τ with values of $10^2/k_f$, $10/kf$, $1/k_f$, $10^{-1}/k_f$ and $10^{-2}/k_f$. Similarly, it is desirable to consider a range of intensities from those which are estimated to be too low to cause any

significant depopulation of the ground state ranging to intensities sufficiently high to cause significant depletion of the ground-state population ($\tilde{>}5\%$). Since the extent of ground state depletion is determined by the relationship between $C(\lambda)I$ and k_f, the limits of interest can be achieved by assigning to $C(\lambda)I$ values of $10^{-2}k_f$, $10^{-1}k_f$, k_f, $10k_f$ and 10^2k_f.

The calculated populations of photoproducts for each set of parameters are shown in Table II-1. The results are also plotted as P_1 vs. $C(\lambda)I$ in Figure II-2 and P_1 vs. τ in Figure II-3. From Figure II-2 it can be seen that for

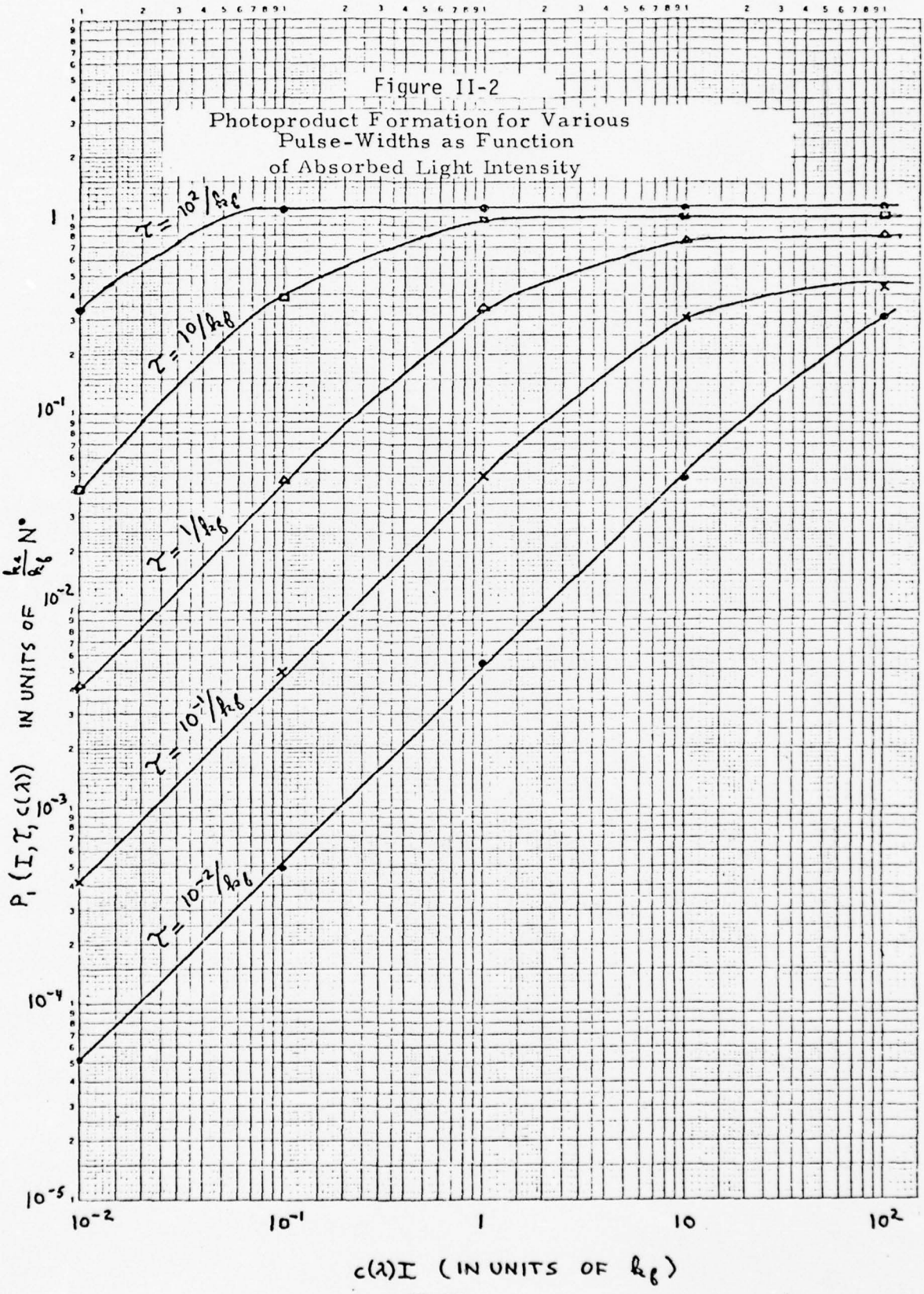
TABLE II-1

RELATIVE POPULATIONS OF PHOTOPRODUCTS FORMED

THROUGH S_1 STATE

$P_1\ (I, \tau, C\ (\lambda)\ )$ in units of $\frac{k_s}{k_f} N^o$

τ \ $C(\lambda)I$	$10^{-2}k_f$	$10^{-1}k_f$	k_f	$10k_f$	10^2k_f
$10^2/k_f$	.34	1.1	1.1	1.1	1.1
$10/k_f$	4.1×10^{-2}	.38	.99	1.0	1.0
$1/k_f$	4.2×10^{-3}	4.7×10^{-2}	.35	.76	.81
$10^{-1}/k_f$	4.2×10^{-4}	4.9×10^{-3}	4.9×10^{-2}	.32	.54
$10^{-2}/k_f$	4.2×10^{-5}	4.9×10^{-4}	$5.5\ 10^{-3}$	4.8×10^{-2}	.32


Figure II-2
Photoproduct Formation for Various
Pulse-Widths as Function
of Absorbed Light Intensity
$\tau = 10^2/k_\beta$
$\tau = 10/k_\beta$
$\tau = 1/k_\beta$
$\tau = 10^{-1}/k_\beta$
$\tau = 10^{-2}/k_\beta$
$P_1(I, \tau, c(\lambda))$ IN UNITS OF $\frac{k_\alpha}{k_\beta} N^\circ$
$c(\lambda)I$ (IN UNITS OF k_β)
1
10^{-1}
10^{-2}
10^{-3}
10^{-4}
10^{-5}
10^{-2}
10^{-1}
1
10
10^2

short pulse-widths P_1 is linearly proportional to $C(\lambda)I$ except at very high intensities where the curves begin to level off. For longer pulse-widths, the curves level off at much lower intensities as the ground state population is depleted and the population of T_1 approaches its steady state value. For sufficiently long τ and high intensity, most of the molecules are "trapped" in the T_1 state, and photoproduct formation from the S_1 state reaches an asymptotic value regardless of further increases in intensity. (This assumes, of course, that no additional damage mechanisms become important.)

From Figure II-3, it can be seen that at low intensities P_1 is linearly proportional to τ for all τ. At higher intensities, however, the curves level off as the population of the T_1 state approaches its steady-state value.

We assume a critical number of photoproducts, P_{1c}, is required in order for cellular aberration (i.e., a lesion) to be observable at the macroscopic level following irradiation. Therefore, a threshold curve is defined as any horizontal line $P_{1c} \equiv P_1$ in Figures II-2 and II-3. In order to derive a plot of threshold intensity, I_{th}, vs. τ it is necessary only to choose the appropriate value of P_{1c} and plot the intersections of this line with the families of curves shown in these figures. Typical results are shown in Figure II-4 for several values of P_{1c}. It is seen that for low values of P_{1c}, I_{th} is linearly proportional to τ with unit slope indicating that the product, τI_{th}, is a constant. This is merely a statement of the usual assumption that the amount of photochemical damage is proportional to the total energy dose. Note, however, that this assumption breaks down for larger values of P_{1c}, i.e., in cases where many photoproducts must be formed before a macroscopic lesion is observable. Note also, that in any case, the

Figure II-3

Photoproduct Formation for Various Absorbed Light Intensities as Function of Pulse-Width

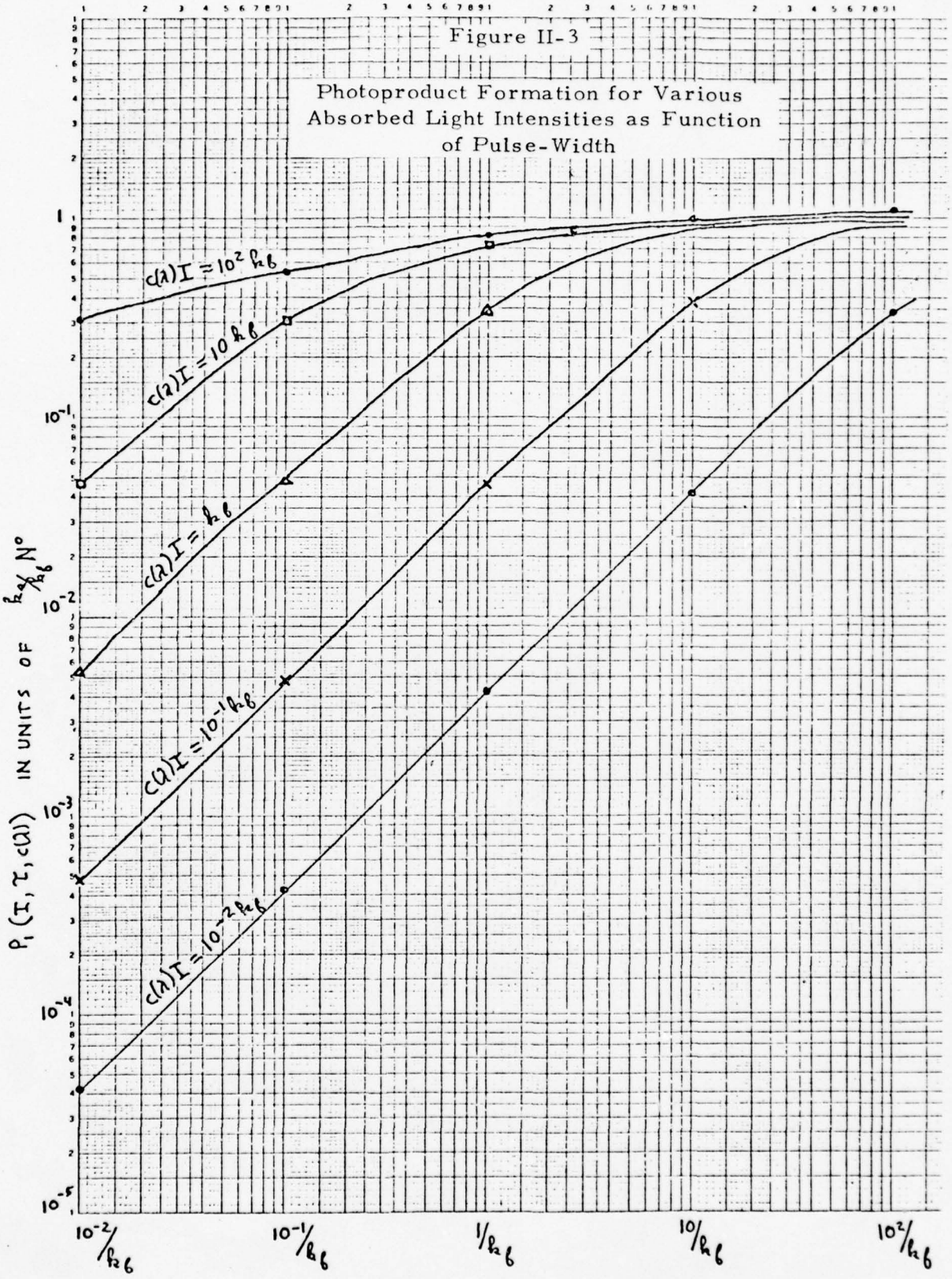
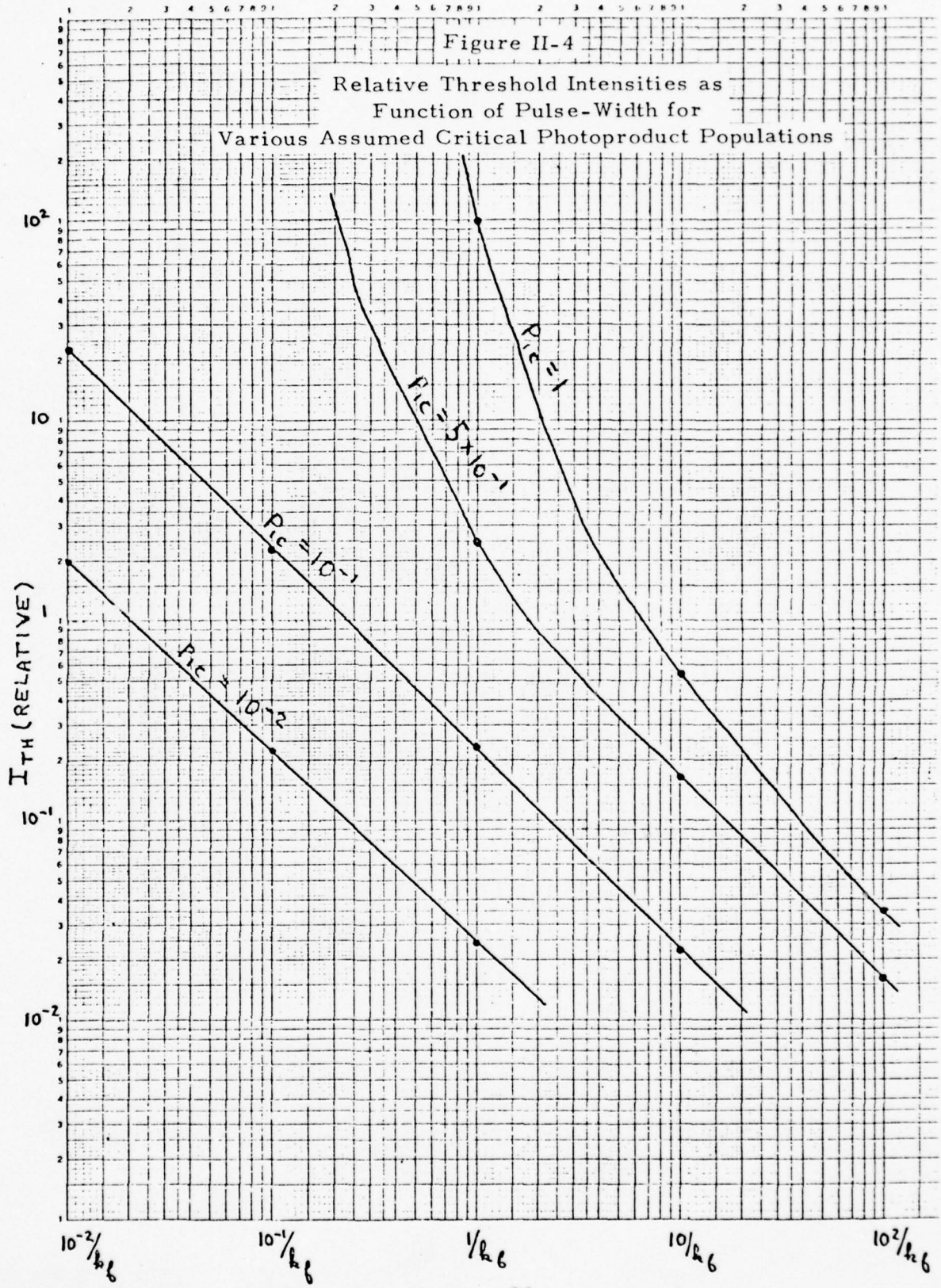


Figure II-4

Relative Threshold Intensities as Function of Pulse-Width for Various Assumed Critical Photoproduct Populations



number of photoproducts formed would not be proportional to the total energy dose for any photochemical mechanism which involved absorption of more than one photon.

With a pulse-width of approximately 5 nanoseconds, τ is approximately equal to $1/k_f$. Inspection of the curve for $\tau = 1/k_f$ on Figure II-2 shows that the deviation from linearity becomes significant only for intensities such that $C(\lambda)I > k_f$, i.e., when depletion of the ground state population is significant. If the conditions necessary to cause macroscopically visible damage in vivo were such that deviations from linearity were significant, this fact would be readily apparent in the experiments proposed to test the photochemical model. Thus, if a threshold intensity, I_{th}, were determined for a single pulse then the threshold for "n" consecutive identical pulses would be I_{th}/n^x where $x \geq 1$. Any value of x greater than one represents a deviation from linearity and indicates that ground state depletion in the absorbing medium is significant. It is fortuitous that a value of $x > 1$ would also serve to differentiate more clearly the photochemical mechanism from any non-cumulative mechanism which would be represented by $x = 0$.

The analysis presented above assumes certain relationships among the rate constants for transitions between the electronic energy levels. However, the analysis may be repeated for any other ratios of rate constants which may be appropriate for the molecules involved in the photochemical reactions. The analysis is readily extended to cover photochemistry involving the T_1 rather than the S_1 state and to cover biphotonic mechanisms involving either state. There are no explicit restrictions on the laser beam parameters and the analysis should be applicable to a wide variety of laser systems when-

ever photochemistry is the dominant mechanism for damage.

(3) Three Level Scheme with Long-Lived Intermediate Species

The three level scheme as discussed above predicts that for long pulses the damage threshold will be directly proportional to the product of the intensity, I, and the pulse-width, τ, of the exposure. This reciprocity between intensity and pulse-width should be valid provided the pulse-width is long compared to the lifetimes of the excited electronic states ($\sim 10^{-8}$ - 10^{-5} sec). Indeed, confidence in this initial version of the proposed photochemical mechanism was based in part on the observed reciprocal behavior for long continuous exposures. However, later experiments (described in the following Section) showed that the reciprocity relationship broke down for pulse-widths of 1 msec or less. Thus, it was necessary to re-evaluate the photochemical model with the realization that if the mechanism postulated in Figure II-1 were valid, the lifetime of at least one of the excited electronic states would have to be several orders of magnitude longer than the lifetimes observed for biological molecules known to be present in primate corneas[1,3]. Alternatively, a transient intermediate species with such a long lifetime ($\sim$1msec) could be integrated into the energy level scheme. The most likely candidate for this long-lived intermediate species is a free-radical, a postulate which is consistent with established photobiological processes.[3] Accordingly, we have modified the theoretical model to account for such a long-lived intermediate, and this more sophisticated and realistic scheme is outlined in Figure II-5.

In the modified scheme, the transient species, R, may be formed

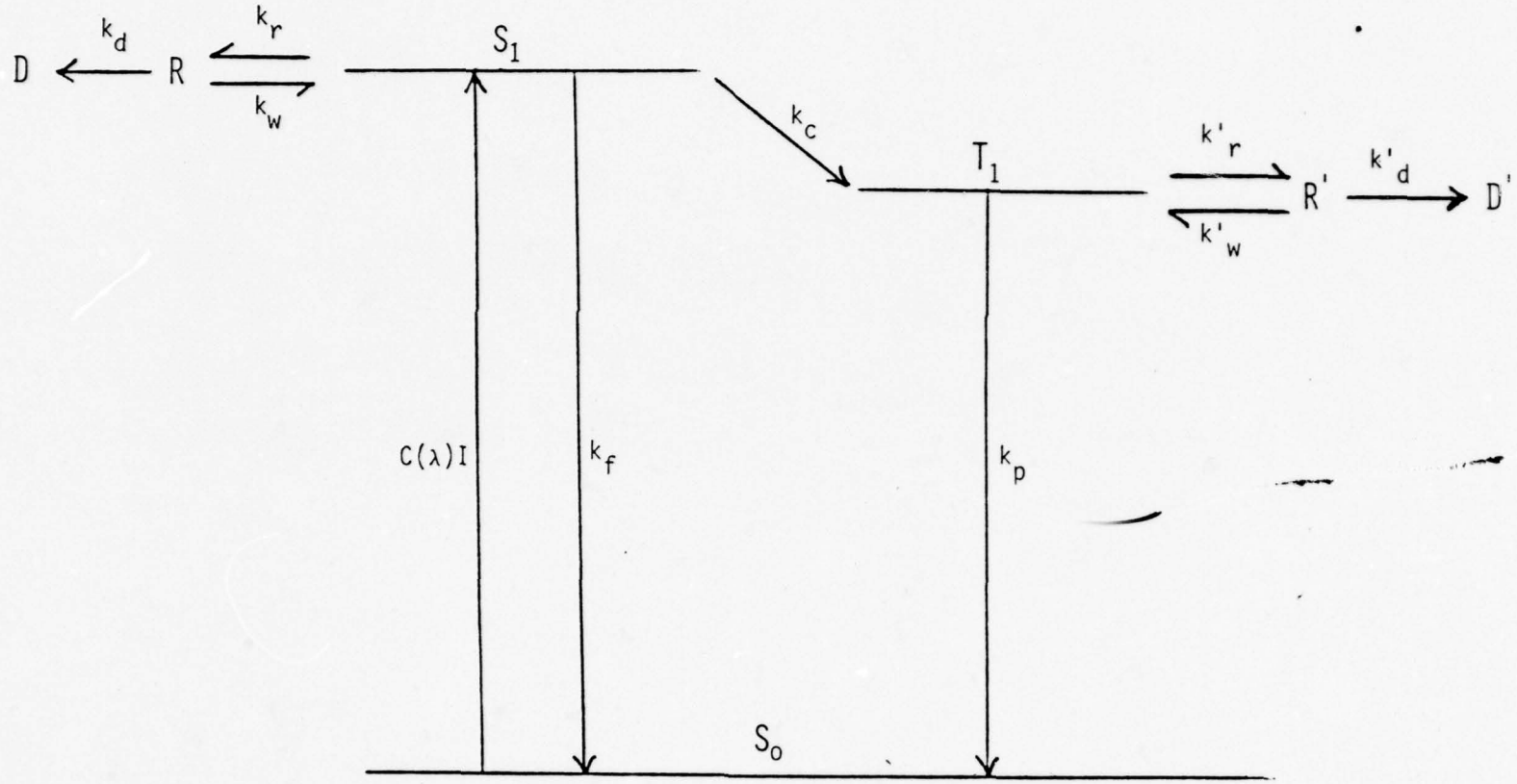


Figure II-5. Three-Level Scheme with Transient Intermediates

reversibly from the excited singlet state, S_1. R may then revert to the S_1 state or proceed to yield a photoproduct by an irreversible step. Similarly, a transient species R' may be formed from the excited triplet state, T_1, also leading to an irreversible photoproduct. The rate equations describing the scheme illustrated in Figure II-5 are as follows:

$$\frac{dS_0(t)}{dt} = -C(\lambda)I\ S_0(t) + k_f S_1(t) + k_p T_1(t) \tag{15a}$$

$$\frac{dS_1(t)}{dt} = C(\lambda)I\ S_0(t) + k_w R(t) - (k_r + k_f + k_c)\ S_1(t) \tag{15b}$$

$$\frac{dT_1(t)}{dt} = k_c S_1(t) - (k_p + k'_r)\ T_1(t) + k'_w R'(t) \tag{15c}$$

$$\frac{dR(t)}{dt} = k_r S_1(t) - (k_w + k_d)\ R(t) \tag{15d}$$

$$\frac{dR'(t)}{dt} = k'_r T_1(t) - (k'_w + k'_d)\ R'(t) \tag{15e}$$

This set of coupled differential equations cannot be solved in closed form as was done for the simple three level scheme. However, the rate of photoproduct formation is linearly proportional to the population of R or R' and these populations will approach steady-state values for long exposures. Thus, this scheme still predicts reciprocity between intensity and pulse-widths but only for pulse-widths which are long relative to the lifetimes of the transient species R and R' as well as to the lifetimes of the excited singlet and triplet states (the requirement for the simple three level scheme). For shorter pulse-widths (i.e., pulse-widths on the order of the lifetimes of the transient species) the populations of the transient intermediate

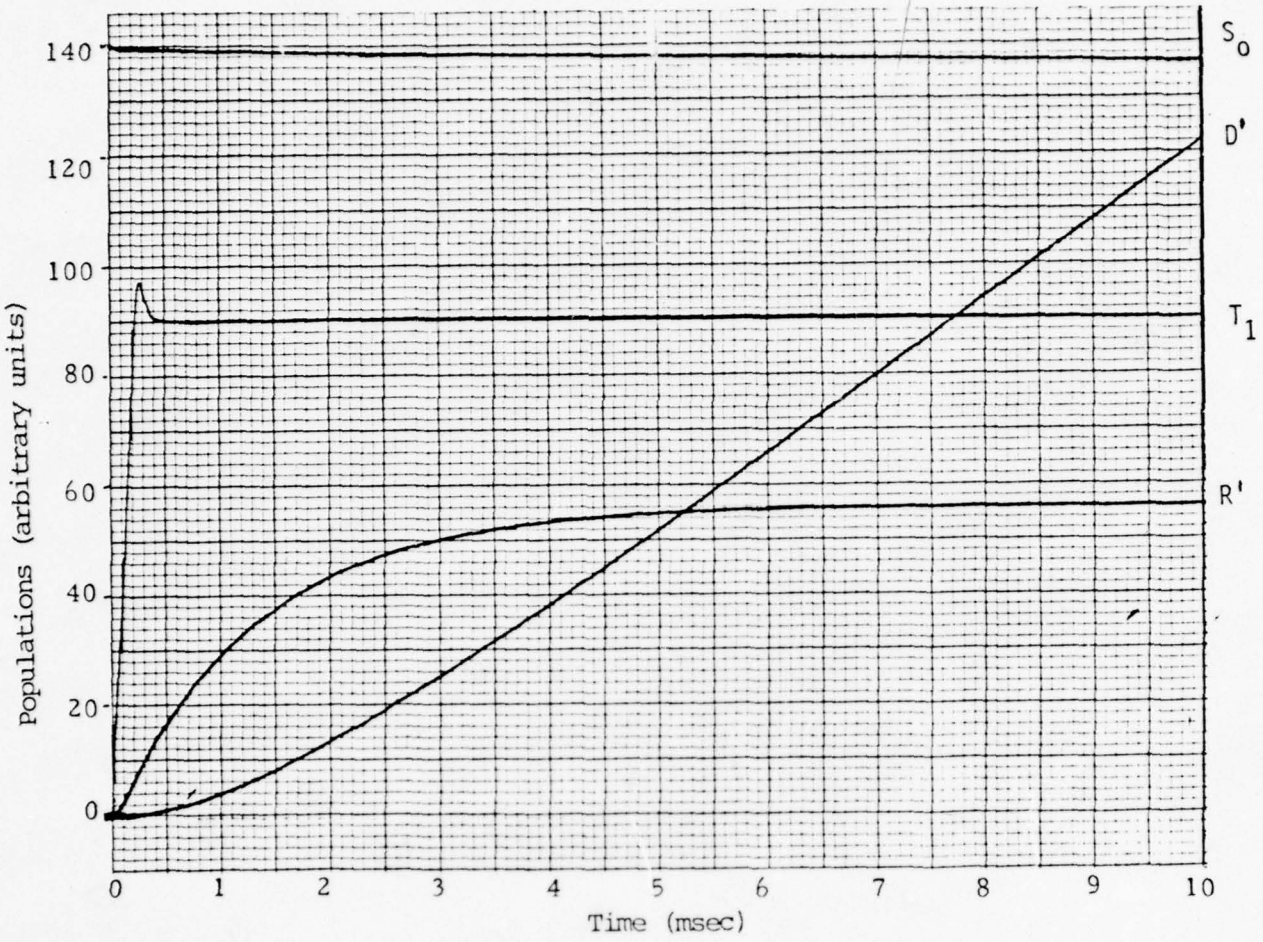
species will not reach their maximum (steady-state) values and, hence, the rate of photoproduct formation will be less than that obtained after the steady state is achieved. Thus, for such pulse-widths an increase in the threshold energy dose is predicted. This, in fact, is what is observed experimentally as the pulse-width is decreased from 20 msec or longer to 1 msec or less (see Section II-D(1)). This significant observation indicates that the lifetime of the transient intermediate is between 1 msec and 20 msec.

In order to achieve some insight as to the quantitative dependence of damage formation on laser beam parameters, the rate equations (15) were solved for specific cases by analog computation. The rate constants involved were given nominal values as follows: $k_f = k_c = 10^9 \text{ sec}^{-1}$, $k_p = 10^6 \text{sec}^{-1}$, $C(\lambda) I = k_r = k_w = k_d = k'_r = k'_w = k'_d = 10^3 \text{ sec}^{-1}$.

Each of these rate constants can be varied individually by a factor of ~100 from the nominal value. The exact solution for each set of rate constants, that is, the time-dependent population of each of the molecular states can be displayed on an oscilloscope and, if desired, plotted out on an X-Y recorder.

A typical result of an analog solution to Equation (15) is shown in Figure II-6. The populations of the S_0, T_1 and R' states as well as the number of photoproducts, D', formed via the R' state are shown for the case of continuous irradiation. The population of the ground state, S_0, remains virtually unchanged, being only slightly depleted by the accumulation of photoproducts and of molecules in the excited electronic states. The population of R' approaches a steady state with a time constant of ~1.7 msec (which is determined by the assigned values of k'_r, k'_w and k'_d). Similarly,

Figure II-6. Populations of Ground State (S_o), Triplet State (T_1), Transient Intermediate (R') and Photoproduct (D') formed by Continuous Irradiation.



the T_1 population reaches its steady state in a time comparable with its assumed lifetime of 10^{-6} sec. (The rise-time shown on Figure II-6 is determined by the response time of the recorder; the overshoot shown in this curve is a recorder artifact.) After an initial induction period, the rate of photoproduct formation becomes linear with time once R' has reached its steady state.

If, instead of CW irradiation, we consider trains of pulses, the dependence of the rate of formation of photoproducts on the pulse-width (at constant duty cycle) can be determined. Figure II-7 shows how the population R'(t) varies with time for trains of 1 msec and 20 msec pulses (50% duty cycle). Since 20 msec is long compared with the lifetime of R', the population of this transient species reaches steady state during each "on" period and decays back to zero during each "off" period. Thus, the average population of R' is just half of that which would be obtained with CW irradiation.

In contrast, with a train of 1 msec pulses, the population of R' does not reach a steady state during the "on" period and does not decay to zero during the "off" periods. It can be seen that the average population of R' is slightly less than half that which would be obtained with CW irradiation. If the pulse-width were made even shorter the average population which could be achieved would be still less. Thus, the rate of formation of photoproducts, which in turn is directly proportional to the population of R', will fall off as the pulse-width becomes shorter than the lifetime of R'.

This is illustrated in Figure II-8 which shows the populations of

Figure II-7. Populations of Transient Intermediate Species (R') Formed by Irradiation Trains of 1-msec and 20-msec Pulses (50% Duty Cycle)

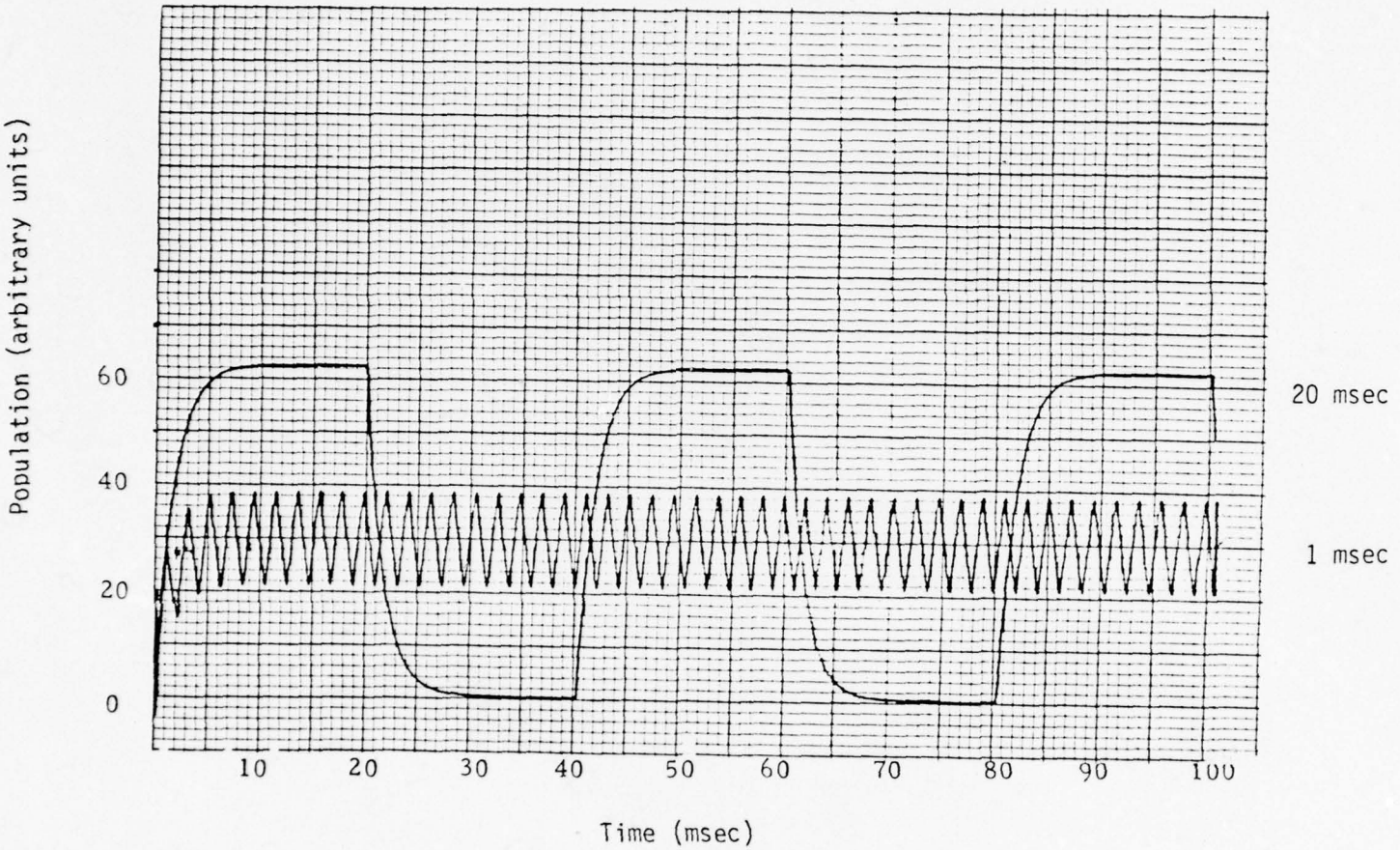
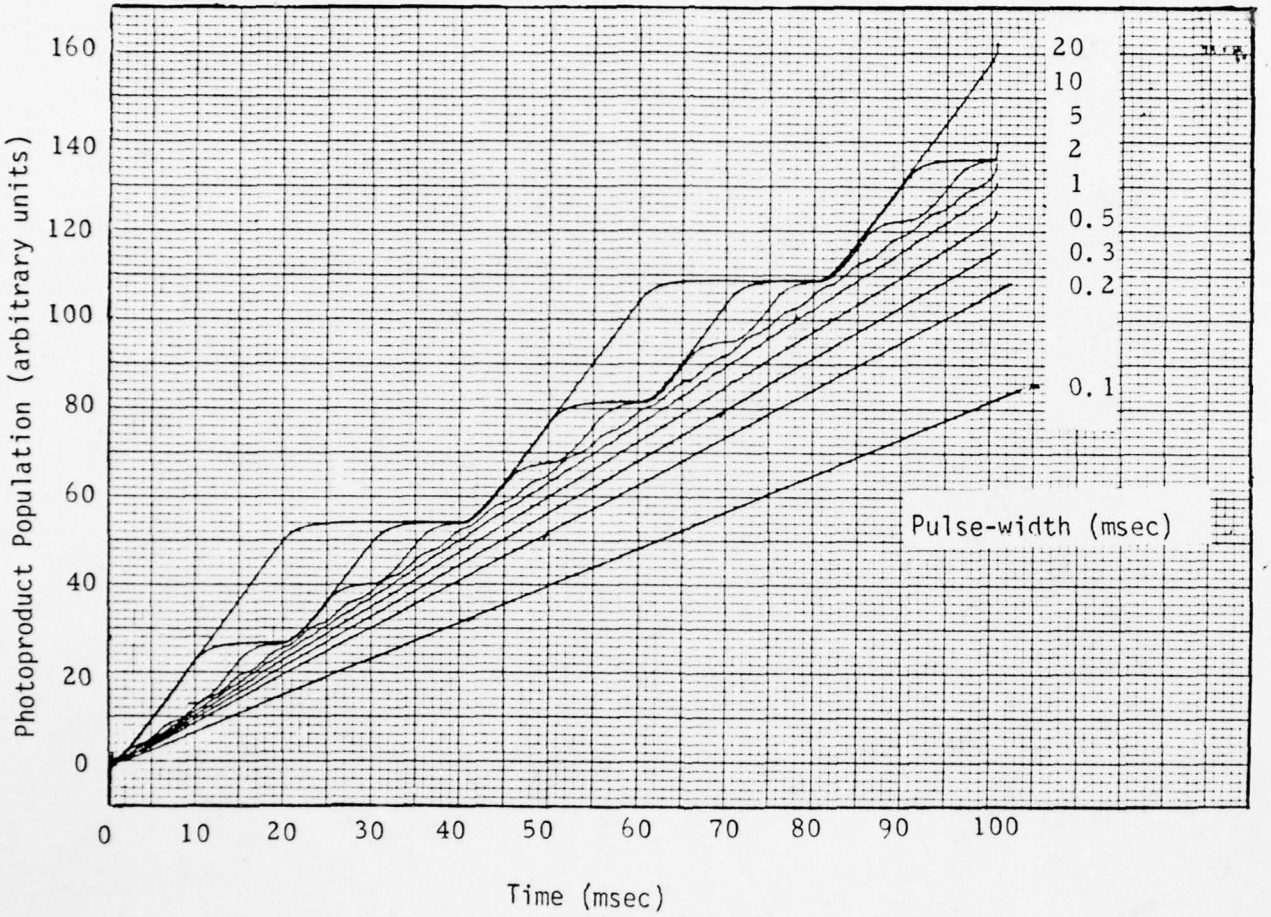


Figure II-8. Relative Populations of Photoproducts (D') Formed by Irradiation Trains of Various Pulse-widths (50% Duty Cycle)



photoproducts resulting from trains of pulses with pulse-widths ranging from 20 msec to 0.1 msec (50% duty cycle in each case). Note that as the pulse-width becomes smaller the fluctuations in the curves for each on-off period become minor and further cannot be resolved within the time response of the recorder. As a result, for assumed pulse-widths shorter than about 1 msec, the curves appear to be linear. Note also that as the pulse-width is decreased to less than two to three times the lifetime of R' (1.7 msec) the slopes of the lines begin to decrease. Thus, this model predicts an increasing threshold energy dose with decreasing pulse-widths.

The theoretical analysis presented here describes in a semi-quantitative manner the dependence of photoproduct formation on molecular rate constants and irradiation parameters. The experimental data obtained to date and described in the next Section are consistent with this analysis, being in accord with both the predicted reciprocity relationship for long pulse-widths and the predicted increasing threshold with short pulse-widths

As this theoretical analysis indicates, the pulse-width at which the reciprocity relationship begins to break down is characteristic of the lifetime of the transient species involved in the photochemistry. Thus, the experiments that are currently being conducted to verify the theoretical model will also yield a value for the approximate lifetime of the transient species. This will be a significant step both in aiding in the identification of the molecular species involved in the photochemistry and in developing the theoretical model into a working quantitative model.

C. EXPERIMENTAL

(1) Subject Preparation and Handling

The subjects used in these experiments are rhesus monkeys ranging in age from two to three years and in weight from two to four kilograms. No distinction is made between male and female subjects. The animals are maintained and the experiments conducted in accordance with procedures outlined in the "Guide for Laboratory Animal Facilities and Care". National Academy of Sciences-National Research Council and USAF/SAM Regulation 169-2, 6 February 1972. The clinical preparation and handling of the subjects is as follows:

1. The pupil of each eye is dilated to a maximum (~7mm) by the application of 2-3 drops of 1% atropine sulfate to the cornea.
2. The animal is tranquilized with an intramuscular injection of 0.1 cc per kilogram weight of ketamine hydrochloride (100 mg/ml).
3. A retro-bulbar injection of 0.6 cc of lidocaine hydrochloride (2%) is given.
4. An injection of 0.5 - 1.0 cc/kg of sodium pentobarbital (50 mg/ml) is given.
5. The eyelids are held open by a wire speculum. Corneal drying is prevented by periodic application of normal saline to the corneal surface.

The clinical preparation and handling of the subjects for the slit lamp observations on days following the exposure are as above except that the anesthetic and retro-bulbar injections are omitted.

(2) Apparatus and Procedures

The ultraviolet source is a Spectra Physics Model 164-01 krypton-ion laser equipped with optics to yield UV output simultaneously at 350.7 nm and 356.4 nm. Using a diffraction grating to resolve these two wavelengths, it was found that at higher power levels the 350.7 nm line accounts for ~75% of the output. As the power is lowered, this fraction becomes greater until the 356.4 nm line ceases to lase (this happens when the laser power output is reduced to ≈10% of its maximum value).

The aperture control of the krypton-ion laser was adjusted until the TEM_{00} mode output was obtained and all experiments were carried out with this mode. The intensity profile (Figure II-9) of the laser beam was measured with a beam scan apparatus consisting of an EG&G-SGD100A photodiode mounted behind a plate with a 50 μm pinhole. The photodiode detector was connected to an X-Y recorder which traced the diode output as a micrometer drive-synchronous motor assembly moved the detector across the laser beam.

The corneal spot size as defined by the $1/e^2$ diameter was measured to be 1.3 mm at a distance of 50 cm from the output mirror of the laser. The subject eye was positioned at this point as shown in Figure II-10. A single exposure was delivered to the center of the cornea of each eye. The subject was first positioned with the aid of a Spectra Physics Model 155 He-Ne alignment laser arranged so that its beam was coaxial with the krypton laser after reflecting off a beamsplitter. The subject eye was briefly exposed to the reflected He-Ne beam as it was positioned to receive the UV laser exposure. The power output of the alignment laser (<0.5 mw) is negligible relative to that of the krypton laser and the cornea and lens are both transparent to

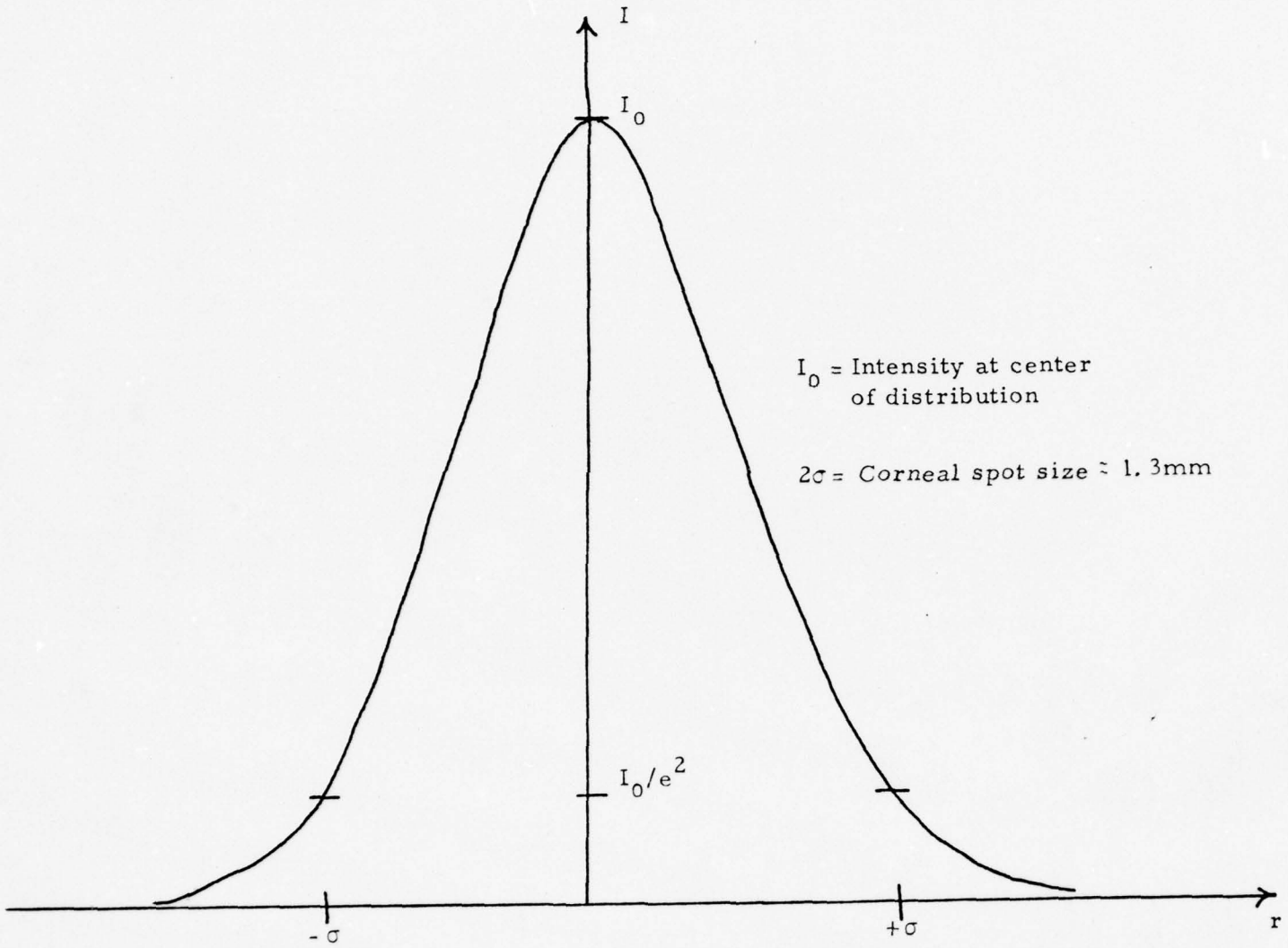


Figure II- 9 Typical Beam Scan of UV Laser Output

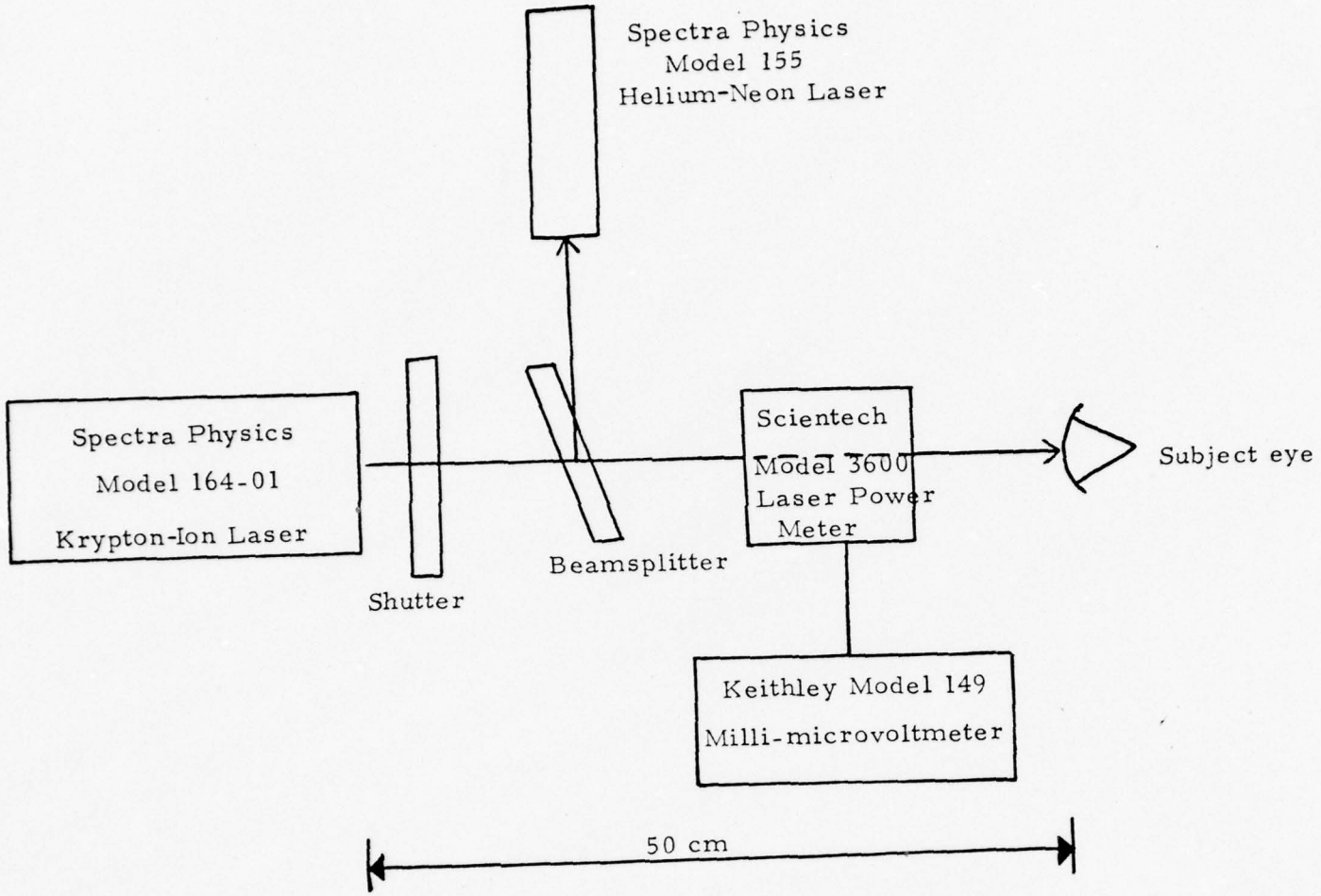


Figure II-10. Block Diagram of Laser Apparatus for Corneal Irradiations.

the output of the alignment laser so that there is no danger of spurious damage effects.

The laser power level (which is controlled by varying the current through the plasma tube) is measured before and after each exposure by monitoring the response from a Scientech Model 3600 Laser Power Meter with a Keithley Model 149 milli-microvoltmeter. The length of the UV exposure is controlled with an elecronically triggered mechanical shutter. In the cases where a train of UV pulses is desired, the beam is amplitude-modulated by triggering the shutter at the desired frequency with a pulse generator (for the case of one second pulse-widths) or by interposing a mechanical chopper between the laser and the test subject.(for shorter pulse-widths).

The chopping device consists of a symmetric slotted wheel driven by a small D.C. motor and regulated power supply. The slotted wheel can be driven at the desired frequency by varying the applied voltage. The pulse-width is monitored during the irradiation by intercepting a small (<10%) fraction of the chopped beam and directing it onto a photodiode, the output of which is fed into a Monsanto 101C counter-timer. The drift in the chopping frequency during the course of the 30-sec irradiations was generally small (±5%) except for the case of 20-msec pulse-widths where the drift approached ±20%. The power supply used to drive the slotted wheel apparently does not have sufficient current regulation to control the rate of revolution of the wheel at frequencies of $\leq$ 12 Hz. Since the slotted wheel is symmetric, all pulse trains are at 50% duty cycle.

Observations of the corneas and lenses of the exposed eyes were made

with a Nikon "Zoom-Photo" Slit Lamp Microscope. After considerable experimentation, an 18-hour criterion was chosen for lesion determination.

D. RESULTS AND DISCUSSION

(1) Corneal Epithelial Lesions

It was determined that long, continuous wave (CW) exposures of ~66 Joules/cm^2 could cause corneal epithelial lesions in rhesus monkeys. Slightly super-threshold lesions appear under slit lamp examination as well-defined spots on the surface of the cornea. The spots have a darker tint than the surrounding area and are more reflective to slit lamp light than the unexposed areas of the cornea. The spots have a fairly even texture if the exposure is ~5% or more above threshold but exposures closer to threshold doses often yield lesions with a more "patchy" appearance. There does not appear to be any significant depth associated with threshold lesions; however, exposures of 50% or more above threshold yield crater-like effects which may penetrate several cellular layers of the epithelium.

There are no visible signs of abnormality in the first 6-8 hours following a threshold exposure. Rather, the lesion appears and reaches maximum development in the period 12 to 24 hours following exposure. All indications of threshold corneal lesions disappear within 48 hours post exposure.

With higher exposures (two to three times threshold) the first signs of lesion formation appear in approximately one hour. Nevertheless, even the crater-like lesions which developed in these cases did not appear to penetrate below the epithelium and all had disappeared by 48 hours. To date, no permanent scarring of the corneal stroma and no permanent lenticular lesions

have been observed in any of the exposed eyes. Several of the exposed animals have been scheduled for future observations to monitor possible long term cataract formation.

Threshold determinations were carried out for continuous exposures (i.e., single pulses) of 45, 30 and 18 seconds. The sharply defined dose-response plots (Figures II-11 to II-13) show that the exposure energies required to induce corneal lesions are approximately 66, 66 and 72 Joules/cm^2 for 45-, 30- and 18-second exposures, respectively. Reciprocity, i.e., constancy of threshold energy dose, is predicted by the photochemical model as discussed in Section II-B.

This behavior, however, would not be expected for a purely thermal damage mechanism. Thermal model calculations (IITRI)[4] which have been carried out with the appropriate beam parameters predict that the irradiated corneal tissue reaches a virtual thermal steady state after several seconds of continuous irradiation. Within acceptable error limits, the predicted peak temperature is directly proportional to the intensity of the radiation source. Thus, the corneal temperature elevation induced by exposure to ~19 mWatt, 350 nm radiation for 45 seconds (~8 °C)* is calculated to be only one third that induced by an exposure to ~52 m Watt for 18 seconds (~24 °C). Yet, both of these exposures are observed threshold doses for their respective pulse-widths (see Figures II-11 and II-13).

---

* These approximate temperature increases represent upper limits and were calculated assuming that all corneal absorption at 350 nm occurs in the epithelial layer. The absorption of the whole cornea has been measured by Boettner,[5] but the absorptions of individual corneal layers are not known.

Figure II-11. Dose-Response Plot for 45-second Continuous Exposures. (Corneal spot size, 1.3 mm diameter ($1/e^2$); open circles indicate lesions observed only at the microscopic level - Section IV-B; 27 eyes).

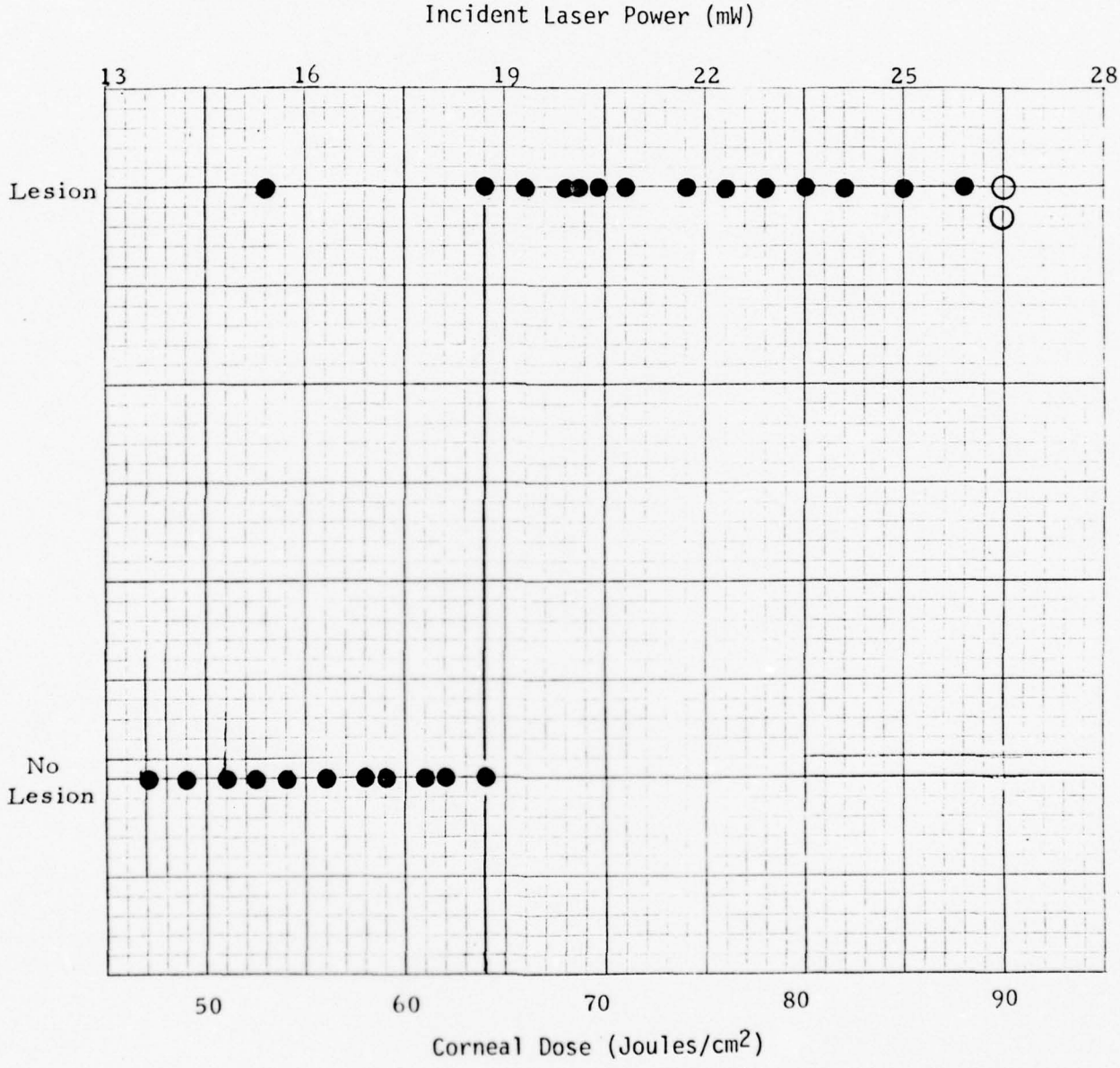


Figure II-12. Dose-Response Plot for 30-second Continuous Exposures. (Corneal spot size, 1.3 mm diameter; 30 eyes).

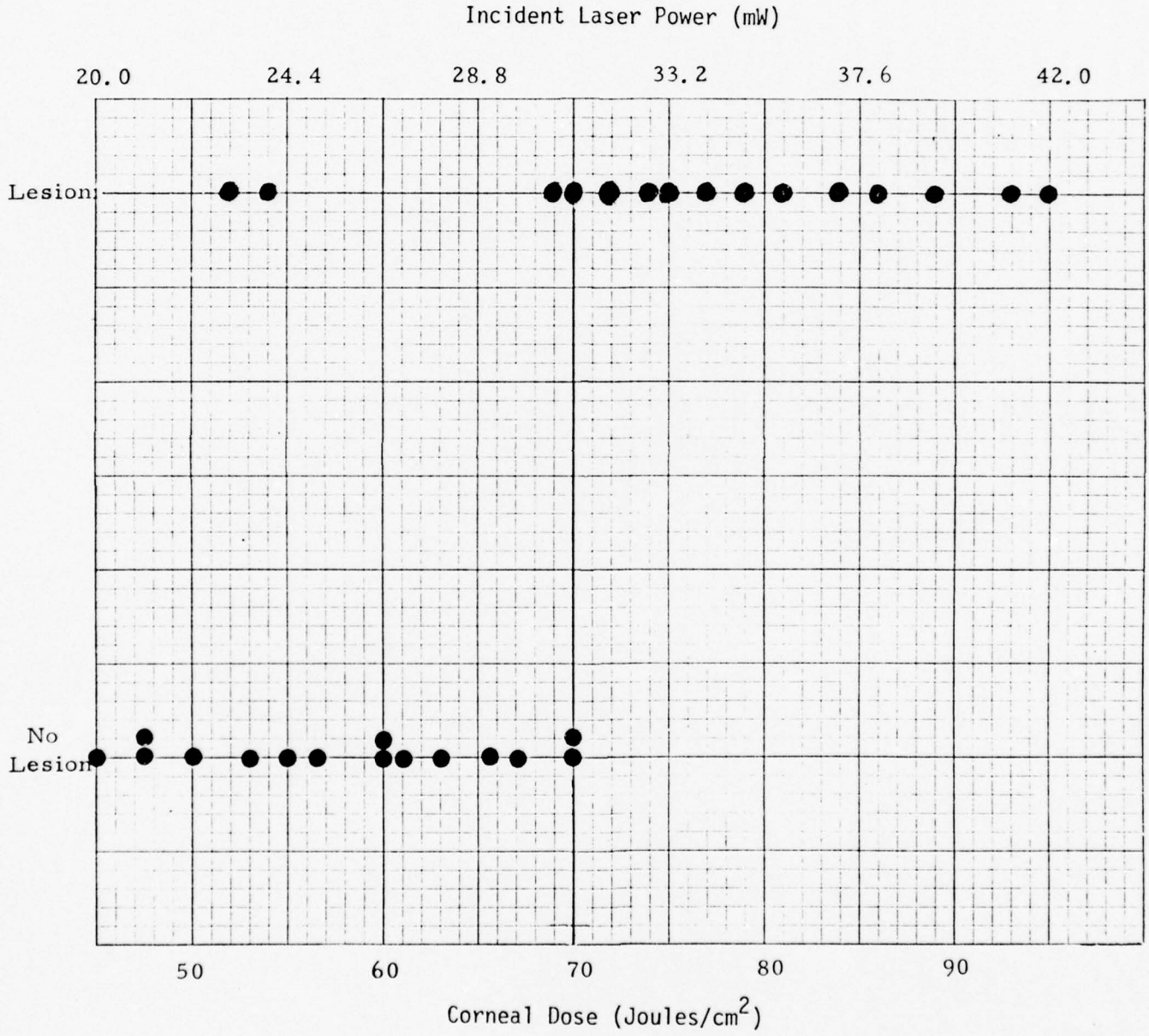
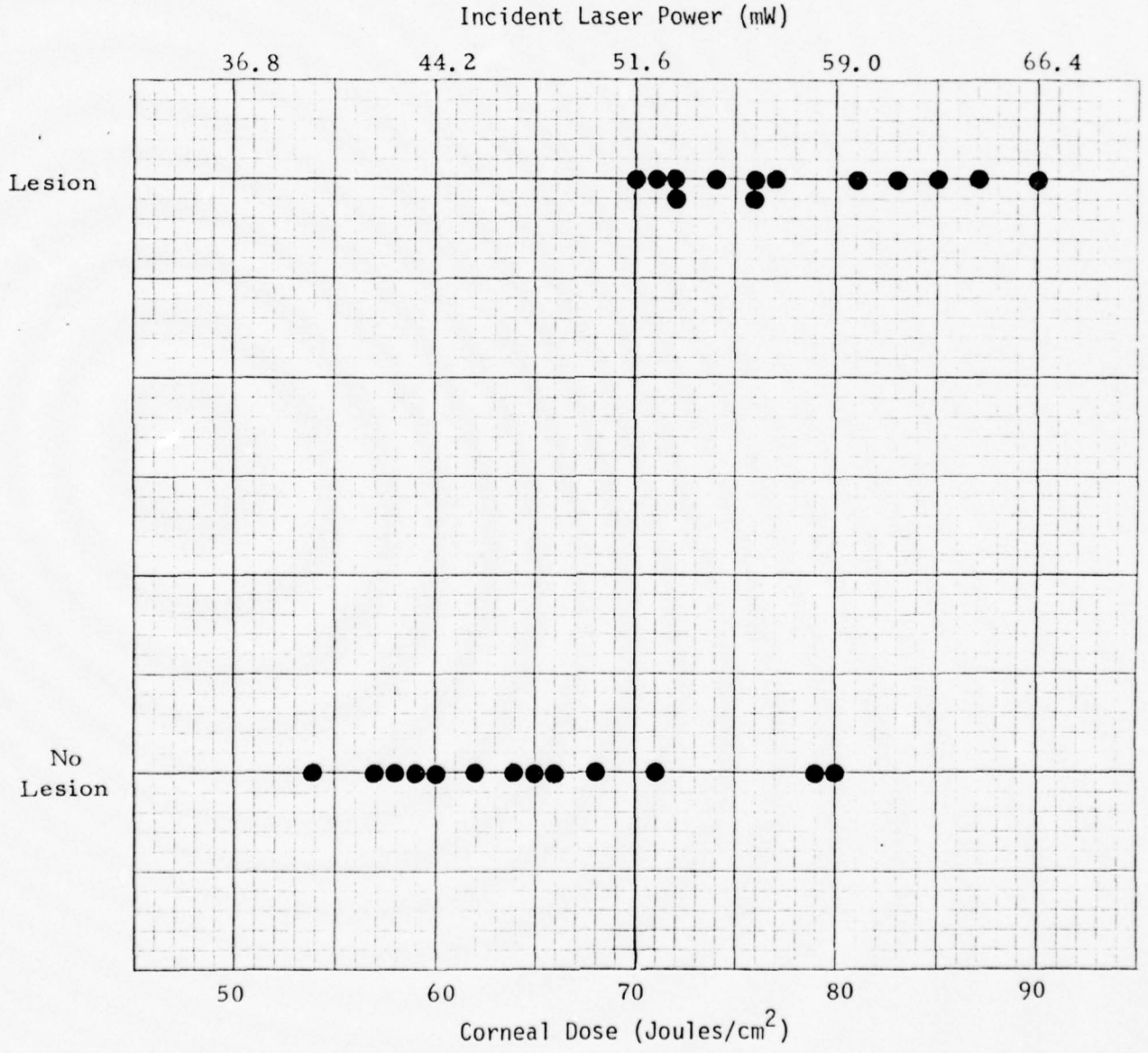


Figure II-13. Dose-Response Plot for 18-second Continuous Exposures. (Corneal spot size, 1.3 mm diameter; 26 eyes).



The maximum power output of the krypton-ion laser is not sufficient to induce epithelial lesions with single pulses of duration less than ~10 seconds. Thus, in order to determine corneal thresholds for shorter pulse-widths, the incident beam was amplitude-modulated with a mechanical shutter or a rotating sector. In this way, corneal threshold determinations have been carried out for 30-second pulse trains with pulse-widths ranging from 250μ sec to 1 sec with a 50% duty cycle in each case.

Figure II-14 illustrates the dose-response plot for a 30-sec train of 1-sec pulses (0.5 Hz repetition rate). The threshold for production of epithelial lesions is 66 Joules/cm^2 in agreement with the results obtained for long single pulses. Similarly, Figure II-15 shows that the threshold in the case of a 30-sec train of 20-msec pulses is 66.5 Joules/cm^2, also in essential agreement with the single pulse (i.e. continuous exposure) data. However, when 30-sec trains of 1-msec pulses (0.5 KHz rep rate) and 250-μsec pulses (2.0 KHz rep rate) were examined the threshold was found to be about 92 Joules/cm^2 as shown in Figures II-16 and II-17. This is an increase of about 37% over the values reported for each of the other cases discussed above. Although the statistical variance of the short pulse data is greater than for experiments employing longer pulses, preliminary probit analyses of all threshold determinations show that the marked increase in threshold values for short pulse exposures is real. The results of these probit analyses are summarized in Table II-2.

As discussed in Section II-B the increasing thresholds observed with decreasing pulse-widths in the millisecond regime imply the involvement of a transient species in the photochemical reaction scheme. When the results

Figure II-14. Dose-Response Plot for 30-second Trains of 1-second Pulses. (Corneal spot size, 1.3 mm diameter; pulse repetition rate, 0.5 Hz; 50% duty cycle; 33 eyes).

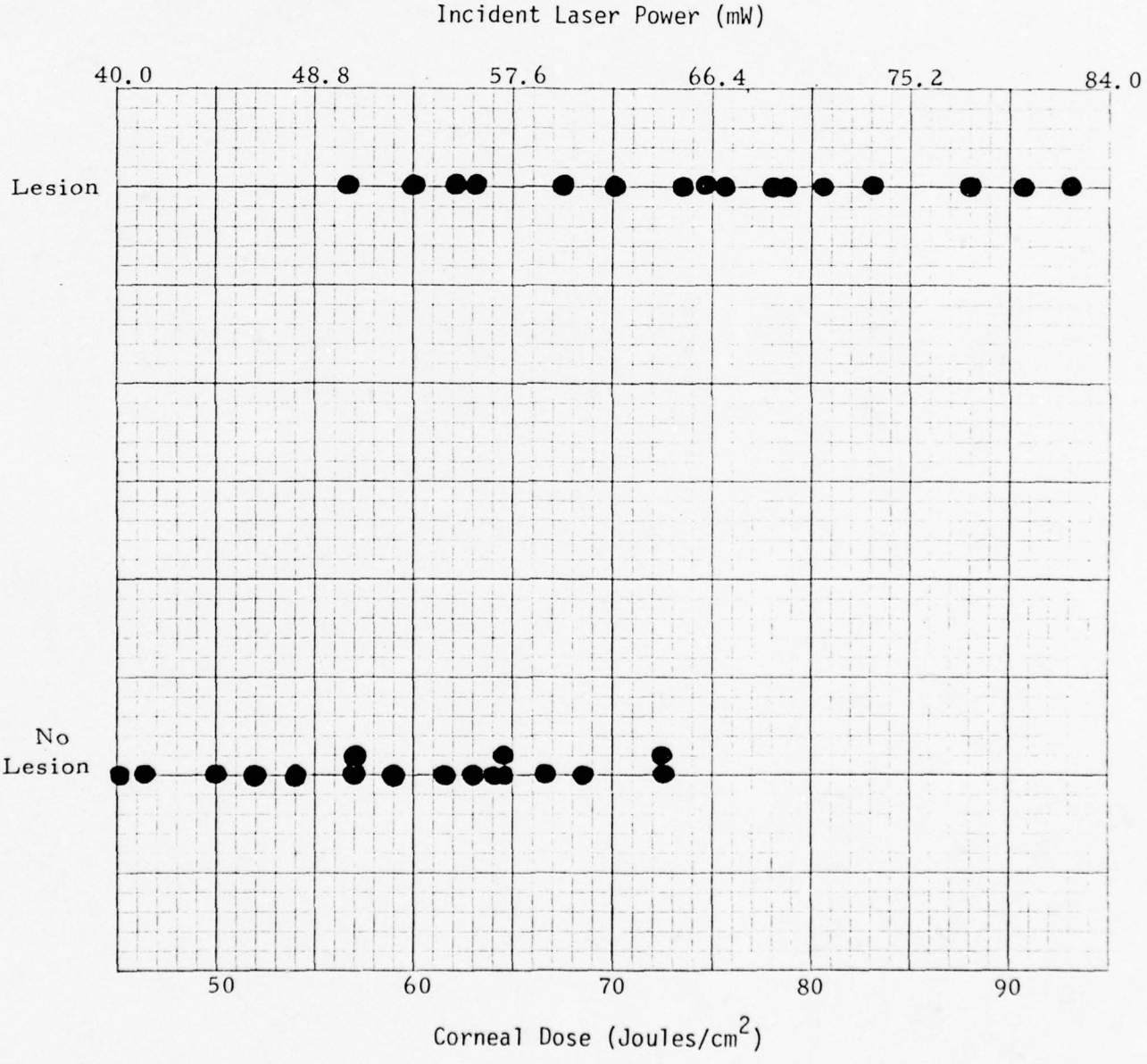


Figure II-15. Dose-Response Plot for 30-second Trains of 20- msec Pulses. (Corneal spot size, 1.3 mm diameter; pulse repetition rate, 25 Hz; 50% duty cycle; 25 eyes).

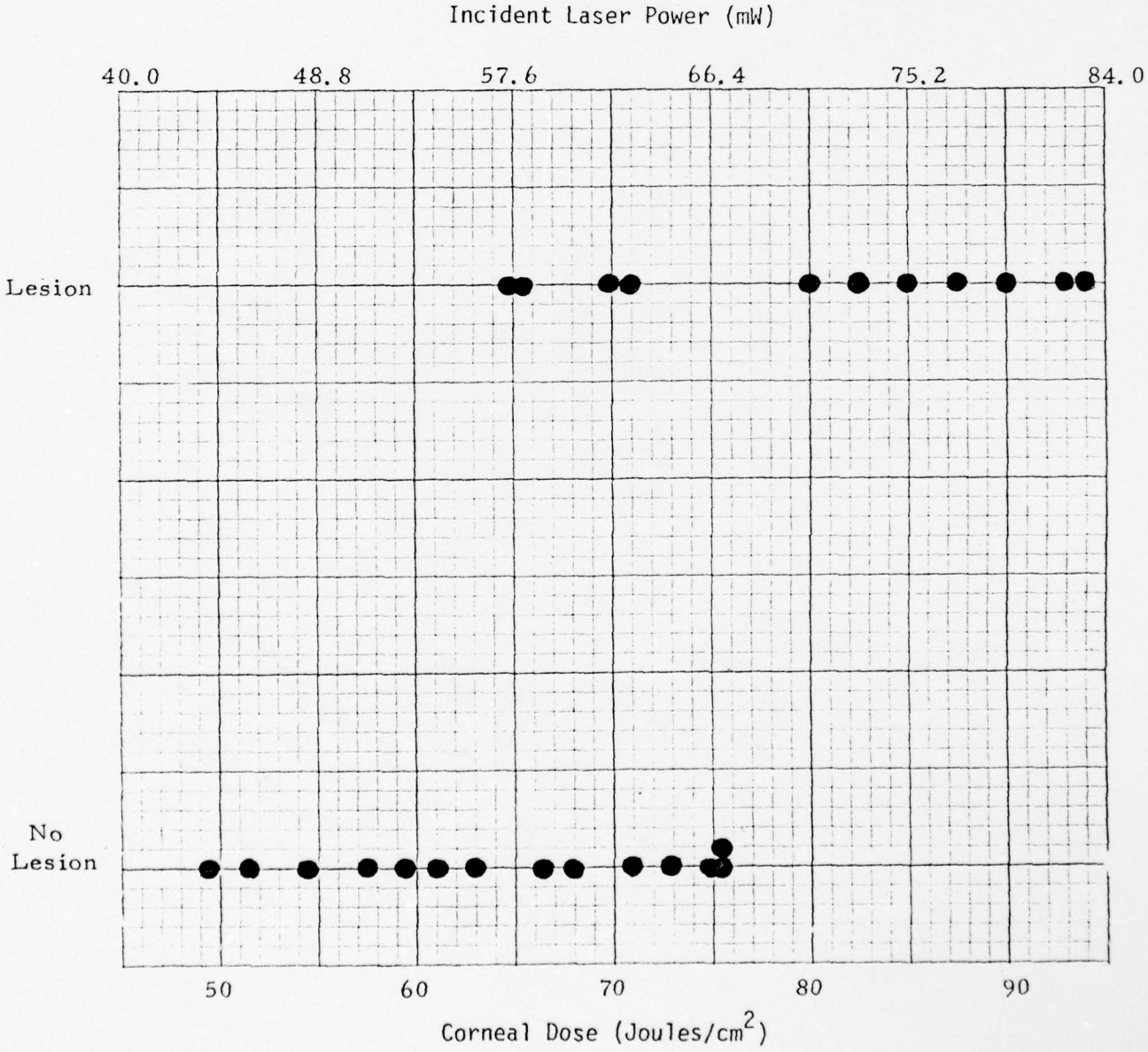


Figure II-16. Dose-Response Plot for 30-second Trains of 1-msec Pulses. (Corneal spot size, 1.3 mm diameter: pulse repetition rate, 0.5 KHz; 50% duty cycle; 29 eyes).

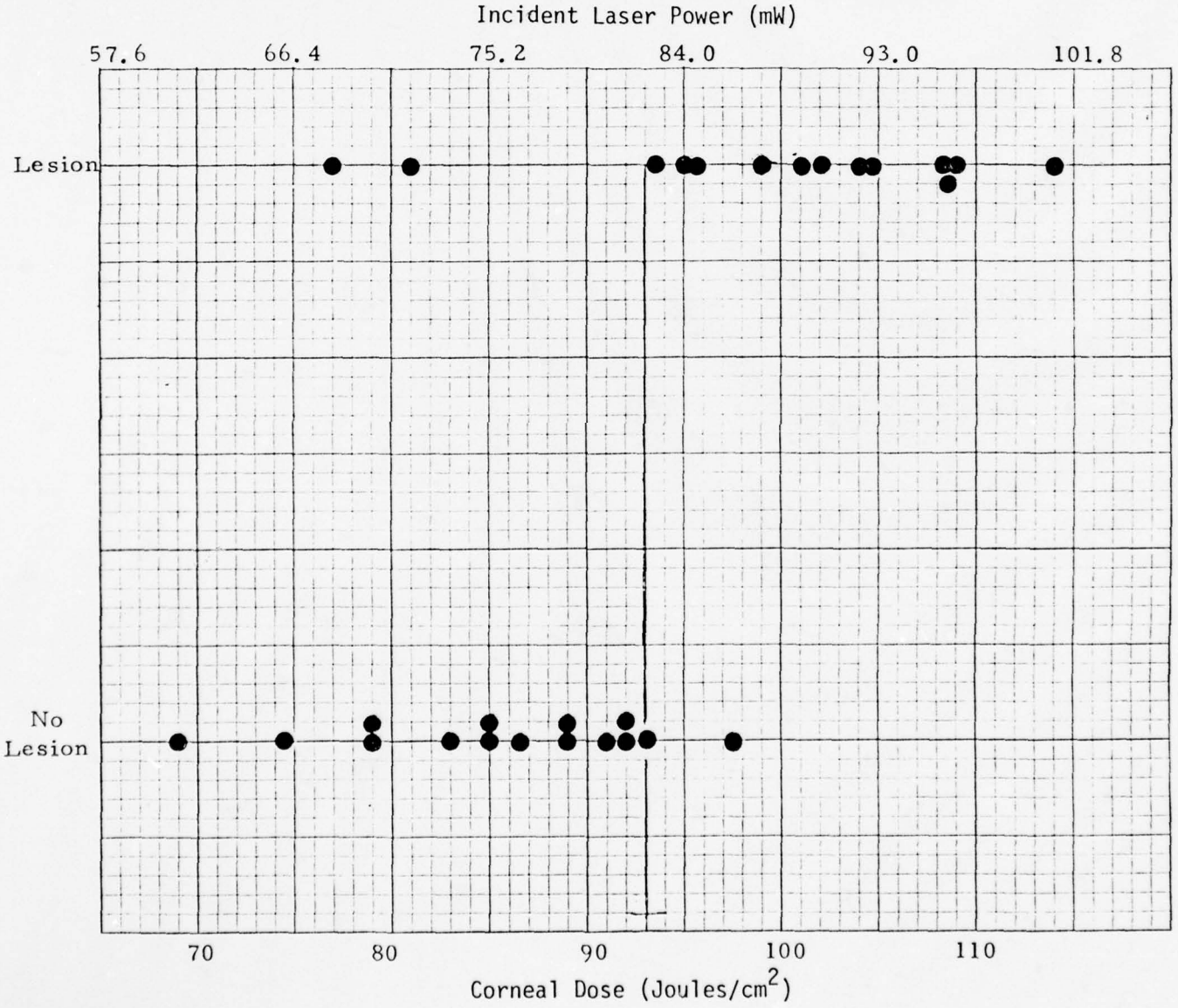


Figure II-17. Dose-Response Plot for 30-second Trains of 250-μsec Pulses. (Corneal spot size, 1.3 mm diameter; pulse repetition rate, 2.0 KHz; 50% duty cycle; 25 eyes).

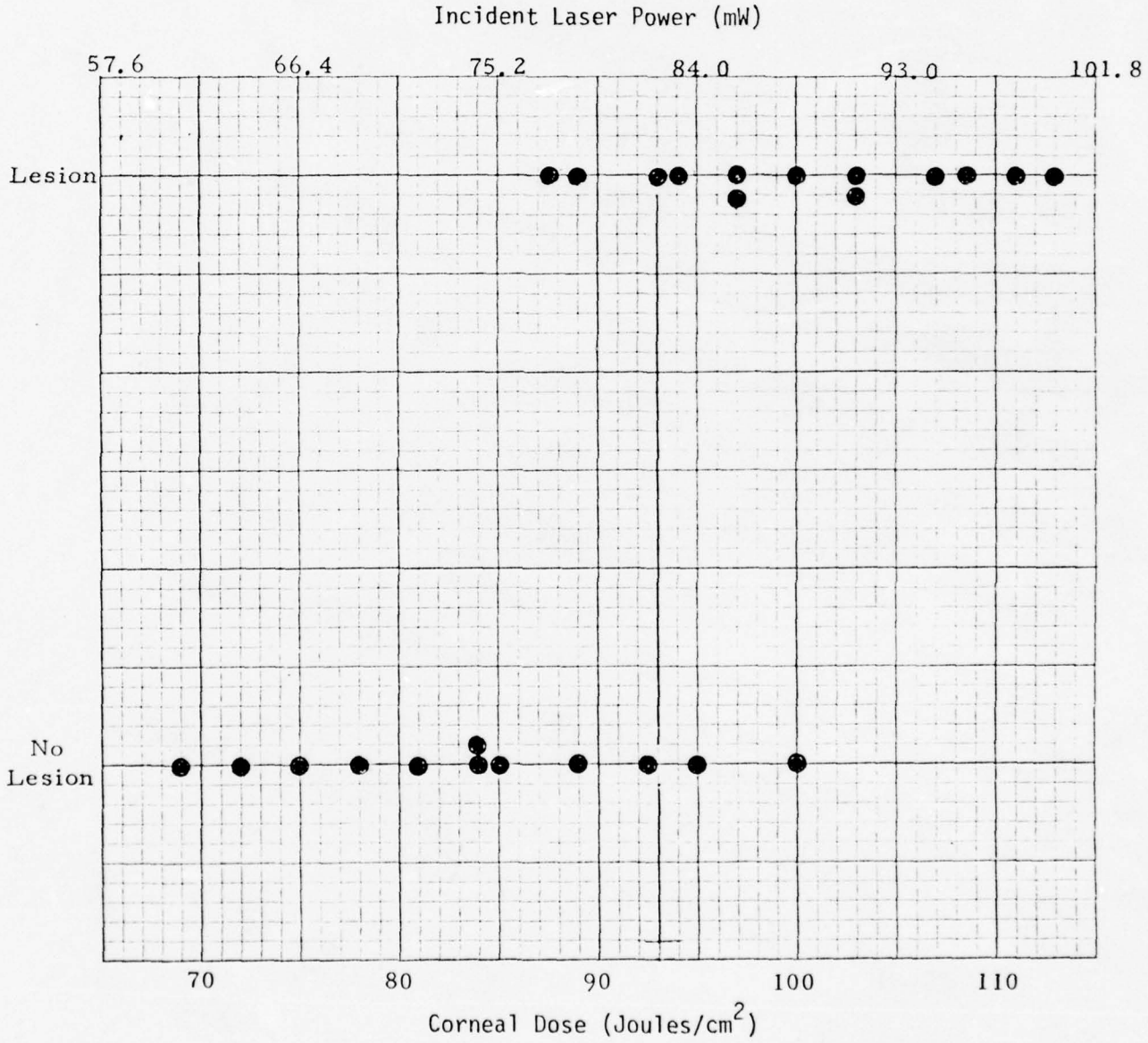


TABLE II-2

Thresholds (ED50) for Corneal Lesions Induced by Krypton-Ion Laser (350.7 and 356.4 nm). The error limits are the 95% confidence limits (two standard deviations) obtained from preliminary probit analyses.

Single Pulses

Pulsewidth (sec)	Threshold (J/cm^2)	No. of Eyes
45	65.6 ± 15.3*	27
30	65.6 ± 8.0	30
18	71.5 ± 5.8	26

30-Second Pulse Trains (50% Duty Cycle)

Pulsewidth (sec)	Threshold (J/cm^2)	No. of Eyes
1000	66.2 ± 8.6	33
20	66.5 ± 6.7	25
1.0	92.0 ± 8.0	29
0.25	91.8 ± 6.9	25

* Computed with lesions observable only by light microscopy counted as "no lesions". (See Figure II-11).

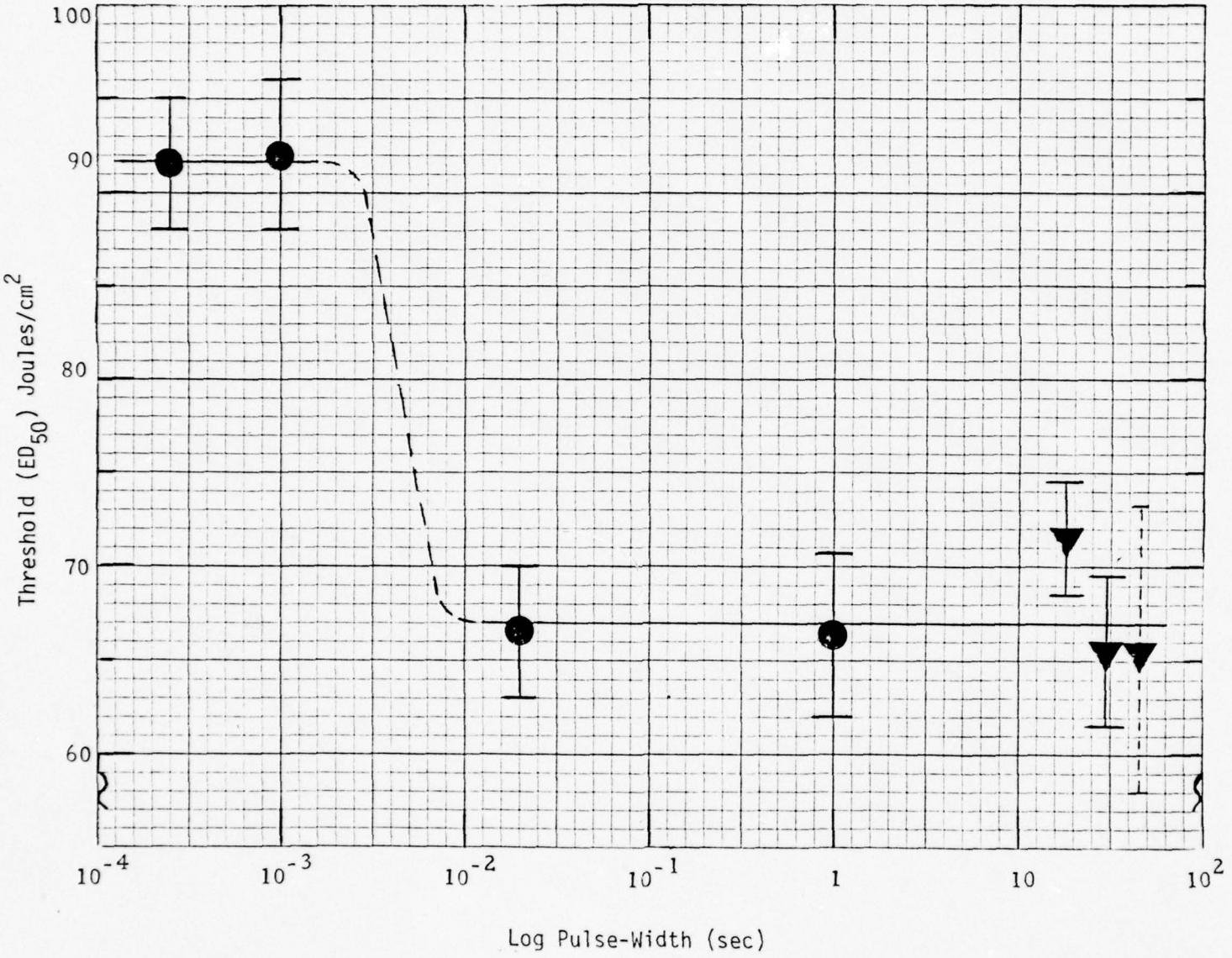
reported above are plotted as threshold vs. the log of the pulse-width (Figure II-18) it is clear that the lifetime of the postulated transient species lies between 1 msec and 20 msec. Additional experiments are in progress to obtain more data points in this interval so that the shape of the experimental curve can be compared with the results predicted by the analog computations. The lifetime of the transient species will be determined from the shape of the experimental curve and this number in turn will be fed back into the theoretical model. The transient species lifetime could prove to be important for the identification of the primary molecular species involved the photochemistry.

(2) Stromal and Lenticular Lesions

Several subjects have been exposed to doses of 350 nm CW laser radiation far in excess of the thresholds for corneal epithelial lesions. An exposure of 625 Joules/cm^2 (approximately 10 times the epithelial threshold) resulted in a lenticular clouding and a reflective spot either deep in the stroma or on the corneal endothelium. The lenticular lesion was readily apparent at 18 hours post-exposure but the deep corneal lesion was largely masked by an epithelial lesion until the latter had cleared (~48 hours).

At 66 hours post-exposure the lenticular clouding had become better defined and was readily observable with an indirect ophthalmoscope as well as with the slit lamp. Also at 66 hours, no stromal lesion could be identified but there was still a reflective spot on the corneal endothelium. By one week post-exposure both the endothelium and the lens had cleared and there was no observable disruption remaining in this eye (the retina was not examined).

Figure II-18. Corneal Epithelial Thresholds (ED_{50}) for Single Pulses (▼) and 30-second Pulse Trains (at 50% Duty Cycle, ●). Error limits are standard deviations.



An exposure of 950 Joules/cm^2 (approximately 15 times the epithelial threshold) yielded both stromal and lenticular lesions which were readily apparent after the epithelium had cleared. The stromal lesion was in the form of a cloudy circular spot. On close examination with the slit lamp it was noted that there were a large number of randomly oriented fibrous particles within the cloudy area. Although these particles were distinct, they were of sufficient density to give the impression of a hazy spot when viewing the cornea directly. The appearance of the stromal lesion was unchanged for more than a month but then began to clear and could no longer be oberved at two months post-exposure.

The lenticular lesion appeared to grow in size during the first week, stabilized in appearance during the next week or so and had cleared completely by one month post-exposure. The production of a reversible lenticular clouding following exposure to high doses of non-coherent UV radiation has been previously observed and noted to be a precursor of eventual cataract formation.[6] Accordingly the subject of this experiment has been monitored at monthly intervals but no cataract has been found to date (5 months post-exposure).

Although the thresholds for stromal and lenticular lesions appear to be far greater than those for corneal epithelial lesions, exposure of these deeper layers to UV radiation may ultimately prove to be of more concern because of long term, cumulative effects leading to irreversible damage.

(3) Retinal Lesions

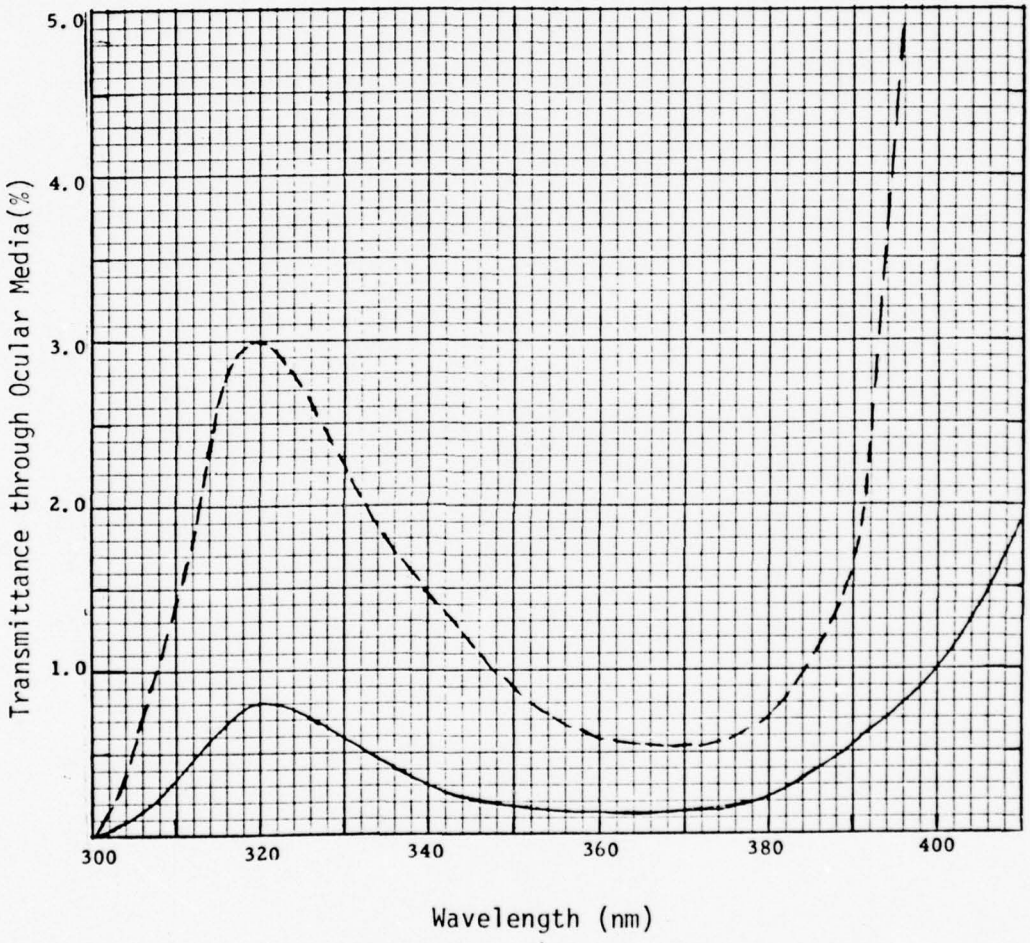
Little, if any, attention has been paid in the literature to the

possibilities of retinal hazards from ultraviolet laser radiation. Generally, the tacit assumption has been made that the cornea and lens are sufficiently strong absorbers of ultraviolet radiation to protect the retina from damaging UV rays. While this is undoubtedly true for wavelengths shorter than 300 nm, the assumption is questionable for the near UV wavelength range (300-400 nm). For wavelengths greater than ~320 nm, the corneal transmission is greater than 50% and the aqueous and vitreous media are even more transparent to near UV radiation. Only the lens is strongly absorbing at these wavelengths but, even so, lenticular transmission is on the order of 1% over much of the near UV. This is illustrated in Figure II-19 which is taken from data reported in Reference 5.

As evidence that the small amount of near UV radiation transmitted through the ocular media may present retinal hazards to personnel working with lasers in this wavelength range, we present here the first report of retinal lesions induced in primates by a UV laser. The laser is the same krypton-ion laser used for the corneal studies described earlier. The technique for aiming the laser beam onto a given spot on the fundus has been described in detail in an earlier report[1] and is illustrated in Figure II-20.

Figure II-21 shows a retinal lesion resulting from a 45-sec exposure to the 350 nm output from the krypton laser. The power incident at the cornea was 70.6 mWatt on a corneal spot size of 2.22 mm ($1/e^2$ diameter) resulting in an energy dose delivered to the cornea of 82 Joules/cm^2. The lesion was observed immediately after the exposure as a dark spot of 200-250 μm diameter. By 18 hours post-exposure the lesion had grown to >250 μm diameter surrounded

Figure II-19. Transmission Spectra of Rhesus Ocular Media. Ordinate is fraction (%) of corneal incident radiation transmitted to the retina; —direct radiation, --- total radiation. (After Boettner[5]).



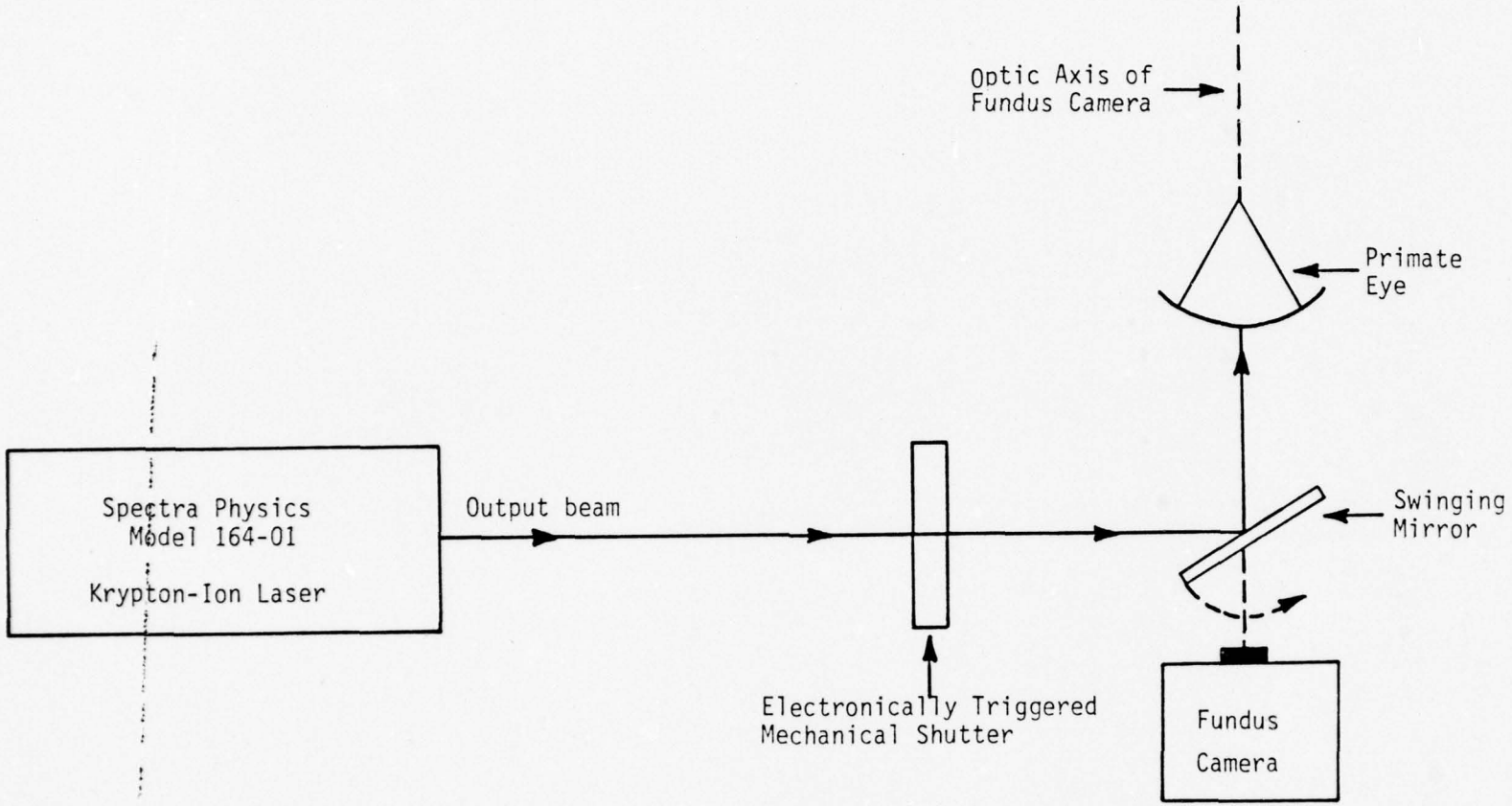


Figure II-20 Experimental Apparatus for Inducing UV Retinal Lesions



Figure II-21. Fundus Photograph of UV-induced retinal lesion; one hour post-exposure. The large circular area is the macula (~1500 μm diameter); the lesion (arrow) is a darker spot, ~250 μm diameter in the center of the macula.

by a dark annulus.

Figure II-22 shows a fundus with a total of seven lesions, five in the macular area and two paramacular (at 10 o'clock), caused by near UV laser radiation. For this series of shots the laser power was held constant at 105 mW and the pulse-widths were varied from 5 to 90 seconds. The seven exposures of 20 seconds and longer duration all resulted in lesions. However, some of these were not visible immediately or even one hour after exposure but were observed only at 18 hours post-exposure. The calculated energy dose for a 20-second exposure is 54 Joules/cm^2 incident on the cornea, which is below the corneal lesion threshold for these beam parameters.

At this time, little evidence has been accumulated as to the nature of the mechanism involved in the UV-induced retinal lesions or the variation in threshold as a function of beam parameters. Nevertheless, it is enlightening to compare the crude threshold estimate of 54 Joules/cm^2 with existing permissible exposure levels as set forth in the standard of the American National Standards Institute's Z-136 Committee On The Safe Use Of Lasers. The retinal permissible exposure level which is quoted for the wavelength range 0.4-1.4μm is ~500 μWatt for a 20-sec exposure. Over most of the visible region, a large fraction ($\lesssim$ 50%) of the incident radiation will be transmitted to the retina. At 350 nm, <0.25% of the incident radiation is transmitted directly to the retina[5]. Therefore, of the 105 m Watt incident upon the cornea in the above experiments, approximately 250 μ Watt is transmitted to the retina. ANSI permissible exposure levels are generally about 10 times lower than thresholds for retinal lesion formation ; thus, it appears that the 350 nm laser radiation is at least as hazardous in terms of inducing



Figure II-22. Fundus photograph of UV-induced retinal lesions; 18 hours post-exposure. The macula is the poorly-defined, large circular area in the center of the photograph. Lesions appear as light-colored spots (arrows).

retinal lesions as is visible laser radiation (for equal intensities incident on the retina).

Perhaps even more pertinent at this stage is an examination of the ANSI corneal permissible exposure level for 315-400 nm radiation. The value cited for a 20-sec exposure is 50 mW/cm^2. In contrast, the 20-sec exposure of 350 nm laser radiation which caused a retinal lesion was equal to 2.7 $Watt/cm^2$, for a 2.2 mm corneal spot size. For a larger spot size the energy density at the cornea would be lower, but essentially all of the non-divergent laser light which passes through the pupil will be focused onto the same retinal spot. Thus, if we consider a 7 mm corneal spot size (which is equivalent to the dimension of the dilated pupil of the rhesus monkey and is also a reasonable figure for the human pupil size in a dimly lit environment) a corneal exposure of 270 mW/cm^2 could very well result in a retinal lesion, other factors (such as lenticular absorption) remaining constant.

Inspection of the lenticular absorption spectrum (Figure II-19) shows that in the region near 320 nm or near the UV-visible border (~400nm), the transmittance of the ocular media to these wavelengths is at least three times greater than at 350 nm. Thus, even without further investigation, it is apparent that although the ANSI permissible exposure level for 315-400 nm radiation has an adequate margin of safety for corneal lesion formation, under certain conditions there is little safety margin for retinal lesion formation which may result from the same exposures. Whether there is any safety margin at all becomes rather doubtful when several other factors are considered.

(1) The UV-induced retinal lesions produced in the preliminary experiments to date have been 150-200 μm or larger. We have not yet had an

opportunity to vary the beam parameters and investigate a threshold for a "minimal visible lesion". Obviously such a threshold will be lower than the estimated threshold quoted in this report.

(2) The dependence of retinal lesion formation upon the laser beam parameters is unknown at this time. If the mechanism for damage is photochemical in nature, the efficiency of the mechanism may vary significantly with wavelength; thus, there is no reason to assume that 350 nm is the wavelength of maximum efficiency.

(3) Small variations in the lenticular absorbance from one subject to another will cause major fluctuations in the relative amount of radiation reaching the retina in each case. Again, there is no reason to assume that the subject used in these preliminary studies had lenticular absorptions lower than the norm.

In conclusion, there appears to be some question regarding 1973 ANSI corneal permissible exposure level for near UV laser radiation. On the basis of the results to date it is reasonable to speculate that with certain beam parameters, retinal lesions might be induced at exposure levels which are comparable to or below the ANSI permissible exposure levels for the cornea.

REFERENCES

1. "Research on the Eye Effects of Laser Radiation," Technology Incorporated, Annual Report Number 1, Contract No. F41609-73-C-0017, USAF School of Aerospace Medicine, Brooks AFB, Texas, (March 1974).

2. "Introduction to Ordinary Differential Equations," S.L. Ross, Blaisdell Publishing Co., Waltham, Massachusetts (1966).

3. "Excited States of Proteins and Nucleic Acids," R.F. Steiner and I. Weinryb, Eds., Plenum Press, New York (1971).

4. Takata, A.N., et al., "Thermal Model of Laser-Induced Eye Damage," Illinois Institute of Technology Research Institute, Final Report, Contract F41609-74-C-0005, USAF School of Aerospace Medicine, Brooks AFB, Texas, (October 1974).

5. Boettner, E.A., Final Report, Contract AF 41(609)-2966, Project No. 6301, University of Michigan (July 1967).

6. Bachem, A., Amer. J. Ophthal. 41, 969 (1956).

7. Federal Register, Vol. 8, No. 236, Part III (10 December 1973).

PART III

RETINAL TEMPERATURE MEASUREMENTS

A.D. Nawrocki, W.H. Bowie and R.F. Lemberger

A. INTRODUCTION

The chief objective of this project is to measure spatial distributions and temporal histories of temperature changes induced by laser radiation in the posterior portions of the vertebrate eye. The approach involves visually guided, surgical insertion of microthermocouple probes through the sclera in the region of the posterior pole. Experiments will be conducted at subthreshold, threshold, and suprathreshold exposures, using the presence of ophthalmoscopically visible and/or histopathologically correlated lesions as criteria for injury. The experimental variables will include wavelength (visible through near IR), radiant intensity, pulsewidth and repetition rate. Results of retinal temperature measurements will be provided to USAF SAM/RAL for validation of a semi-empirical model for predicting temperature increases based upon heat diffusion equations.

B. BACKGROUND

Of the various sensory organs in man, the most susceptible to injury by laser irradiation is the eye. As Cain and Welch[1] have noted, the increasing use of lasers has necessitated the implementation of safety standards based upon experimental measurements and, where possible, clinical data. As our understanding of laser-induced injury and dysfunction has increased, these standards have been revised periodically.

At the present time, it appears that the complex chemistry which underlies

laser induced injury can be predicted reasonably well as classical (macroscopic) heat diffusion and first-order kinetics. However, recent results of Hemstreet, et al.,[2] indicate that the ocular effects of repetitive pulses at certain fast rates typical of field applications do not necessarily add linearly to produce equivalent injury as predicted by strictly thermal processes. In addition, all present thermal models ignore possible changes of state such as vaporization in which heat is absorbed incrementally without contributing to rising temperature. Thus, both from first principles and direct experiment, thermal modeling cannot be expected to predict effects of all possible laser parameters, in particular of certain fast, intense or repetitive pulses.

Clearly, experimental validation of thermal modeling in such applications is necessary to establish limits of its overall utility as well as to provide possible corroborating evidence as to the significance or predominance of other mechanisms. The advantage of such a model, once validated, is its ability to predict ophthalmoscopic damage -- and by extension with other physiological and psychophysical correlates, visual dysfunction -- without the expense and time of generating large masses of experimental data for each new set of exposure parameters.

Briefly, thermal effects of laser irradiation in the retina may be understood as follows: with the exception of the pigment epithelium (PE) and choroid, the retina and underlying tissue are essentially transparent, and the PE and choroid may be considered as a double-layered, spectrally dependent heat sink. When a highly collimated source or sufficiently bright, diffuse source impinges on the eye, the PE and choroid can rapidly absorb and conduct heat. For laser

pulse durations less than about 10 sec and greater than 100 μsec, the associated temperature increases apparently cause rate-dependent injury mechanisms such as deactivation of enzymes and protein denaturation[3] as well as pathological signs such as edema, lysis, and at suprathreshold exposures, massive disruption of cellular layers.

Experimental temperature measurements with probes whose tip diameters exceed 50μm have been suspected of recording artifacts[4]. Metal-vapor coated, quartz microthermocouples developed by Reed[5] and modified by Cain[6] are possibly more suitable; tip diameters of 10-30 μm and time constants of about 200 μsec have been reported[4]. Experimental measurements with this probe have been conducted by Welch, et al.[4,7] and have been compared with thermal models originally devised by White, et al.[8] and Henriques[9].

C. EXPERIMENTAL

Research efforts under this contract will utilize thermocouple probes developed by Reed and Cain (cited above) in conjunction with an advanced computational scheme for predicting chorioretinal spatio-temporal temperature profiles developed for USAF SAM/RAL[10]. The recording/control systems for performing these measurements will be based at least in part on equipment assembled by Crum[11].

A block diagram of this experimental system is shown in Figure III-1. The laser beam passes through converging optics to a pellicle driven by an incremental, hydraulically-driven beam deflector which deflects the beam through an arc whose center is near the pupil of the eye. The beam is gated and scanned across the retina by control logic and clock circuitry. An incandescent source illuminates the fundus of the eye with a Maxwellian view so

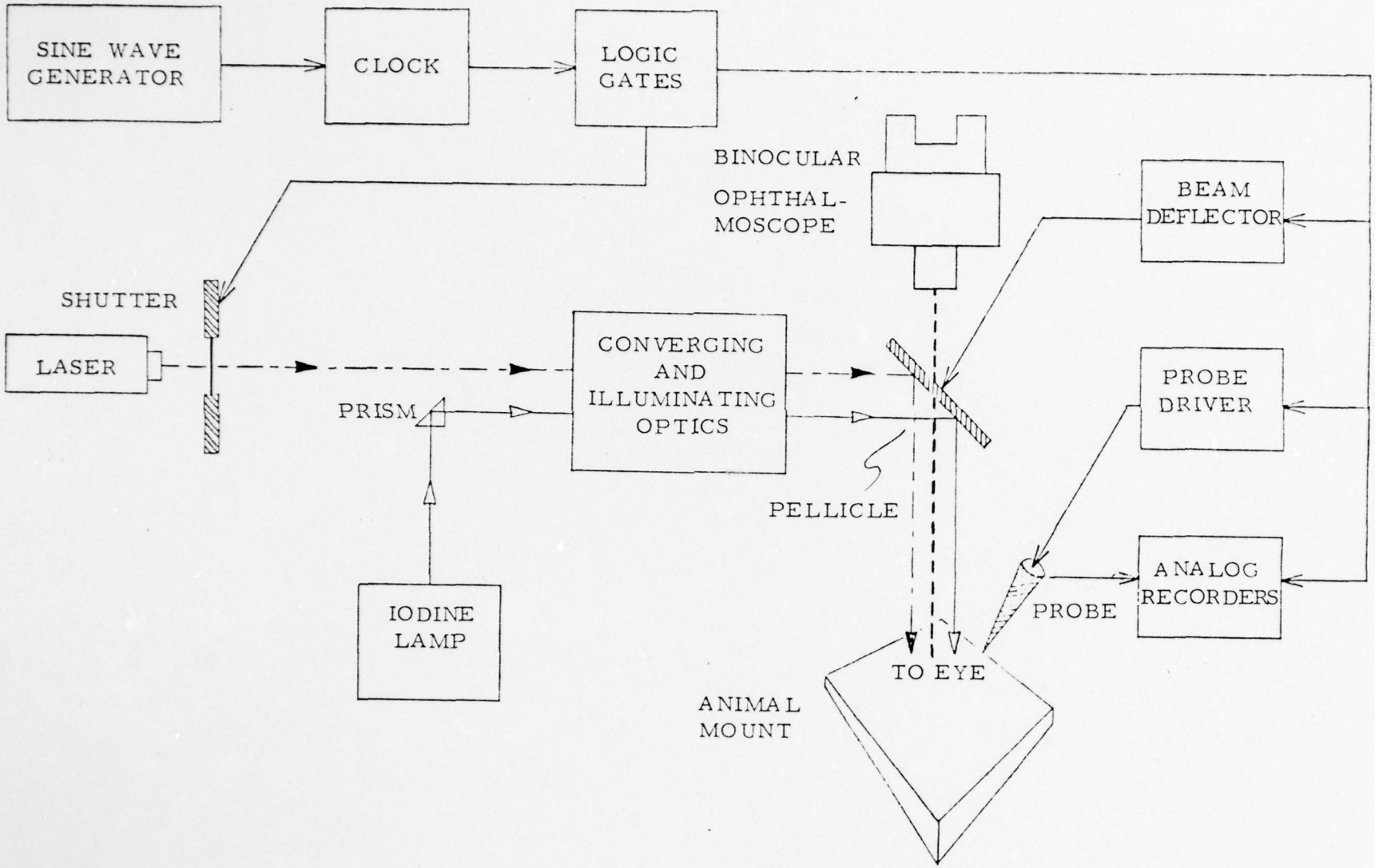


Figure III-1. Block Diagram of Experimental System for Retinal Thermal Probe Measurements.

that positioning of the probe can be observed with the binocular ophthalmoscope. Analog signals representing the temperature changes monitored by the microthermocouple probe are amplified and stored on magnetic tape for off-line computer processing.

Surgical procedures for implanting the microthermocouples into the eyes of rhesus monkeys have been developed in collaboration with USAF/SAM personnel based on a modification of the techniques employed by Dr. A. J. Welch's research group[4,7], University of Texas at Austin. With sufficient experience and additional tools and equipment, we plan to perform such surgery within the USAF SAM Laser Laboratory (RAL). Similarly, calibration and measurement of dynamic responses of microthermocouples will be performed on these premises.

D. RESULTS TO DATE

(1) Thermal. Previous testing of probe step and pseudo-impulse responses conducted with pulsed and shuttered lasers in the USAF/SAM Laser Laboratory, suggests that the probe behavior approximates that of an RC filter with a time constant of about 50 msec, which is much slower than the time constant reported for these probes by Welch, et al.[4]

This discrepancy has been resolved as follows: The SAM/RAL preamplifier was taken to Dr. Welch's laboratory and tested with a single, new microthermocouple. With the probe aligned in air with respect to the center of a shuttered CW laser beam, results were very similar to the step responses measured in air at SAM/RAL. With experimental conditions the same, except with the probe surrounded by a static head of water contained in a glass beaker, the probe step response was roughly 100 times faster than that observed in air as above.

This finding is consistent with the significantly different set of boundary conditions for heat transfer which are generated in these two cases. For example, a term $K\underset{\sim}{\nabla} T$ (where K = thermal conductivity, $\underset{\sim}{\nabla}$ = gradient, T = temperature) enters into the equations for the boundary between the probe and its surround[12]. Other differences in heat transfer are caused by relative differences in convection and radiative absorption by the probe and its surround. It is interesting to note that the step response in biological tissue is roughly 150 times slower than that of pure water[13].

Thus, in general, one must be cautious of characterizing these microthermocouple probes as a simple RC filter whose response is independent of its surround. As seen in Figure III-2, a typical retinal temperature measurement, using a shuttered CW laser to irradiate the eye, is characterized by a rapid rise followed by a slow ascent; then a fast decay when the beam is interrupted, followed by a slow descent. Presumably the fast rise and decay segments of this curve are a consequence of radiative absorption and heat transfer within the probe itself[13], surrounded distally as it were by optically transparent tissue. Clearly the waveform in Figure III-2 cannot be modeled mathematically with a system containing a single time constant.

On the other hand the low pass behavior of such a system can be approximated reasonably well by considering that the thermal resistance and heat capacity of tissue and microthermocouple correspond, respectively, to electrical resistance per unit length R and capacitance per unit length C in a three-dimensionally distributed RC matrix. For convenience, Welch, et al.[4] assume that a single RC configuration with a time constant τ of 0.2 msec can be used

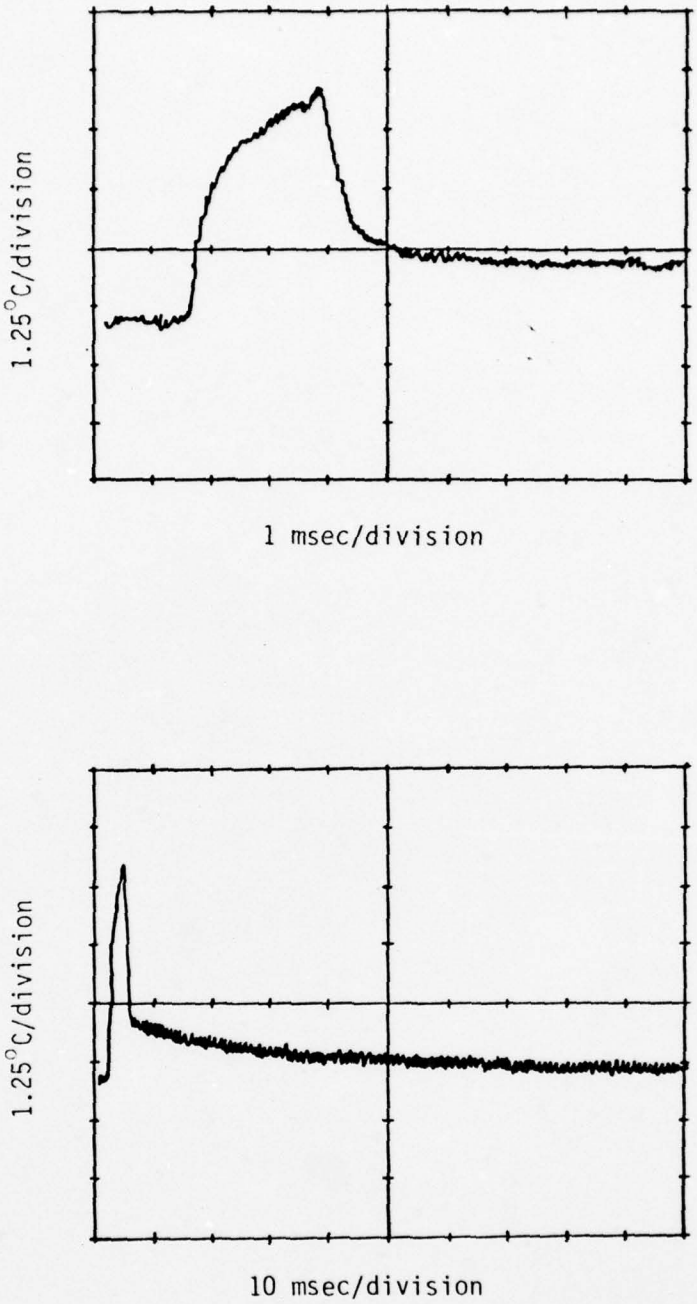


Figure III-2. Thermal responses of microthermocouple near pigment epithelium of rhesus monkey eye irradiated with argon laser. Upper and lower traces obtained at same location within eye, with differing time bases as shown, probe being slightly off center with respect to laser beam center. (Tracings from oscilloscope photographs.(13))

to characterize the sensor perturbation of tissue temperature measurements. To allow for heat transfer across additional boundaries of finite thickness between heat source and sensor, additional RC units must be added. In general the values of RC must be matched to each distinct layer in the heat conducting pathway. The addition of such RC units, however, causes additional attenuation and smoothing of recordings of temperature profiles outside the sensor.

For example, consider the attenuation of a signal (strictly speaking, the unit-normalized modulus of frequency response) passed by such simplified RC systems, as shown in Figure III-3. The case n = 1 corresponds to signal attenuation due to a single RC unit. Note that although for practical purposes, such a system equilibrates to a step temperature input in about 5 time constants (~1 msec), the signal components whose frequencies exceed 1.3 KHz are attenuated by over 50%. With n = 2,3,4, corresponding numbers of identical RC units are cascaded serially, loading being ignored[14], to simulate conditions in which additional layers or boundaries must be passed between temperature sensor and sensed environments.

It should be emphasized for the purpose of this report that the above models are not intended to provide precise quantitative predictions as to temperature waveform distortions in actual biological experiments; rather they purport to delineate in a broad sense the band pass limitations which are imposed upon experimental design and interpretation. Clearly additional experimental and theoretical work is needed on this very important point. However it is apparent that when laser repetition rates of more than 1-10 KHz and duty cycles of ~50% are used in biological experiments, special data processing

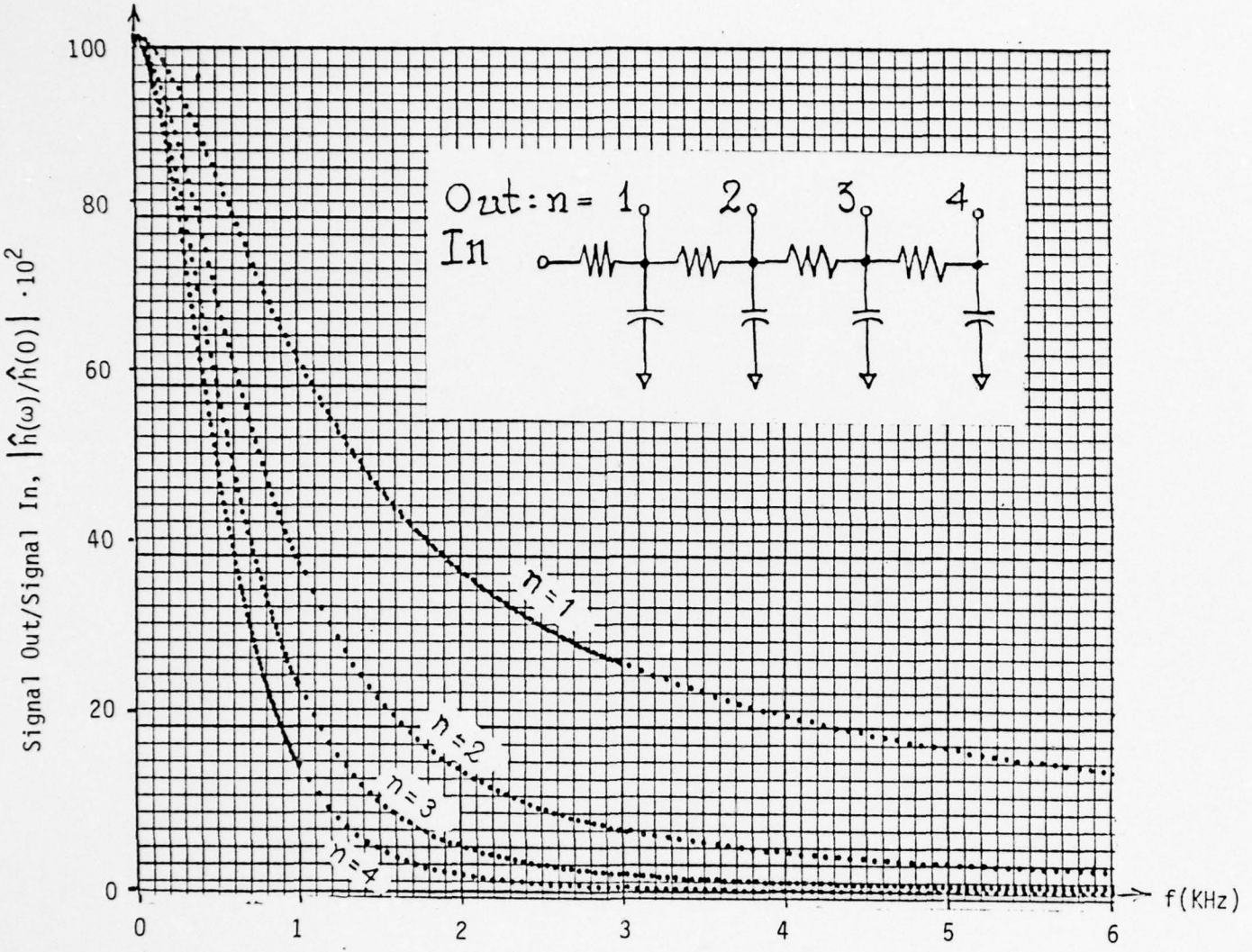


Figure III-3. Unit-normalized modulus of frequency response $\hat{h} = (a + j\omega)^{-n}$ vs. frequency $f = \omega/2\pi$, where $a = 1/\tau$ and $\tau = RC$, filter time constant; ω = angular frequency; and n = number of identical RC stages as shown in inset.

techniques to correct for sensor perturbation of temperature measurement are essential. Efforts are underway to provide these corrections and to understand more precisely the probe characteristics and limitations.

(2) Electrical. The SAM/RAL thermocouple preamplifier and amplifier system appears to have adequate stability, frequency response, and gain to make it a useful experimental tool, although certain design changes may be necessary. In particular, 60 Hz line noise was significant in one experiment when a functional microthermocouple probe, whose electrical resistance measured an atypically high value of ~1 K Ω, was tested for its dynamic response by exposing the probe in air to a shuttered He-Ne laser. Although the temperature stability of the preamplifier appears quite acceptable from an electronics standpoint, it would be convenient, although not essential, to have a separately controlled reference temperature junction to assist in interpretation of data when displayed on-line with a storage oscilloscope. In any case, the reference junction temperature must be measured as part of routine data collection. In addition, it is necessary to determine whether the noisy substrate of wet, exposed biological tissue will necessitate floating differential inputs across the microthermocouple leads.

The control logic to drive the shutter, probe, and beam deflector appears to have sufficient latitude for exploratory purposes. However, the linearity and reproducibility of the beam deflector and probe driver have not yet been tested. As discussed in Section 3, an improved beam deflector system must be designed and built before meaningful measurements can be obtained. Depending upon the criterion for spatial data resolution, use of a single photodiode scanner to calibrate deflector positions of an unmodulated laser beam may be

inappropriate for this particular task; a sufficiently accurate calibration is likely to require a quadrant-differential detector array. One such system, which should be capable of measuring beam positions well within ±5 μm and possibly ±0.5 μm has been designed (see Appendix III-A for details).

Twelve microthermocouples, which had been provided by the University of Texas some twelve months previous, were tested with a newly designed[15] electrical resistance measuring circuit (see Appendix III-B for circuit details and diagram). Probes which had resistance values between 200Ω and 1.1KΩ were found to generate linear EMF's when equilibrated to temperature steps in a water bath. A dissecting microscope was used to visualize the probe tip; with appropriate alignment of a camera above the microscope tube with one ocular removed, it was found that acceptable photomicrographs can be readily obtained for documentation of probe size and shape.

In the future, the above resistance measuring device and auxiliary microscope system will be used as a quick, presumably non-destructive check on all new batches of microthermocouples obtained from the University of Texas. In addition, acceptable probes subsequently damaged, either in use or as a consequence of a possible limited shelf life, can be checked out against these initial values before and after an experiment.

(3) Optical. In the beam deflector designed by Crum[11], a cam was machined to ride against a roller and mount which carries a beam-deflecting pellicle. The geometry of this cam is based upon an assumed paraxially-incident laser beam, which is subsequently deflected by the pellicle through a fixed point in or at a dilated, relaxed eye of an animal. Thus, the eye, accomodated to focus at infinity, images the incoming beam at the retina,

forming a small diffraction patch whose central disc diameter is typically on the order of the probe tip diameter.

Clearly the size of the temperature sensor, located at the probe tip, is a limiting factor as to how small the laser beam can be without producing significant attenuation and smoothing of spatial temperature profiles, as well as probe radiometric scans of the image intensity of the beam. One expects from Fourier analysis (see Appendix III-C) that the diameter of the diffraction disc should be larger than the diameter of the sensor by a factor of at least 10, which necessitates that the laser beam be incident on the eye either in a converging or diverging fashion.

For example, if the laser beam is focused at certain distances in front of the eye, it will have an enlarged diameter at the retina whenever the geometric focus of the beam inside the eye is proximal to the retina. Alternatively one may focus the laser beam near the pupil of the eye (Maxwellian view), with the cone angle for the converging beam so chosen that an appropriate beam diameter intersects the retina. The size of this beam intersection is readily calculated to a first approximation from standard lens formulae. Thus additional laser optics could be added conveniently to the present system to expand the retinal image of the incident beam. However, unless this optical system either is interposed between the eye and pellicle or is translated axially to about the same extent as the pellicle, the retinal beam size will be dependent upon deflector position.

Moreover, due to optical aberrations within the eye, the beam intensity distribution is not translationally invariant with respect to arbitrary displacements of the beam on the retina. Hence one should not assume <u>a priori</u> (a)

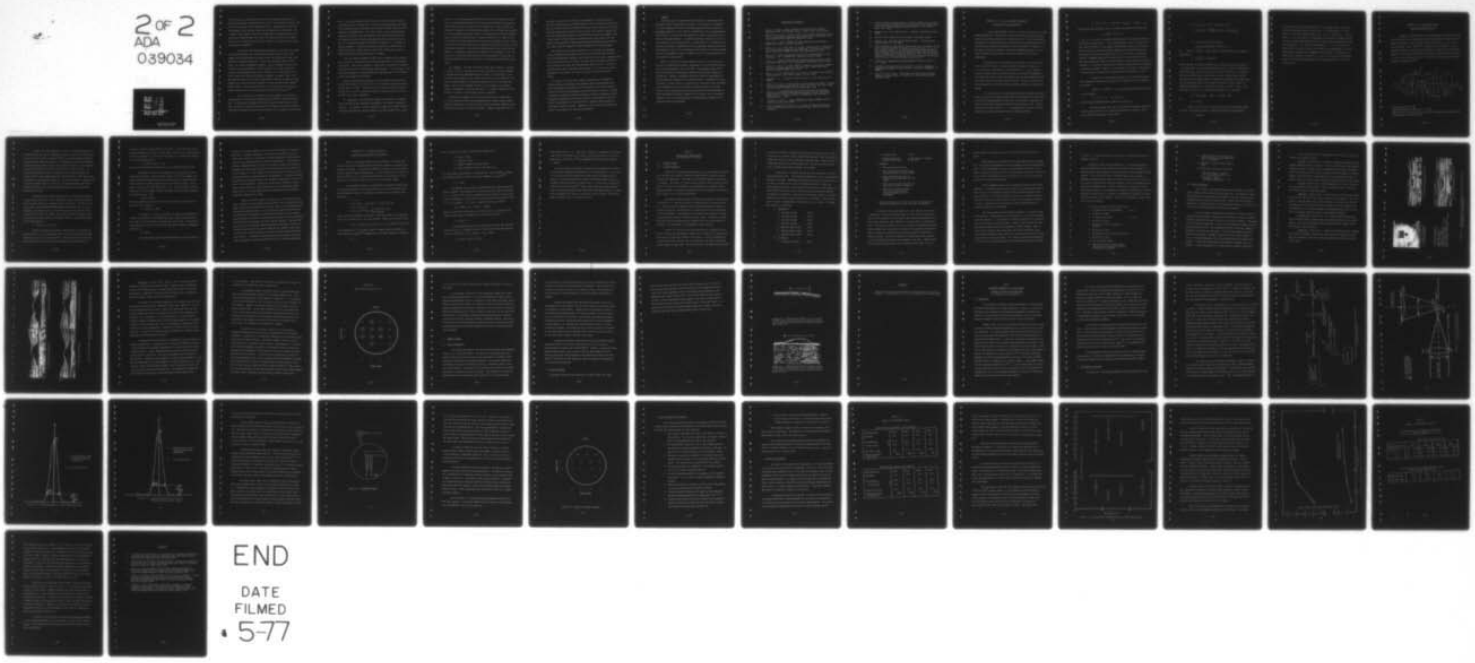
that the initial radial symmetry of the beam intensity distribution in air is not distorted at the retinal level, or (b) that equal angular displacements of the beam in air remain equally spaced at the retina. Fortunately these effects are measured readily with the newly designed optical system, as discussed briefly below.

In addition, we may use a general three-dimensional ray tracing program currently being developed[16], to provide both an independent check on the above translational invariance for particular choices of beam width, inclination and divergence, and by extension, a useful tool for correcting and optimizing the present beam deflector design. Briefly, each ray is assigned an initial set of space coordinates and direction cosines; then it is traced through each (spherical) surface in the optical system, and specified at a given observation plane or at a concave surface which represents the retina. The principal advantage of this method, based upon simplification of a technique devised by Spencer,[17] is the ease with which both meridional and skew rays can be traced; effects of lens aberrations are calculated precisely. This method can be extended readily to include aspherical surfaces, Fresnel coefficients, light polarization, and intensity. At present, minicomputer software is being written for simple two-dimensional test cases to insure that the method is working properly.

The condenser optics to illuminate the fundus have also undergone some modification, initially to decouple the laser optics from the condenser optics, as well as to increase the distance between the beam deflector pellicle and the ophthalmoscope lens assembly used by Crum.[11] This was accomplished in prototype form (a) by replacing the ophthalmoscope prism with a

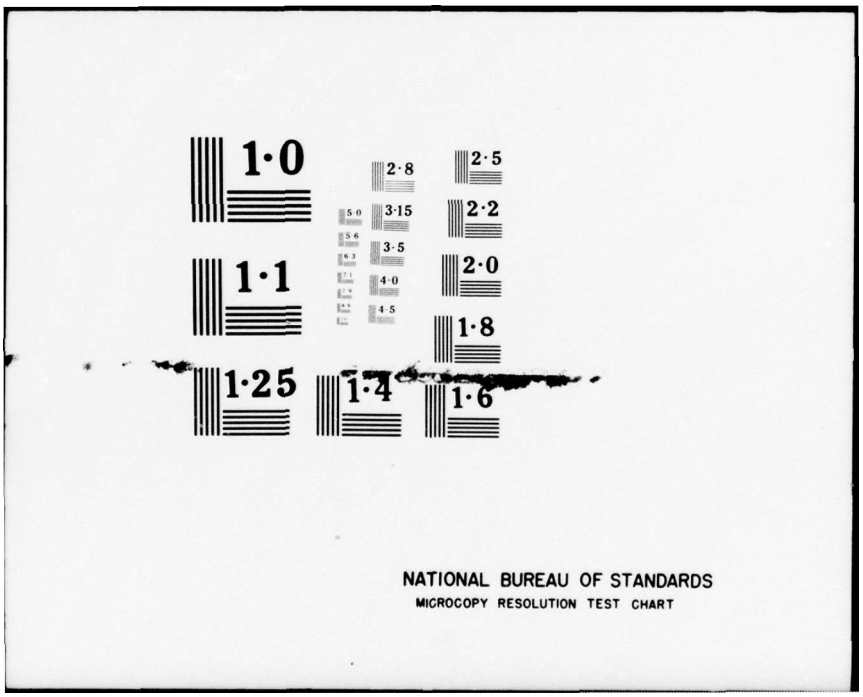
AD-A039 034 TECHNOLOGY INC SAN ANTONIO TEX LIFE SCIENCES DIV F/G 6/18
RESEARCH ON THE OCULAR EFFECTS OF LASER RADIATION.(U)
FEB 75 J S CONNOLLY, J A ZUCLICH F41609-73-C-0017
UNCLASSIFIED TI-75-0561-02 NL

2 OF 2
ADA
039034



END

DATE
FILMED
5-77


1·0
1·1
1·25
1·4
1·6
1·8
2·0
2·2
2·5
2·8
3·15
3·5
4·0
4·5
5·0
5·6
6·3
7·1
NATIONAL BUREAU OF STANDARDS
MICROCOPY RESOLUTION TEST CHART

45° slanting mirror through which was drilled an elliptical hole and (b) by replacing the aspheric ophthalmoscope lens with a large biconvex condenser lens with a circular hole drilled through the center. Both apertures can be made large enough to pass the laser beam without attenuation or diffraction. The f number of the condenser lens was so chosen that it closely matches that of the original ophthalmoscope lens; hence, the working distance was increased about five times without sacrificing the intensity or reducing the cone angle of the fundus illumination.

It was also found that by placing crosshairs in the back focal plane of the large condenser lens, the crosshair image within the retina of one monkey could be aligned with the center of the laser beam retinal image, thus providing a convenient method for aligning the laser with respect to the probe. For routine experimental purposes, a coarse alignment is quite satisfactory since fine adjustments in animal position can be made using probe responses to subthreshold laser pulses. However, it is interesting to note that in those cases where precise animal alignment is needed or where it is desirable to measure certain optical aberrations of the eye in vivo, this same method can be refined by adding crosshairs or other patterns within whatever optical system is used to inspect the eye; such fixed patterns may be used to measure the deviation of matching patterns projected into the eye.[18]

In the interest of facilitating a quick alignment of a surgically exposed animal to the binocular ophthalmoscope, additional changes were necessary. A beam steerer was added and the entire optical system raised so that the laser beam axis and the surface normal of the deflecting pellicle defined a plane which coincided closely with the horizontal axis of rotation of the animal

mount. Thus by adjusting the animal position so that the eye more nearly coincided with this rotational axis, tilting of the animal mount had a much less pronounced effect in displacing the condenser filament image and in defocusing the ophthalmoscope. For similar reasons, and to provide greater mechanical stability in the beam deflector (see next section), the latter was decoupled from the binocular ophthalmoscope which otherwise had to be left in a fixed position while the animal was lined up to it, a rather cumbersome procedure. In addition, the present system has no precise way to adjust the pellicle surface normal to stay within a given plane, such adjustment requiring an additional degree of freedom.

It has also proved convenient to add a small alignment mirror perpendicular to the axis of that portion of the laser beam which is transmitted by the pellicle. With proper alignment, a small part of this beam is reflected along the optical axis of the binocular ophthalmoscope. In this fashion a fast, very precise method for lining the binocular ophthalmoscope to the decoupled pellicle and condenser was obtained.

Finally the He-Ne laser presently in use was checked to insure that it was not mode locking; the cavity mirrors were cleaned and aligned to provide maximum output (~100mW). Subsequent beam scans indicated that some type of spatial filtering will be needed to symmetrize the beam and purge it of undesirable high spatial frequencies.

(4) Mechanical. One significant problem which remains to be solved before reliable retinal temperature measurements can be made is mechanical stability. For example, in order to project an image of the fundus into the binocular ophthalmoscope, the beam deflector has been designed with a large

pellicle. The vibrational sensitivity of this pellicle is readily discerned with a single photodiode detector lined up with the deflected laser beam axis and situated close to the position of the subject eye. Hence, acoustic and mechanical vibrations, caused by ordinary speech a few feet away from the pellicle, and by bumping the optical bench or its accessories, are readily detected. Similar results are obtained when a relatively heavy mirror is used in place of the pellicle and then the bench and accessories are bumped as above. Hence, part of this vibrational sensitivity is apparently also due to the small, coiled spring which maintains a light tension between the roller and cam of the beam deflector. In general, the mechanical supports of the componerts in this system are not sufficiently vibration-free to take advantage of in vivo data resolution capabilities which, in principle, can be achieved with current technology.

(5) Surgical. The other significant problem which remains is surgical in nature. To date, two exploratory surgery experiments have been conducted in collaboration with USAF/SAM veterinary surgeons to familiarize us with the tools and equipment for eye surgery and to help define an effective, minimally traumatic method for exposing the posterior orbit of the right eye, making a small incision through the sclera, and implanting a microthermocouple. Subsequently a visit was made to Dr. A. J. Welch's laboratory at the University of Texas to observe their surgical techniques.

Tentatively it appears that the eye can be rotated far enough nasally so that the posterior orbit can be penetrated with a thermal probe, without extensive compression or excision of brain tissue and without otherwise stressing the eye tissue by occlusion or stretching. However, additional work is

required on this point, in particular by examination of more than two animals with a fundus camera or ophthalmoscope. It may be necessary to suture the eye to a fixation ring since suturing the cornea or ocular muscles to tie bars at several points did not stabilize the eye over a long period. However, for short term exploratory purposes, suturing the eye as above was adequate, since it was possible in both instances to penetrate the retina and PE with trial probes; these consisted of inexpensive glass microelectrodes whose tip diameter, shape, and bulk properties closely resembled the microthermocouples.

Verification that one such electrode was in the retina and reasonably close to the macula was achieved as follows: after inserting the electrode with a micromanipulator through a tiny (<1 mm) slit in the sclera, obtained with a razor knife and surgical microscope, light was piped by internal reflection from a bright source above the electrode shank down to the tip. Then by inspecting the eye with a hand-held ophthalmoscope, it was possible to locate the probe as a thin pencil of light in relation to the position of the macula.

In the near term, additional surgery experiments will be needed to further define our methodology, with emphasis upon finding the most expedient and mechanically stable way to fix the head, the eye with respect to the head, and the microthermocouple probe with respect to the eye. In order to identify the hardware needed to accomplish this goal, preliminary retinal temperature measurements are obviously required, even though all other mechanical requirements are not yet fulfilled. Obviously good technique in microsurgery requires practice. However, our early success with substitute probes in this respect has been most encouraging.

E. SUMMARY

Additional tools and equipment must be procured or fabricated before meaningful retinal temperatures can be made. In the interest of expediency, certain mechanical and optical design changes have been assembled in a *pro temps* system and are now ready for incorporation into an improved experimental system. A critical design problem still remains, namely the configuration of the beam deflector. In addition, mechanical stability of the entire system must be increased greatly. At this point, it is essential to decide what constitutes reasonable limits on *in vivo* data resolution both from the standpoint of what can be accomplished with respect to current technology, and from the standpoint of what is needed to verify or negate predictions of the theoretical thermal model.

However, it should be strongly emphasized that it is not necessary to wait for all mechanical and optical requirements to be fulfilled before certain retinal measurements can be initiated. The *pro temps* system will be used to further define experimental procedures for the gross surgery and implantation. Moreover, reasonably simple fabrication or procurements to increase mechanical stability of the present system, if mounted on an isolation table or granite block, will permit certain long-pulse laser experiments to be conducted as soon as our surgical techniques measure to the task. Finally, this interim period will be used to improve the beam deflector; to devise appropriate calibration methods for this system and its individual components; and to investigate dynamic microthermocouple responses and related data processing techniques.

REFERENCES AND FOOTNOTES

1. Cain,C. P. and A. J. Welch, "Measured and Predicted Laser-Induced Temperature Rises in the Rabbit Fundus," Invest. Ophth. 13, 60 (1974).

2. Hemstreet, H.W. et al., "Ocular Hazards of Picosecond and Repetitive Pulse Lasers," Technology Incorporated, Second Annual Report (March 1975), Contract F41609-73-C-0016, USAF SAM, Brooks AFB, Texas.

3. Geeraets, W. J. and D. Ridgeway, "Retinal Damage from High Intensity Light," Acta. Ophth. Supp. 76. 109 (1963).

4. Welch, A. J., C. P. Cain, and L. A. Priebe, "Investigation of Temperature Rise in the Fundus Exposed to Laser Radiation," Final Tech. Rpt. (May 1974), Contract No. F41609-73-C-0031, USAF SAM Brooks AFB, Texas.

5. Reed, R. P. "Thin Film Sensors of Micron Size and Applications in Biothermology," Ph. D. Dissertation, University of Texas (1966).

6. Cain, C. P. "Dynamic Spatio-Temporal Temperature Measurements in Laser Irradiated Rabbit Eyes," Ph.D. Dissertation, University of Texas (1972).

7. Welch, A. J. and L. A. Priebe, "Model of Thermal Injury Based on Temperature Rise in Fundus Exposed to Laser Radiation," Interim Tech. Rpt., Contract F41609-74-C-0025 (Sept. 1974).

8. White, T. J., M. A. Mainster, J. H. Tips and P. W. Wilson, "Chorioretinal Thermal Behavior," Bull. Math. Biophys. 32, 315 (1970).

9. Henriques, F. C., "Studies of Thermal Injury," V., Arch. Path. 43, 489 (1947).

10. Takata, A.N., et al., "Thermal Model of Laser-Induced Eye Damage," Illinois Institute of Technology Research Institute, Final Tech. Rpt. (Oct. 1974), Contract F41609-74-C-0005, USAF SAM, Brooks AFB. Texas.

11. Crum, C. G., "An Experimental Apparatus and Procedure for Obtaining Dynamic Spatio-Temporal Temperature Measurements in Laser Irradiated Monkey Eyes," M. S. Thesis, School of Engineering, USAF Institute of Technology (Dec. 1973).

12. Carslaw H. S. and J. C. Jaeger, Conduction of Heat in Solids, 2nd ed., Oxford University Press (1959).

13. Personal communications from Mr. L.A. Priebe, Bio-Medical Engineering Research Laboratory, Electronics Research Center, University of Texas at Austin.

14. Strictly speaking, loading cannot be ignored although for our purposes here an accurate characterization is not required. See Chapter III of Close, Chas. M. The Analysis of Linear Circuits, Harcourt, Brace & World, Inc. (1966).

15. Nawrocki, A.D., R.W. Thompson and R.F. Lemberger, unpublished results (1974).

16. Details of this method will be discussed in subsequent reports.

17. Spencer, G.H. "A General Ray Tracing Procedure," IBM Corporation Research Paper, RC - 549 (1961).

18. Proof-of-concept was obtained by using a small lens to simulate the eye with a small grid pattern in the back focal plane of this lens. As this lens was rotated, it was possible to observe effects of coma by first aligning crosshairs and then measuring displacement of the projected crosshairs as a function of rotational angle. By interpolation between division marks, approximately 100 μm displacement was observed when this lens, initially centered, was rotated by 7^{o}.

19. Goodman, J.W. Introduction to Fourier Optics, McGraw Hill Book Co., N. Y. (1968).

20. Calculated from tabulated values of Bessel Functions, Handbook of Mathematical Functions, National Bureau of Standards, Washington, D.C. (1964).

21. Stein, M.N. and S. Elgin, "Measurement of Retinal Image for Laser Radiation in Rhesus Monkey," Final Rpt. No. F41609-68-C-0038-6301 (February, 1970).

APPENDIX III-A: Limits of Scanner Resolution and Detector System Sensitivity

1. In the present SAM/RAL system for scanning a laser beam, a single photodiode detector is displaced in one or two directions within a given perpendicular plane with respect to the sampled beam axis. This single detector configuration is quite satisfactory for characterizing the shape and size of a particular laser intensity distribution, but as shown below, in general it is not nearly as precise a method as two or more photodiodes whenever it is required to measure the beam center, particularly when the laser beam is unmodulated.

We assume that a laser intensity distribution, I, may be given by $I(\rho) = \exp(-k\rho^2)$, where ρ = radial coordinate orthogonal to beam axis, $k = 2/\rho_2^2$ and ρ_2 is the radius at the $1/e^2$ points, i.e., $I(\rho_2) = \exp(-2)$. Further we assume that all sensing, amplifying, and recording components of this system are linear and that the detector aperture which samples the beam is so small that we can ignore spatial filtering. Likewise we assume that the scan speed is so slow that we may approximate sampling as a quasi-static process.

2. In the case of a single photodiode detector system, while scanning $I(\rho)$ as we try to locate the beam center corresponding to a peak reading at $I(0)$, we assume measurement sensitivity to be limited to some value, ΔI, taken as the smallest detectable reduction from the peak at $I(0)$. Then at some small off-center position $\rho = \varepsilon$, corresponding to the limit of spatial resolution for locating the beam center, we have the relation:

$$\Delta I = I(0) - I(\epsilon) = 1 - \exp(-k\epsilon^2) \simeq 2(\epsilon/\rho_2)^2 \qquad (\text{where } \epsilon << \rho_2).$$

Alternatively the resolution limit is related to measurement sensitivity by

$$|\epsilon| \simeq \left(\frac{\Delta I}{k}\right)^{\frac{1}{2}} \simeq 0.71\rho_2 \sqrt{\Delta I}.$$

If, say, ρ_2 = 1 mm and ΔI is between 0.0001 and 0.01, then the beam center can be resolved to within about ± 7 to 70 μm, respectively. Thus, to resolve the beam center to within ± 10 μm, detector system sensitivity must be capable of sensing ~0.01% roll-off from the peak reading for fairly typical beam sizes. Experience with laser scans suggests that $|\epsilon|$ ~15 to 20 μm is a reasonable value for unexpanded beams, which implies that ΔI is on the order of 0.001. Note that expanding the beam in a naive attempt to improve resolution actually decreases it, since the curvature of the intensity peak becomes less pronounced as the beam is expanded. However, for sufficiently small beams, this decrease is compensated by the resulting increased precision in measuring ρ itself.

3. Instead of a single detector system, let us consider two detectors connected differentially to produce a null condition at $I(0)$, defined by the relation:

$\lim_{\epsilon \to 0} [\Delta I] = 0$, where $\Delta I = I_1 - I_2$ and where detector inputs I_1 and I_2 are defined by:

$$I_1 = I(-\rho_n + \epsilon), \qquad I_2 = I(\rho_n + \epsilon);$$

and the distance between detector centers is given by $2\rho_n$.

As in the previous case, let ΔI be a measure of detector system sensitivity, forcing the limit to resolution defined by ϵ to assume a finite value, implicitly contained in the relation:

$$\Delta I = \exp\left[-k(-\rho_n + \varepsilon)^2\right] - \exp\left[-k(\rho_n + \varepsilon)^2\right]$$

$$= \exp\left[-k(\rho_n{}^2 + \varepsilon^2)\right]\left\{\exp\left[2k\varepsilon\rho_n\right] - \exp\left[-2k\varepsilon\rho_n\right]\right\}$$

or:

$$\Delta I = 2I(\rho_n)\exp\left[-k\varepsilon^2\right]\sinh\left[2k\varepsilon\rho_n\right]$$

$$\simeq 4k\varepsilon\rho_n I(\rho_n) \text{ provided } k\varepsilon^2 \text{ and } 2k\varepsilon\rho_n \ll 1.$$

But $(\partial I/\partial\rho)_\varepsilon = -2k\rho I(\rho)$. Hence, subject to the conditions in the approximation above:

$$\Delta I = 2\varepsilon\left|\left(\frac{\partial I}{\partial\rho}\right)_\varepsilon\right| = 8\varepsilon\rho I(\rho)/\rho_2{}^2.$$

Clearly the rate of change of detector system sensitivity per unit change in ε is proportional to the partial derivative $(\partial I/\partial\rho)_\varepsilon$ so that to maximize beam center resolution, we must find that ρ_n for which $(\partial^2 I/\partial\rho^2)_\varepsilon = 0$. Therefore, for the same limitations in sensitivity as in the single detector system, resolution in the present instance is maximized by spatially tuning two detectors to the maximum slope of the intensity distribution $I(\rho)$, namely, by separating the detectors by the amount $2\rho_n$, where $\rho_n = (2k)^{-\frac{1}{2}} = \rho_2/2$. Substituting this value of ρ_n into the last equation for ΔI, we obtain:

$$\Delta I \simeq 4\varepsilon I(\rho_2/2)/\rho_2 \quad \text{where} \quad I(\rho_2/2) \simeq 0.61$$

or:

$$\Delta I \simeq 2.4\varepsilon/\rho_2.$$

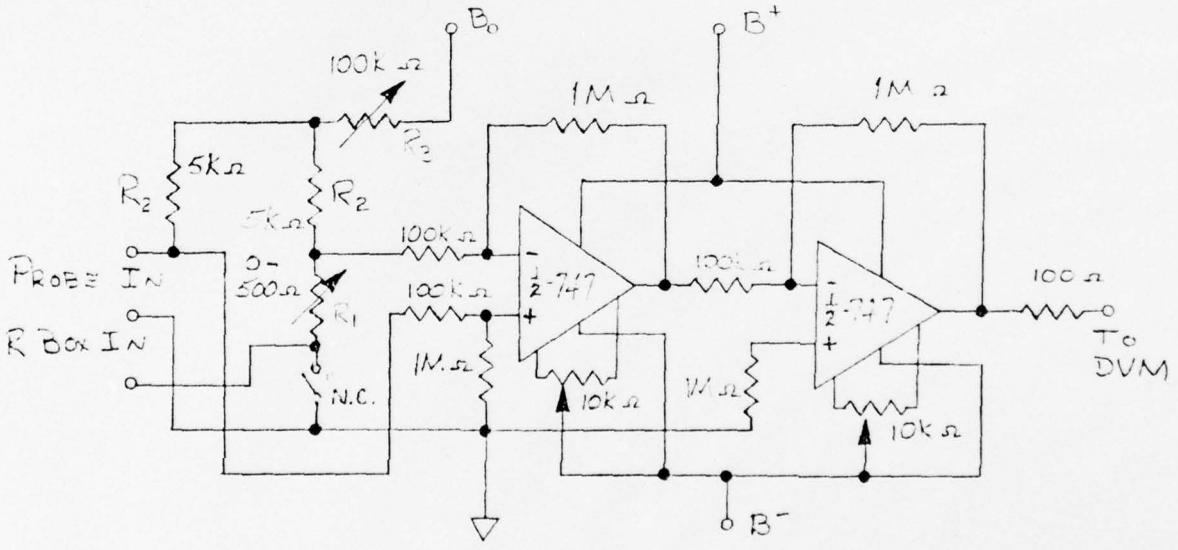
Hence, by solving for ε explicitly, we see that the maximum resolution for a two detector system is related to measurement sensitivity by:

$$\varepsilon \simeq 0.42\rho_2\Delta I.$$

Note that although the linear dependence of ε upon beam radius ρ_2 is similar to that of the single detector system, here ε is proportional to ΔI, as opposed to $(\Delta I)^{\frac{1}{2}}$ in the single detector case. For $\Delta I \simeq 0.001$ and $\rho_2 \sim 1$ mm, we have $|\varepsilon| < 1$ μm; this implies an improvement in resolution of roughly 20 times over that of unmodulated single detectors, without adding substantially to the system complexity. For resolution requirements $|\varepsilon| \sim 5$ μm, one may also expand the beam in order to improve the precision in the measurement of ρ itself. Obviously this two-detector arrangement may be expanded to 4 equidistant detectors whose diagonals are equal to $\rho_n = \rho_2/2$; in so doing, the distribution center can be measured orthogonally within a plane perpendicular to the distribution axis.

APPENDIX III-B: Microthermocouple Resistance Measuring Circuit

Although a thermocouple is a voltage generator, measuring its resistance R_p provides a quick, convenient method for checking the integrity of the bimetallic junction: shorted leads are suspected when $R_p << 100\Omega$, a faulty junction when $R_p > 500 - 1000\Omega$.[13] Apparently, the resistance of freshly fabricated probes can be measured with a typical, commercially available VOM; however, circuit-induced electrical heating of the probe should be minimized by using a more conservative circuit. The bridge circuit shown below appears to meet our requirements.[15]



Bridge supply (B_0) = 5 VDC
Operational amplifier supply ($B^{\pm}$) = ± 12 VDC
Input terminals soldered to probe leads and 0-10 megohm decade resistance box
Output terminals connected to DVM

Briefly, the circuit operates as follows: the bridge supply B_o is connected across the legs of a Wheatstone bridge consisting of current shunts R_2 in series with R_3 and of variable resistor R_1, used to balance the probe resistance which forms the fourth leg. In those cases where probe resistance exceeds the normal bounds of <500Ω, the ground connection of R_1 can be opened to permit the addition of a decade resistance box in series with R_1. The bridge output between the probe to ground and the variable resistance to ground is fed to two cascaded operational amplifiers with a total gain of 100, energized by a separate power supply B±. The amplified output is measured with a digital voltmeter (DVM). The DC off-set of each operational amplifier is nulled by grounding its input and adjusting the 10K pot, the output being measured with the DVM.

Experiments with a decade resistance box to simulate the probe resistance were performed to maximize measurement sensitivity while minimizing heat dissipation within the simulated probe resistance R_p. With the circuit values shown, using a Weston 4444 DVM capable of resolving ± 10 μV, current through R_p was constant at 92 ± 1 μA when the bridge was nulled for each of successive variations in R_p between ~10Ω and 10KΩ. Hence at balance, using probes whose resistance values are considered "normal", the heat dissipation by the probe should be:

$$< (93\ \mu A)^2 \times (1K\Omega) \simeq 9\ \mu W.$$

Another experiment was directed at how much heat is dissipated by the probe when it is first connected to the circuit with an arbitrary bridge imbalance being set up by such connection. With the variable resistance (R_1 and resistance box) fixed at 625Ω, the simulated probe resistance R_p was

varied in successive steps between 8Ω and 9.9 MΩ. In all cases the current measured through R_p was <110 μA. Hence, when a probe is first connected, without prior knowledge of its electrical resistance, we can expect heat dissipation in normal probes to be:

$$< (110\ \mu A)^2 \times (1K\Omega) \simeq 12\ \mu W,$$

when the variable balancing resistance is set at 500-600Ω before nulling.

Measurement sensitivity was adjusted by varying the gain of the operational amplifiers. With the values shown in the circuit diagram, the bridge imbalance was determined for successive values of R_p between 8Ω and 9.9 MΩ, while the variable resistance was fixed at 625Ω as above. In the range of interest for normal probes, $100\Omega < R_p < 1K\Omega$, the change in bridge imbalance ΔV per unit change in probe simulated resistance ΔR was calculated from measured values to be:

$$\Delta V/\Delta R < 0.3mV/\Omega.$$

Since the bridge amplifiers had a gain of 100, measurement sensitivity for this circuit M is given by:

$$M = 100\Delta V/\Delta R < 30mV/\Omega.$$

For example in a similar experiment, the output of the DVM was observed to vary between -270 and 280mV when R_p was varied successively from 477 to 537Ω, while the variable resistance was fixed at 514Ω. Thus when the bridge imbalance is close to a null, under the above conditions, measurement sensitivity is:

$$M \sim 9mV/\Omega.$$

In actual thermocouple resistance measurements, the probe leads are

soldered to the input terminals of the circuit and the probe is immersed in a water bath at constant temperature. The variable resistance R_1 is set to ~300Ω; after a delay of a few minutes to permit temperature equilibration of the probe, the bridge imbalance is nulled by adjusting R_1. If the probe resistance is abnormally high, so that a null cannot be found, the switch may be opened after the decade resistance box has been connected to appropriate circuit terminals. In this fashion a null can be found by setting R_1 to 500Ω and increasing the resistance values of the decade box. The probe resistance is equated to the measured value of the variable resistance, plus or minus the error in this measurement. Sufficient accuracy may be obtained by using a linear 10-turn pot for R_1, thus providing the circuit with direct reading capability; or, as in the present case, by simply measuring the variable resistance separately with a VOM.

Hence, we have the option of setting R_1 to a fixed value and the output voltage is within expected upper and lower limits, indicating that the probe is functional irrespective of its exact value; or we may measure probe resistance as described above. Until we gain more experience with the use and limitations of the present microthermocouple probes, we will continue measuring probe resistance to establish upper and lower limits by correlating resistance with probe dynamic and static thermal responses. Assurance that this circuit is not degrading these probes during measurement has been obtained by observing that the output voltage has not changed by more than a few millivolts, on the average, over periods of several minutes before and after nulling. In addition, we have observed no differences in the microscopic appearance of the probes before and after a resistance measurement.

APPENDIX III-C: Spatial Filtering of Gaussian Distribution by Finite Detector

Ideally, the sensing element of an area detector is so small that spatial filtering of the sensed environment may be ignored at all spatial frequencies of interest. To account for possible filtering of a Gaussian temperature or radiant intensity distribution, I, using an equation for I similar to that in Appendix III-A, we assume that transduction by each element of area generates an unweighted, linear contribution to the detector output.

This assumption allows us to characterize the detector output power $\dot{E}$ as being proportional to the convolution (*) of I(x,y) with detector area, which corresponds physically to stepping the detector across the beam quasi-statically:

$$\dot{E} \propto I * C;$$

$$I \propto \exp\left[-k(x^2 + y^2)\right] \text{ where } k = 2/\sqrt{x_2^2 + y_2^2} \text{ and}$$

$$I(x_2,y_2) = \exp(-2);$$

$$C \equiv \text{circ}\left[2\sqrt{x^2 + y^2}/D\right] = \begin{cases} 1, & |\sqrt{x^2 + y^2}| \leq D/2 \\ 0, & \text{otherwise.} \end{cases}$$

Here x and y are rectangular coordinates in the plane normal to the distribution axis at I(0,0) and D is the probe diameter. Hence, we have the relation:

$$\dot{E}(x,y) = \int_{-\infty}^{\infty}\int d\xi d\eta \exp\left[-k(\xi^2+\eta^2)\right] \text{circ}\left[2\sqrt{(x-\xi)^2 + (y-\eta)^2}/D\right].$$

The counterpart of $\dot{E}$ in the radial spatial frequency domain, obtained by a Fourier-Bessel transform[19] (denoted FBT) of the above equation, is given by:

$$\hat{\dot{E}} \propto \hat{I}\,\hat{C}.$$

Here (^) refers to the FBT of the respective quantities and

$$\hat{I} \propto \exp(-\pi^2 f^2/k);$$

$$\hat{C} \propto J_1(\pi D f)/f; \text{ where}$$

f = spatial frequency (cycles/μm) and

J_1 = Bessel function of first kind, order zero.

$\hat{E}$ is thus simply proportional to $\hat{I}$ attenuated by $\hat{C}$, which resembles a damped cosine function with its first zero at some frequency f_o given by[20]

$$f_o = 1.22/D.$$

An estimate for the largest acceptable detector diameter may be deduced as follows. The transform $\hat{C}(f)$ rolls off by no more than 0.9 $\hat{C}(0)$ when $f \leq f_1 \sim 0.235\ f_o$.[20] Thus $\hat{E}$ is attenuated by less than 10% for most significant low frequencies if this roll-off occurs beyond the $1/e^2$ points of $\hat{I}(f)$, i.e., at a frequency $f \geq f_b = 2/\pi\rho_2$. Equating f_1 and f_b, we obtain:

$$f_b = 0.637/\rho_2 = f_1 \sim 0.235\ f_o \sim 0.286/D.$$

Hence, to insure that the detector is not filtering $I(\rho)$ significantly, we expect that the ratio R of diameters $2\rho_2$ and D must be at least

$$R = 2\rho_2/D \sim 4.$$

A conservative value for R is obtained by insisting that the first zero of $\hat{C}$ occur at a frequency at least 10 times greater than that obtained at the $1/e^2$ points of $\hat{I}$, i.e., when $f_o \geq 10\ f_b$. Hence:

$$f_o = 1.22/D > 10 f_b = 6.37/\rho_2,$$

which implies that $R > 10$. Under these conditions, $\hat{C}$ attenuates $\hat{I}$ by no more than 2% for all frequencies less than f_b, and by no more than 3.1% for frequencies less than $\sqrt{2}\, f_b$, [20] corresponding to the $1/e^4$ points at which $\hat{I} \sim 0.018$.

It may be possible to correct for spatial filtering when say $4 < R < 10$, by using certain mathematical techniques such as deconvolution. In any case it is clear that results obtained with probes whose tip diameters are as small as 10 μm must be suspected of spatial filtering whenever the laser is incident on the cornea from an extended source: in particular, calculations from data by Stein and Elgin[21] indicate that the retinal image diameters ($2\rho_2$) of freshly enucleated rhesus monkey eyes range between 30-50 μm. Hence, with an extended laser source, we can expect R not to exceed a value 5 when probe tip diameters are on the order of 10 μm.

PART IV

HISTOLOGICAL INVESTIGATIONS

W.H. Bowie and J.A. Zuclich

A. RETINAL LESIONS

(1) Tissue Preparation

Animals to be necropsied and whose eyes are to be studied are delivered to the Veterinary Science, Pathology Branch (SAM VSP) previously anesthesized by the investigator. The animal is administered additional anesthetic if necessary. Two liters of fixative and two liters of normal saline are prepared. The fixative is composed of 2% glutaraldehyde in cacodylate buffer. Cacodylate buffer is composed of dimethylarsinic acid (cacodylic acid) adjusted to a pH of 7.2-7.4 with sodium hydroxide.

The bottles containing these solutions are attached to a common piece of tubing by a "Y" connector and each is clamped between the bottle and the "Y". A pressure source (compressed air) and a pressure gauge are then connected to the system. The body cavity is opened from the top of the sternum to the lower abdomen. The diaphragm is dissected from the body wall and the organs carefully displaced to reveal the dorsal aorta. A ligature is passed around the aorta and tightened, thus preventing blood flow to the lower extremities. The pericardium is then opened to reveal the heart.

A small slit is made in the left ventricle and a serrated hose connector is forced into the opening. Another slit is made in the right auricle and pressure is then slowly applied to the bottles. Saline is subsequently forced into the left ventricle and is circulated via the normal circulatory system through the upper body. This solution clears the blood from the system,

the progress of which is judged by the clarity of the venous return. When a virtually clear solution is being expelled from the heart, the saline flow is stopped and fixative is then circulated through the body. Proper fixation is assured when the animal's muscles become firm. At this point the fixative flow is stopped and the tubing removed from the heart.

The bony orbit is removed from the skull and the eyeball carefully dissected from the orbit. This method was developed to lower the probability of damage to the eye. Immediately upon removal, the globe is placed in fixative and, as quickly as practicable, is hemisectioned with a clean, new, double-edged razor blade. The posterior half of the eye is then immersed in cold, buffered fixative for one to two hours and then transferred through two changes of cold buffer. After the last buffer wash, the eye is carefully trimmed to remove excess tissue from the area of the macula. The resulting piece of tissue is approximately 5 mm wide and 1 to 1.5 cm long. The embedding sequence is as follows:

A. Dehydration

1.	50% ethyl alcohol	15 min
2.	70% ethyl alcohol	15 min
3.	85% ethyl alcohol	15 min
4.	95% ethyl alcohol	15 min
5.	Absolute ethyl alcohol	15 min
6.	Absolute ethyl alcohol	15 min
7.	Absolute ethyl alcohol	15 min

B. Infiltration

1.	Propylene oxide (PO)	10 min

2.	Propylene oxide	10 min
3.	Propylene oxide and resin in 50:50 ratio*	30 min minimum - overnight if possible

C. Embedding

1. Drain off PO-resin mixture
2. Cover sections with complete resin mixture and place in vacuum chamber
3. Draw a maximum vacuum until no bubbles are seen emanating from the tissue.
4. Place tissue in molds and add fresh resin with a minimum of bubbles.
5. Place molds in 45°C overnight. This is a *minimum cure time* and longer (several days) is recommended.

* The resin mixture used in this step should be complete with catalyst and identical to that to be used for embedding.

The plastic block may be rough cut to size after the curing time is completed. In cases where marker burns are used, precision cutting proceeds in 2-4μm sections at top microtome speed through approximately 500 μm. The section thickness is then reduced to 2 μm and cutting is continued for 50 μm. After each 50 μm block is cut a 2 μm section is examined by staining with toluidine blue. When markers are found, the orientation of the entire block is altered in an attempt to cut as nearly parallel to the rows of burns as possible. Once this orientation is established cutting proceeds at a pace dictated by the number and placement of the burns. When multiple burns are placed in the macula, serial sections must be taken. This re-

quires examination of every section cut through the entire width of the macula.

Single burns are cut according to the requirements of the investigator. If the entire developed burn is to be examined, serial sections must be made. If only the diameter or cross sectional damage of the burn is of interest, sections are taken every 20 - 50 μm through the burn until a reduction in the width of the damaged area can be measured using an optical micrometer attached to the examining microscope.

Plastic embedded sections are an adaptation of electron microscopy techniques. In electron microscopy the "stain" is an electron-dense material that is held in varying degrees by the different chemical-organelle interfaces of the cell. In light microscopy, the stain is a dye which may show different colors when it reacts with or adsorbs to the molecules of the cell or tissue. These colors can be altered by various chemicals which are routinely applied prior to staining.

The routine method used by light microscopists is a paraffin embedding technique. The end product of this technique is a slice of tissue with no binding medium, i.e., the paraffin is removed by xylene prior to staining. A fast, vivid stain is usually obtained. However, this may not be the case when plastic embedded sections are adapted to light microscopy. There is no safe way to dissolve the binding epoxy resin while leaving the tissue intact and the presence of this plastic will interfere with nearly all stains used routinely in light microscopy. For instance, staining with hematoxylin (a nuclear stain) requires about 10 min at room temperature when no paraffin

is present. It requires about 14 to 16 hours at 45°C when the sections are embedded in plastic.

Hematoxylin stains nuclear elements blue. The usual counterstain used with hematoxylin is eosin, which stains other cellular elements (i.e., cytoplasm) pink, thus producing a readily observable contrast between cellular elements. Eosin stains the plastic embedding medium, hence Paragon (a combined cytoplasmic-nuclear stain) is used as the counterstain in this case. This stain is used primarily for frozen sections, but has been adapted for use with plastic-embedded tissue in which it produces in a deep pink - almost red-colored cytoplasm. The counterstain is applied by immersing the previously hematoxylin-stained slide in a solution of paragon-borax (50/50) at room temperature for about 5 to 20 seconds. The slide is then washed in water, dried and a cover slip applied.

A staining schedule for Hematoxylin-Paragon:

1.	1% aqueous potassium permanganate	15 min
2.	Rinse well in water	
3.	1% aqueous oxalic acid	3 - 5 min
4.	Rinse well in water	
5.	Overnight in Erlich's Hematoxylin at 45°C	
6.	Rinse well in water	
7.	Differentiate in acid alcohol* until red	
8.	Rinse well in water	
9.	Blue in ammonia water**	
10.	Rinse well in water and dry slowly (air dry or very low heat) to prevent shrinking of the sections	

11. Immerse slide in fresh paragon-borax solution (50/50) at room temperature for 5 - 20 seconds

12. Wash well in water and dry slowly as above

13. Apply cover slip as per convention

* 70% Ethyl Alcohol - 1000 ml
Conc. Hydrochloric Acid - 10 ml

** Tap Water - 1000 ml
28% Ammonium Hydroxide 2 - 3 ml

(2) Retinal Pathology

This section of the report summarizes the findings of the histological studies carried out during the contract year. Two studies on histological evaluation of chronological development of retinal lesions have been completed and are described in detail below. Several other histological evaluations for ongoing projects are mentioned briefly and will be dealt with more fully in future reports as the projects are completed.

The first study on chronological development of retinal lesions involved seven rhesus monkeys (fourteen eyes) which were sacrificed at various intervals ranging from one hour to ninety days following exposure. The purpose of this study was to determine if there is any histological evidence of repair during the 90-day period. One suprathreshold retinal lesion was induced in the macula of each eye of each animal. The laser beam parameters were the same for each exposure: 40 mWatt incident on a corneal image diameter of ~2.5 mm, 500 msec pulsewidth, 647.1 nm wavelength and 450 μm retinal image diameter. The lesions induced under these conditions averaged ~750 μm in diameter. A fundus photograph of a typical lesion is shown in Figure IV-1a.

A brief description of the appearance of the lesions at various intervals after exposure follows:

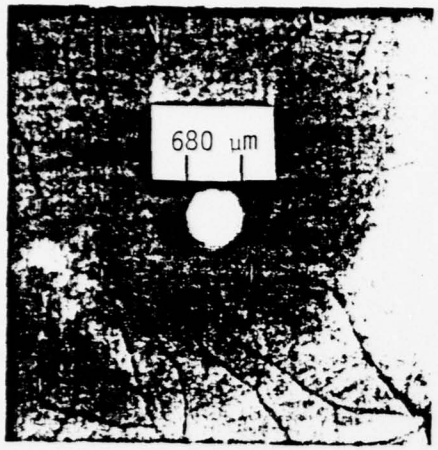
One hour (Figure IV-1b): An annulus of damage was observed in the pigment epithelium (PE) of the retina. The PE was lifted off of the basement membrane to yield a circular area of vacuolation directly above the membrane. Within this annulus, the PE as well as the rods and cones appear to be intact. However, above the center of the annulus there is considerable necrosis of nuclei in the outer nuclear layer resulting in some vacuolation in this layer.

One day (Figure IV-1c): Severe degeneration is found in the outer nuclear and outer molecular layers. The PE and rods and cones still appear to be intact within the annulus of damage.

Seven days (Figure IV-1d): By seven days all of the retinal layers within the circular area of the lesion have begun to disintegrate. This suggests that the apparently intact tissue observed earlier within the annulus of damage was actually dead or dying as a result of the laser exposure. The choriocapillaris is likewise completely obliterated below the retinal lesion. Still, the basement membrane appears to have remained undamaged.

Fourteen days (Figure IV-1e): All retinal layers between the PE and the internal limiting membrane have been destroyed and most of the debris removed. Some large macrophages bearing varying degrees of pigment filled the otherwise void retinal area.

Thirty days (Figure IV-1f): Similar to fourteen days but a "plaque" consisting of macrophagic spindle cells (which were first apparent at seven days) has accumulated in the area formerly occupied by the posterior layers of the retina.



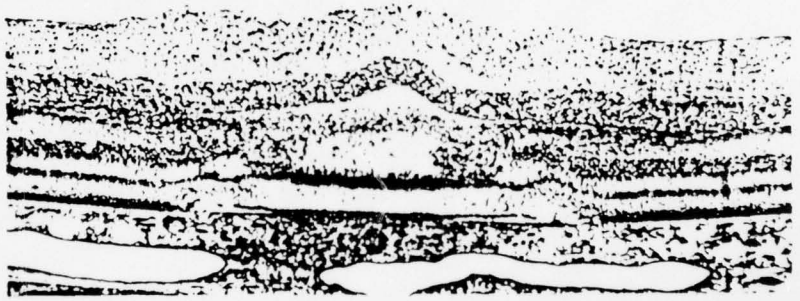
1a. Fundus photograph
(one day post-exposure)



1b. One hour post-exposure (x 69.5).

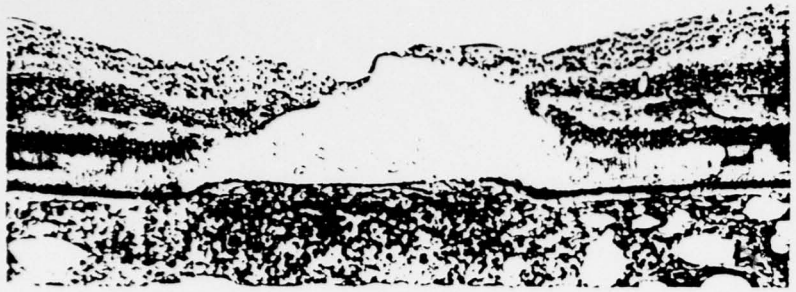
Laser Beam Parameters:

Wavelength - 647.1 nm
Power - 40 mWatt
Pulsewidth - 500 msec
Corneal image diameter - 2.5 mm
Retinal image diameter - 450 µm
Beam divergence (calculated) ~34 mrad

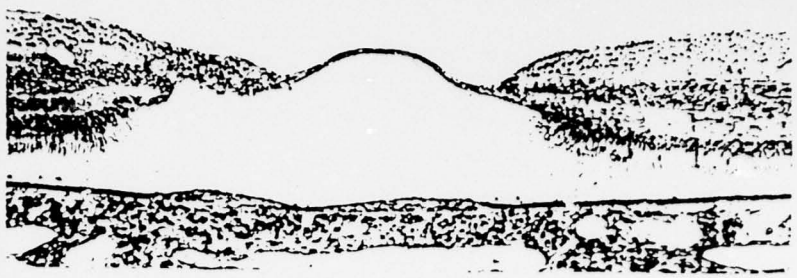


1c. One day post-exposure (x 69.5).

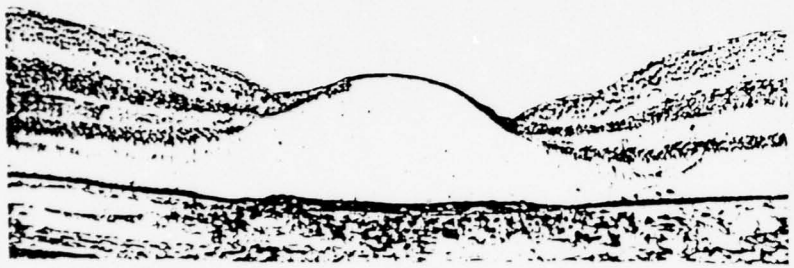
Figure IV-1 Photomicrographs of suprathreshold retinal lesions at various time intervals following exposure.



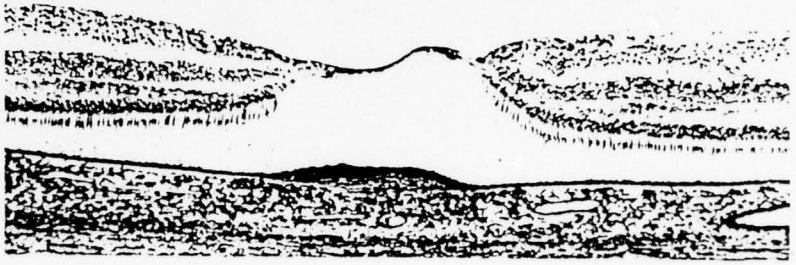
1d. Seven days post-exposure.



1e. Fourteen days post-exposure.



1f. Thirty days post-exposure.



1g. Ninety days post-exposure.

Figure IV-1 (continued) Photomicrographs of suprathreshold retinal lesions at various time intervals following exposure (all X 69.5).

Ninety days (Figure IV-1g): There is still a large area (450 μm diameter) of complete loss of retinal layers. However, this is considerably less than the 700-800 μm areas of damage observed from seven to sixty days post-exposure. Apparently, there has been some regeneration or possibly migration of retinal tissue from the surrounding area.

The reasons for the annular appearance of the damage at one hour and one day after exposure are not understood at this time. However, it is clear that the apparently intact retinal tissue within the annulus must have been severely traumatized by the laser exposure since this tissue eventually disintegrates and is disposed of. The disintegration of all retinal layers is virtually complete by fourteen days, after which there appears to be a gradual filling-in of the destroyed area, first by macrophages and plaque and, after ninety days, by some regeneration or migration of viable retinal tissue into the area. It would be of interest to determine whether this apparent retinal regeneration continues beyond ninety days.

The second study on chronological development of retinal lesions involved one subject eye. The purpose of this study was to determine if there is any histologically observable development of a minimal visible lesion over a two-hour period. Sixteen suprathreshold exposures were delivered to the macular region of the retina. The laser beam parameters were the same for each exposure: 18mW total power incident on a corneal image diameter of ~2 mm, 40 msec pulsewidth, 647.1 nm wavelength and a minimum retinal spot size. The power was chosen to be 50% above threshold to give reasonable assurance that a lesion would develop at each exposed site. The exposures were made eight minutes apart and the eye was fixed approximately twenty minutes after

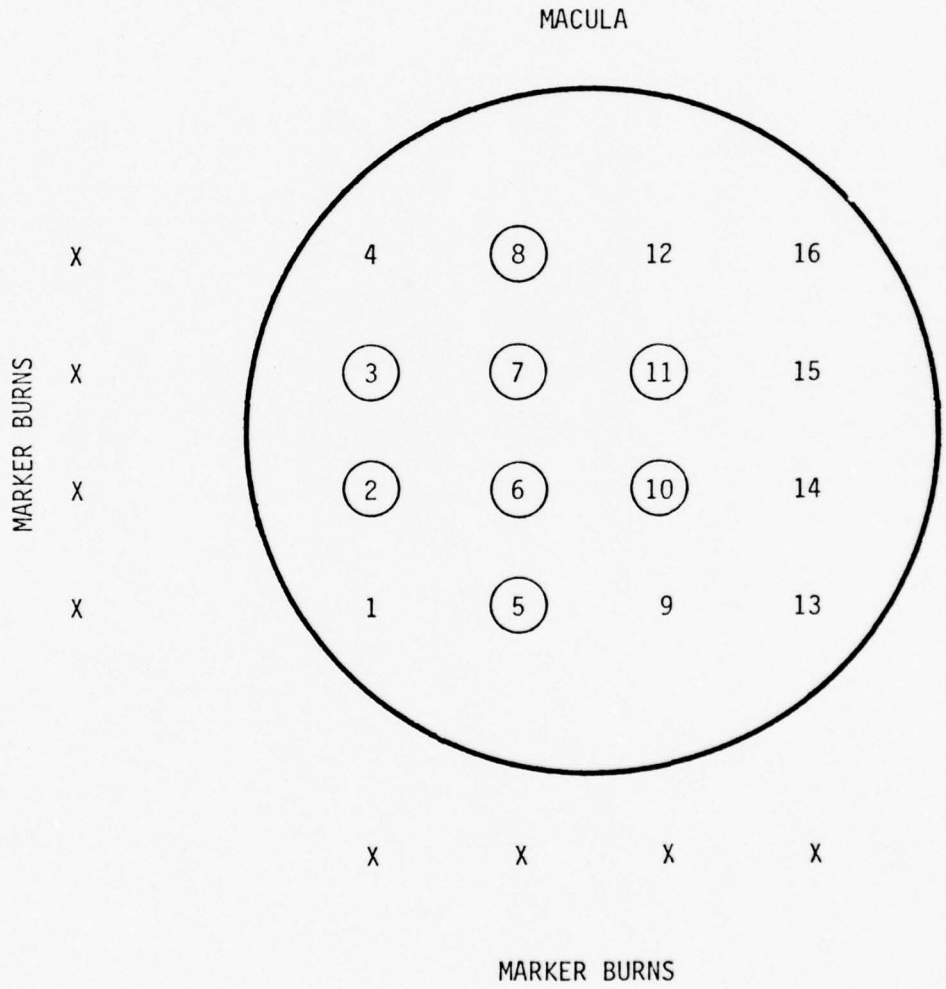
the last exposure. The locations in the macula and the order in which the exposures were delivered are shown in Figure IV-2.

The pathologic report on this eye (left eye, primate 476B) shows that lesions were observed at eight of the sixteen exposure sites. These sites are indicated by the circled numbers in Figure IV-2. It is seen that no lesions were observed at sites 12-16, the last five sites of exposure before fixation. However, lesions were found at all but three of the first eleven exposure sites. Of the three exceptions two are in the bottom row (sites 1 and 9) and may have been obscured by the large marker burns which infringed upon the macular area and the other (site 4) may represent an exposure which went somewhat astray and fell outside of the macula (such a stray lesion was indicated in the pathologist's report).

The results of this experiment suggest a time delay between a threshold exposure and the time at which any morphological lesion becomes observable. In particular, no lesions were observed at the five sites exposed within one hour before fixation. Lesions were found at nearly all of the sites exposed one to two hours before fixation. Unfortunately, it is not possible from the information provided in the pathologic report to discern any systematic time development in the severity of the lesions placed from one to two hours prior to fixation. The first and last exposed sites at which lesions were observable (sites 2 and 11 respectively) had approximately the same size lesions (60 μm) and both are characterized by nuclear pyknosis in the outer nuclear layer and vacuolation of the pigment epithelium. Other lesions at sites exposed between one and two hours before fixation show varying degrees of pyknosis and/or vacuolation and have maximum diameters ranging from

Figure IV-2

Macular Map of Exposure Sites



20 - 60 μm but all of these variations seem random with respect to the age of the lesion.

In conclusion, the results of this experiment suggest that following a threshold exposure there is a period of development of about one hour before any morphological lesion is observable (at the light microscopic level). Between one and two hours there is no obvious criterion by which to judge the stage of development of the lesion. Certainly, it is not possible to draw any definitive conclusions from a study involving a single eye, but the results do indicate that it is possible to monitor the developing pathology in retinal tissue during the first two hours following a threshold exposure. More critical studies of the lesion development (possibly including electron microscopy) could provide detailed information regarding the nature of the damage mechanism(s) involved.

B. CORNEAL LESIONS

(1) Tissue Preparation

The corneas were removed from the anesthetized animal and immediately placed in cold, buffered formalin. The formalin was exchanged twice over a 24-hour period, after which the tissues were processed in a Technicon tissue processor in preparation for paraffin embedding. The procedure consists of infiltrating the tissues with formalin fixative, followed by alcohol, xylene and finally paraffin. Variations of this technique may be found in any standard text on histological laboratory procedure. When embedded and cooled, the paraffin blocks were trimmed and serial sections of 6 μm each were taken.

This procedure was followed because there was no way to determine the precise location of the lesion before microscopic examination. The result was 30 to 40 slides per cornea, with 10 to 15 sections per slide. The sections were batch stained by a routine hematoxylin and eosin procedure and mounted in Permount.

Although the approach described above has produced tissue of an acceptable quality the caliber is not as high as desired, principally because of a problem of tissue hardness. Corneal tissue is essentially avascular, the stroma being composed primarily of fibers arranged in flat lamellae parallel to the surface of the tissue. This stromal layer apparently becomes quite hard during the routine processing and when this tissue is embedded in a softer medium (i.e., paraffin) the cutting procedure results in tissue distortion and damage. The sudden decrease in block resistance to the knife as the cutting edge moves from hardened stromal tissue to paraffin results in the tissue being "dragged" into the softer medium.

The apparent hardness of the stromal tissue and subsequent stromal separation parallel to the fiber layers may be due to the tissue processing technique currently used at USAF SAM/VSP. However, a tissue processing technique which purports not to harden tissue has been adapted from the Manual of Histologic Staining Methods of the Armed Forces Institute of Pathology.[1] The efficacy of this method for future histological investigations is currently being evaluated.

(2) Corneal Pathology

A pathologic report has been received on a rhesus subject (no. 920B)

whose corneas were exposed to the krypton laser 18 hours prior to sacrifice. The right eye which received a dose of 70 J/cm^2 in 45 sec showed some disruption of all corneal epithelial layers with necrosis more pronounced in the middle and basal layers (Figure IV-3). The left eye which received a dose of 90 J/cm^2 in 45 sec showed more serious damage in the form of a separation of the epithelium into two layers with severe necrosis of the middle layers. In contrast, the surface layer appeared largely intact even though it was separated from the lower layers by approximately 100 μm (Figure IV-4).

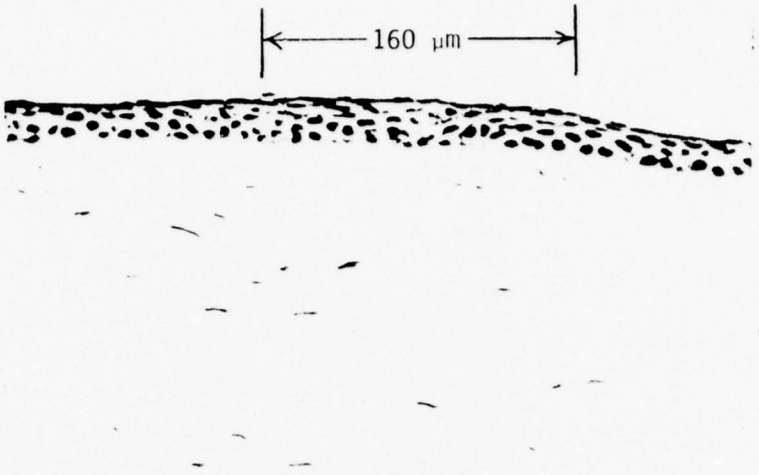


Figure IV-3. Photomicrograph (280x) of rhesus cornea 18 hours after exposure to UV laser radiation (350 nm) at 20.6 mW for 45 sec (total dose 70 J/cm^2). (Primate 920B, right eye).

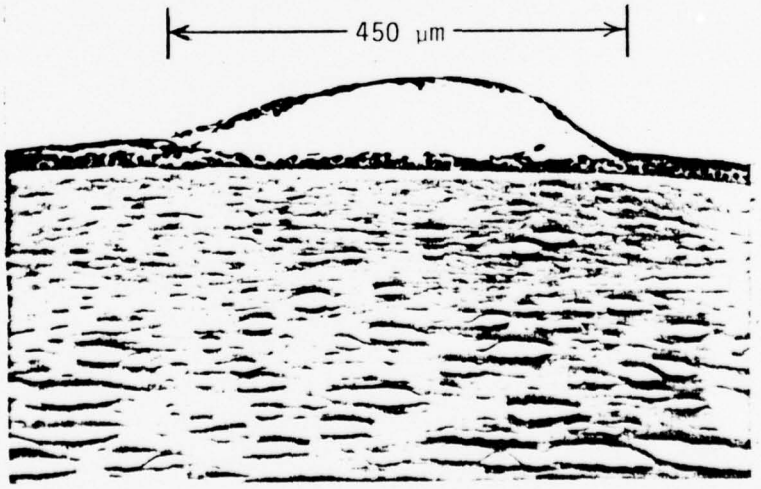


Figure IV-4. Photomicrograph (148x) of rhesus cornea 18 hours after exposure to UV laser radiation (350 nm) at 26.5 mW for 45 sec (total dose 90 J/cm^2). (Primate 920B, left eye).

REFERENCES

1. "Manual of Histologic Staining Methods of the Armed Forces Institute of Pathology," Third Edition (L.G. Luna, ed.) McGraw-Hill, New York (1968).

PART V

WAVELENGTH DEPENDENCE OF RETINAL DAMAGE INDUCED BY VISIBLE LASER RADIATION

V.E. Sanders and H.W. Hemstreet, Jr.

A. INTRODUCTION

The literature on retinal threshold measurements in rhesus monkeys from laser beam exposures at visible wavelengths is extensive. Previous investigations have covered retinal threshold measurements performed with a variety of lasers operating at different wavelengths, various lasing modes and beam divergences, and with both Q-switched and CW laser pulses.

However, there is also a considerable variation in the data, posing the question whether wavelength dependence plays a significant role in laser burn thresholds. For example retinal theshold measurements at 1064 nm are several times greater than thresholds in the visible spectrum, pointing to a significant wavelength effect. In this case the principal variations can be explained on the basis of the markedly higher absorption coefficients of the anterior ocular media in the near IR as opposed to the visible region. There is also some variation in absorption coefficients within the visible spectrum. However, as pointed out in earlier reports,[1,2] the principal wavelength dependent term which governs temperature increases in the retina and hence threshold levels is expressed as $\alpha T_o \exp[-\alpha z]$, where α is the pigment epithelium (PE) absorption coefficient (cm^{-1}), T_o is the transmittance of the ocular media anterior to the PE, and z is the optical path (cm) through the PE. Although both α and T_o are wavelength dependent, the product of these terms shows little variation across the visible spectrum.

This small variation predicted theoretically was essentially substantiated by a series of experimental determinations of "worst case" (i.e., minimal laser spot size) retinal damage thresholds in rhesus monkeys for single pulse exposures (40 ms) at four wavelengths: 647.1 nm, 568.2 nm, 520.8 nm and 476.2 nm.[1] Although experimental results showed some variations in worst case ED50 thresholds for these wavelengths, the variations were small compared to the magnitude of the 95% confidence intervals calculated in each case. Therefore, these variations could be attributed to random fluctuations in experimental parameters, such as minimal retinal spot size, which masked out any actual wavelength dependence.

In an effort to eliminate possible fluctuations in the retinal spot size, a second series of wavelength dependent threshold experiments was undertaken. These experiments were designed to produce fixed, large spot sizes on the retina so that thresholds for each of the four wavelengths could be measured for known retinal irradiance ($W\ cm^{-2}$). This series of experiments, begun during the period of previous annual report,[2] was completed during the past year and the final results are reported here.

The experimental results are expressed in terms of maximum threshold variation as a function of wavelength and are compared with calculated peak retinal temperatures as predicted by two different theoretical models.

B. EXPERIMENTAL PROCEDURES

The second set of wavelength dependent threshold measurements using

a large, measurable retinal spot size was completed. The image radius on the macula for each exposure was fixed at 140 μm. In order to compensate for the lower retinal irradiance as compared with minimal spot sizes, the exposure time was increased from 40 msec to 250 msec in order to provide sufficient laser energy at each wavelength to produce lesions.

The apparatus used in the experiment is shown schematically in Figures V-1 and V-2. A Spectra-Physics Model 164 Krypton gas laser, operating in the TEM_{00} mode, was used as the irradiation source. This unit is readily tunable to the four visible wavelengths employed: 647.1 nm, 568.2 nm, 520.8 nm and 476.2 nm. A beam scan of the laser output was recorded using an EG&G - SGD100A photodiode mounted behind a 50 μm pinhole and attached to a micrometer translation stage driven by a synchronous motor. The pinhole and photodiode were driven across the center of the beam at a uniform rate and the output was displayed on an X-Y recorder. Typical beam profiles are shown in Figures V-3 and V-4. The former shows a cross-section of the beam at the corneal plane without the intervening lens shown in Figure V-2. The latter is a cross-section of the beam at the cornea with the lens in place. The purpose of the lens is to increase the divergence of the beam entering the eye and thus produce a large image size on the retina. As seen in Figure V-4, the lens does not alter the Gaussian profile of the incident beam.

Total laser power was continuously monitored as shown in Figure V-1 by reflecting a small fraction of the beam onto an EG&G - SGD444 photodiode coupled to a Tektronix Model 556 Oscilloscope. The photodiode was calibrated daily against a Scientech Model 3600 thermopile placed in the output beam at the intended position of the subject's eye. Thus, the photodiode output (in

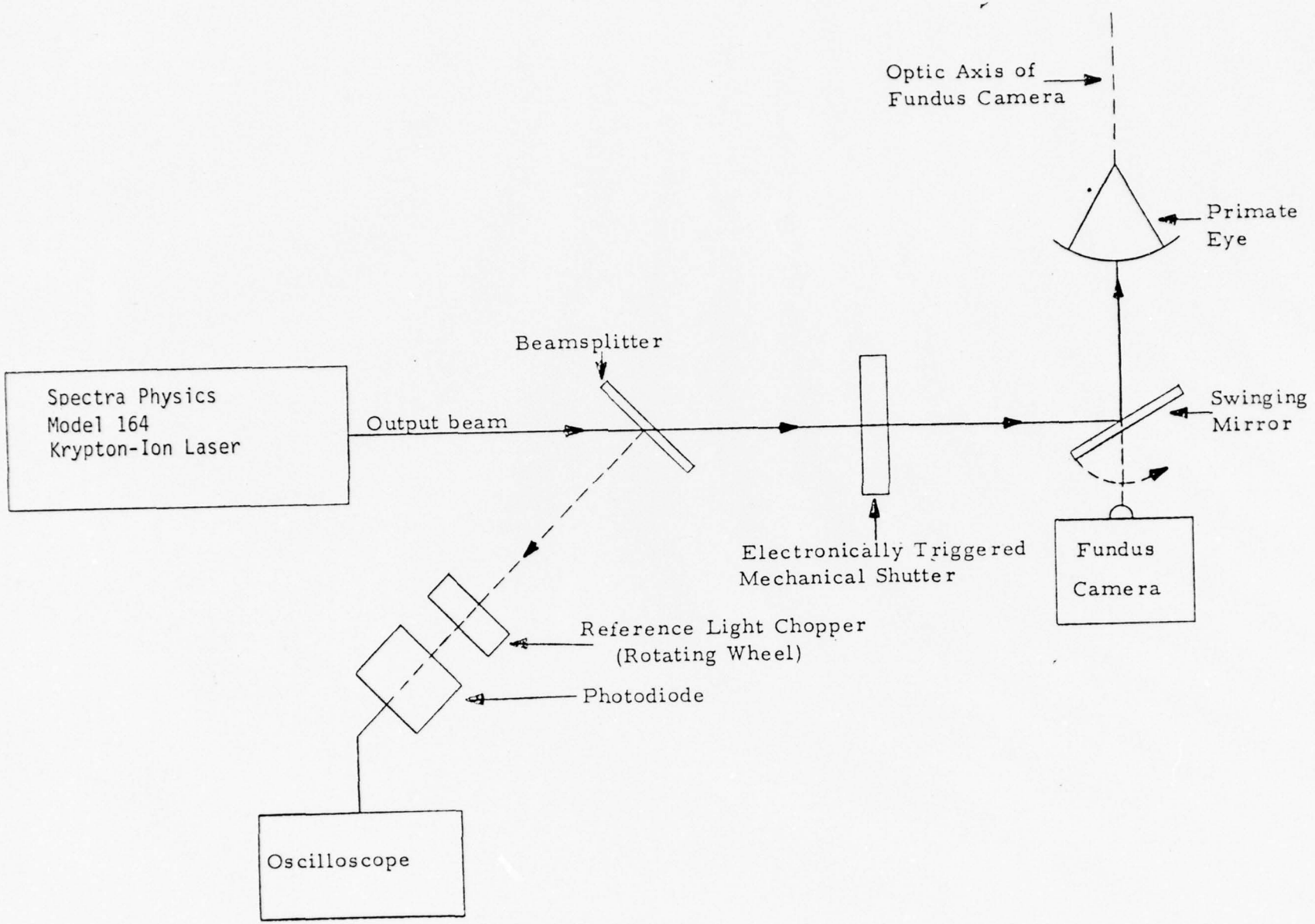


Figure V-1. Block Diagram of Experimental Apparatus for Retinal Irradiations

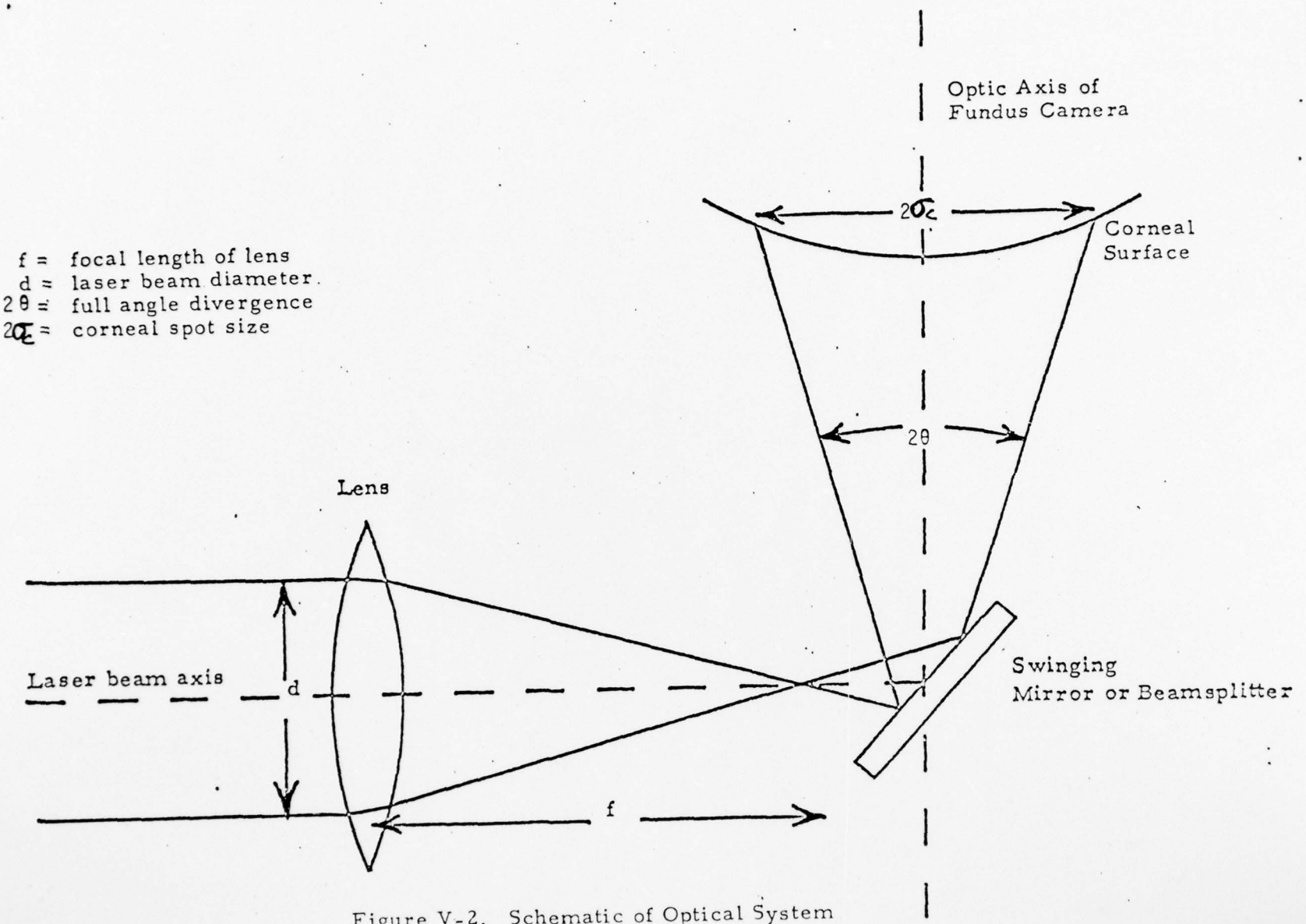
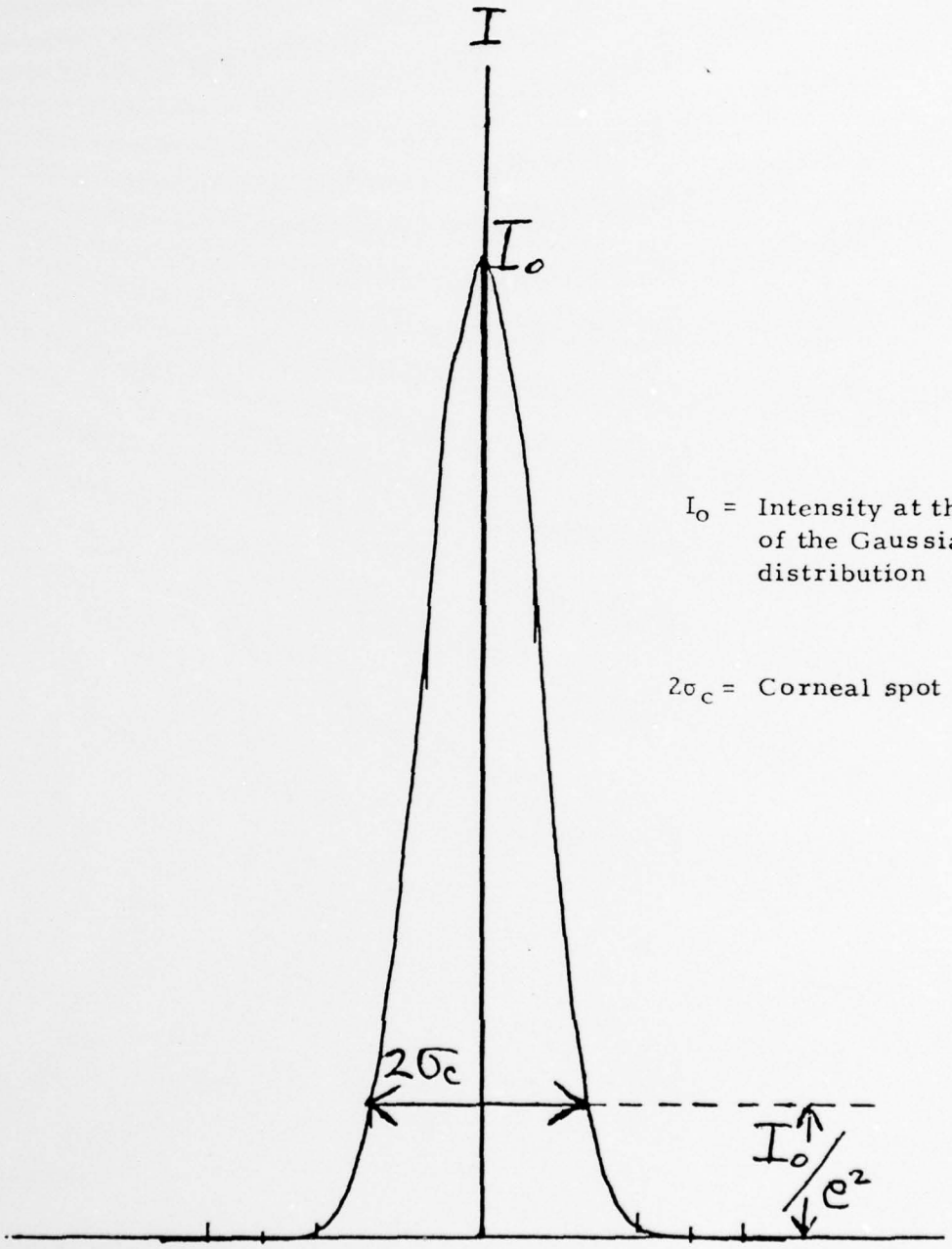


Figure V-2. Schematic of Optical System for Large Retinal Image Sizes



I_o = Intensity at the center of the Gaussian field distribution

$2\sigma_c$ = Corneal spot size

Figure V-3. Spatial Distribution of Undiverged Laser Beam

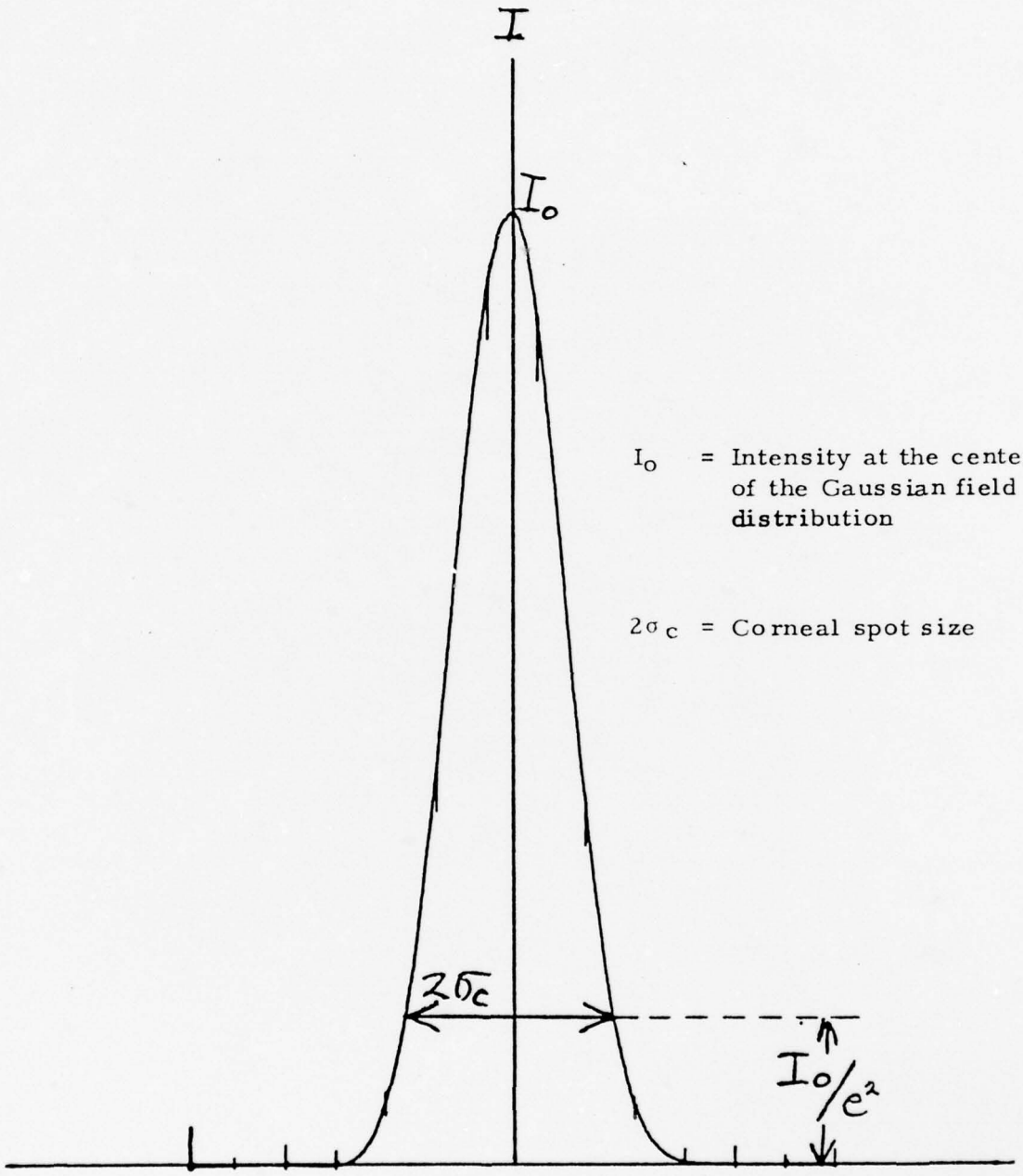


Figure V-4. Spatial Distribution of Laser Beam Diverged through a Positive Lens

volts) as read on the oscilloscope was directly convertible to total corneal beam power (in milliwatts).

A Zeiss fundus camera was used to view the subject's retina and to hold the front-surface mirror used to deflect the laser pulse into the subject's eye. The mirror was swung out of place after each exposure so that the retina could be viewed. When in place, its position and orientation were adjusted so that the reflected beam was coaxial with the fundus camera optics and its ocular crosshairs. With this apparatus a given macular site could be precisely selected to receive an exposure pulse.

In addition the fundus camera was fitted with a measuring reticle located directly behind the camera eyepiece. One division on the reticle corresponded to a linear dimension of 50 μm in the retinal (PE) plane.[2] This value was determined by calibrating the reticle with respect to a double-tipped probe (Figure V-5) surgically implanted in the PE. The distance between probe tips was fixed at 1 mm. Thus, when the implanted probe was viewed through the eye and the fundus camera, the distance between tips corresponded to 20 reticle divisions, based on measurements through six different eyes.

The large retinal image size was produced by simply increasing the laser beam divergence with a positive lens as shown schematically in Figure V-2. The magnitude of the divergence is evidently a simple function of lens power; and thus, for a given lens, the beam diameter at the corneal plane is a function of the distance from lens to cornea. By a trial and error procedure with ophthalmic trial lenses placed at various distances from the cornea, the proper combination was selected to produce a retinal spot radius of 140 μm

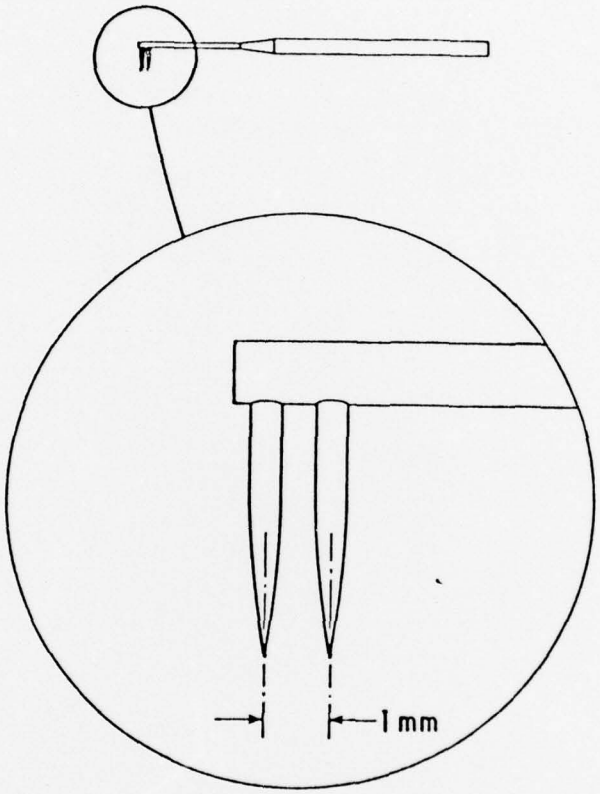


Figure V-5. CALIBRATED PROBE

with a corneal image diameter of 2.5 to 3.0 mm. Although it is possible to calculate the approximate lens power required to produce the desired retinal spot, the actual lens used was based on a direct measurement of retinal image size using the calibrated reticle. This was accomplished by replacing the front surface mirror with a beam splitter of equal dimensions so that the retinal image of a sub-threshold laser beam could be measured visually through the fundus camera. After the proper lens and distance had been determined, the beam splitter was replaced by the mirror to induce retinal lesions.

It should be noted that since the retinal image has an assumed Gaussian radial intensity distribution, measurement of the beam radius by visual observation is decidedly subjective. Thus, in order to arrive at a consistant $1/e^2$ radius, the measurements for all the eyes were performed by the same observer.

The ED50 threshold for each wavelength was calculated by a probit method using burn/no burn data from 18 exposed eyes. The macula of each eye was irradiated with 14 single-pulse (250 ms) exposures at pre-selected sites as shown in Figure V-6. The exposure powers were arranged on a log dosage scale extending above and below an estimated threshold value such that the lowest power would not produce a lesion, and the highest power would always produce a lesion. These 14 exposures were delivered to the eye in a randomized power sequence.

The occurrence of a lesion was determined ophthalmoscopically one hour after exposure. A lesion was defined to be any white or gray discoloration surrounded by a black or dark gray ring.

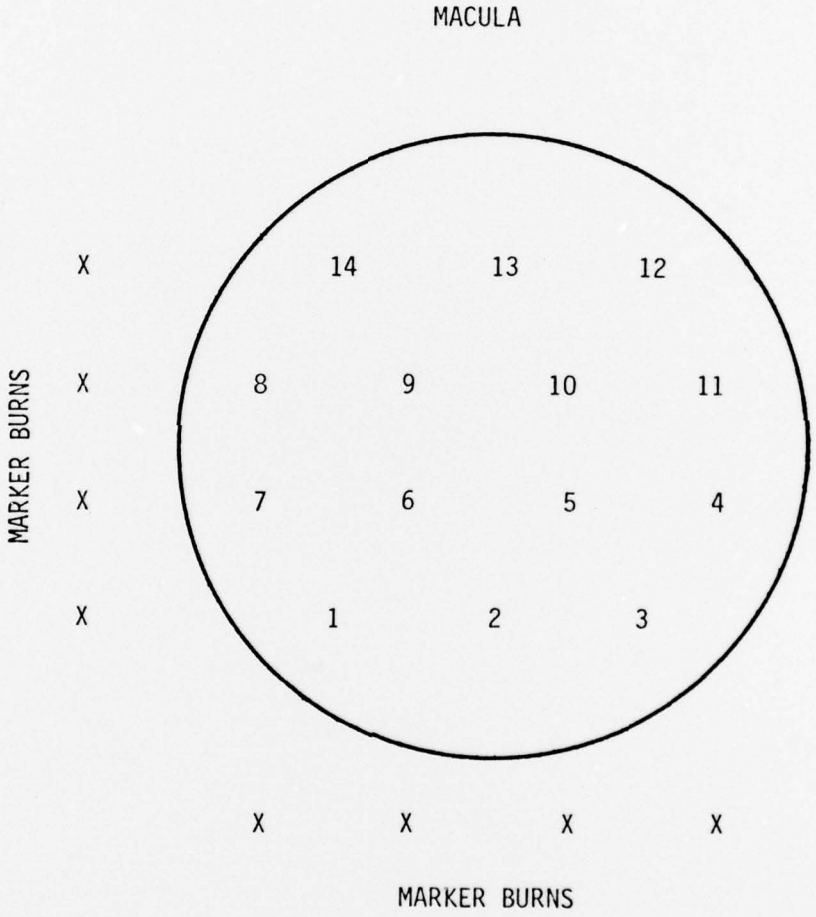


Figure V-6. Exposure Placement in Macula.

C. SUBJECT PREPARATION AND HANDLING

The following sequence describes the chronology of events constituting the clinical preparation and handling of each rhesus monkey before, during, and after the ocular exposure to laser radiation:

1. Each subject's eyes were refracted to the nearest .25 diopter in each meridian. An eye with a greater than .50 diopter refractive error in any meridian was not used in the experiment.
2. An intra-muscular injection of .05 cc (per kilogram weight of the subject) of ketamine hydrochloride (Ketylar), 100 mg/ml, was given prior to the administration of other anesthetic agents.
3. The pupil of each eye was dilated to a maximum (7 mm) by the application of two drops of (1%) tropicamide (Mydriacyl) to the cornea. This application was repeated after five minutes.
4. The dilation process was followed by a retro-bulbar injection of 0.6 cc of lidocaine hydrochloride (2%).
5. An intra-catheter was placed in a saphenous vein for periodic injection of .5 - 1.0 cc/kg of sodium pentobarbital (Nembutal) 50 mg/ml.
6. Sutures were placed in the upper eye lid to facilitate holding the eye lid open during the irradiation process.
7. During the period of exposure the subject's body temperature was monitored and maintained at a temperature of 36 $\pm$ 1^{o}C.
8. Corneal drying during the period of exposure was prevented by periodic application of normal saline to the corneal surface and by manually blinking the bottom eye lid.

9. After the laser exposure and the determination of induced visible lesions, two drops of 1% methyl-cellulose were placed in each eye before the subject was returned to the vivarium.

These subjects ranged in weight from two to four kilograms and in age from two to three years. No distinction is considered or discrimination made between the eyes of male and female subjects.

These animals were maintained and the experiments conducted in accordance with procedures outlines in "Guide for Laboratory Animal Facilities and Care", National Academy of Sciences-National Research Council, and USAF/SAM Regulation 169-2, 6 February 1974.

D. RESULTS AND DISCUSSION

The results of the experimental measurements at all four wavelengths for a 140 μm retinal spot radius are summarized in Table V-1, which lists the calculated ED50 thresholds as well as the lower 95% confidence limit, the 95% confidence interval and the standard deviation for the groups of 18 eyes exposed at each wavelength. For comparision, the bottom half of the table contains a similar summary of the earlier study of wavelength dependence using "worst case" (i.e., minimal image) retinal exposures. These data represent the results of statistical analyses on the raw data.

In comparing the two sets of results, it should first be noted that the standard deviations at each wavelength for the large spot exposures are consistently smaller than those for the minimal image exposures. This smaller variance among the thresholds for each eye in a group indicates that the

TABLE V-1

Summary of Experimental Results

140 μm Retinal Image Radius, 250 ms Exposure

Wavelength (nm)	476.1	520.8	568.2	647.1
ED50 (mW)	35.5	37.7	36.1	38.6
95% Confidence Interval (mW)	33.4 – 37.6	35.9 – 39.6	34.9 – 37.2	37.8 – 39.4
Lower 95% CL (mW)	33.8	36.2	35.1	38.0
Standard Deviation (log units)	.0533	.0428	.0281	.0175

Minimal Retinal Image, 40 ms Exposure

Wavelength (nm)	476.1	520.8	568.2	647.1
ED50 (mW)	11.9	10.5	11.5	12.0
95% Confidence Interval (mW)	10.8 – 13.2	9.7 – 11.4	10.5 – 12.6	10.7 – 13.5
Lower 95% CL (mW)	11.0	9.8	10.7	11.0
Standard Deviation (log units)	.0899	.0709	.0772	.1005

relative magnitude of random fluctuations was less severe in the case of the large retinal image exposures. Presumably this is due to the essentially constant retinal image size for each wavelength and each set of exposed eyes. In the minimal image exposures it was not feasible to measure or control retinal image size, and it can be assumed that there were significant random fluctuations in retinal image sizes over the range of wavelengths and exposed eyes.

Both sets of ED50 thresholds from Table V-1 are plotted against wavelength in Figure V-7. The vertical bar through each threshold point is the magnitude of its 95% confidence interval, which represents the range within which the ED50 thresholds for 95% of the sample population would be expected to fall.

The minimal retinal image data show quite clearly that there is no significant wavelength dependence within the range of visible wavelengths employed. Similarly there is no significant trend in the 140 μm retinal image data. Thus, from the results of both sets of experiments, it is evident that retinal burn thresholds for visible laser radiation are essentially independent of wavelength.

This conclusion is consistent with computer calculations using both the TI[3] and IITRI[4] thermal models; i.e., both predict only small changes in induced retinal temperatures for variation of laser wavelengths across the visible spectrum. The parameters used in these experimental studies along with available measured values of ocular transmittances and absorption coefficients[5] were input to both computer programs. The outputs from

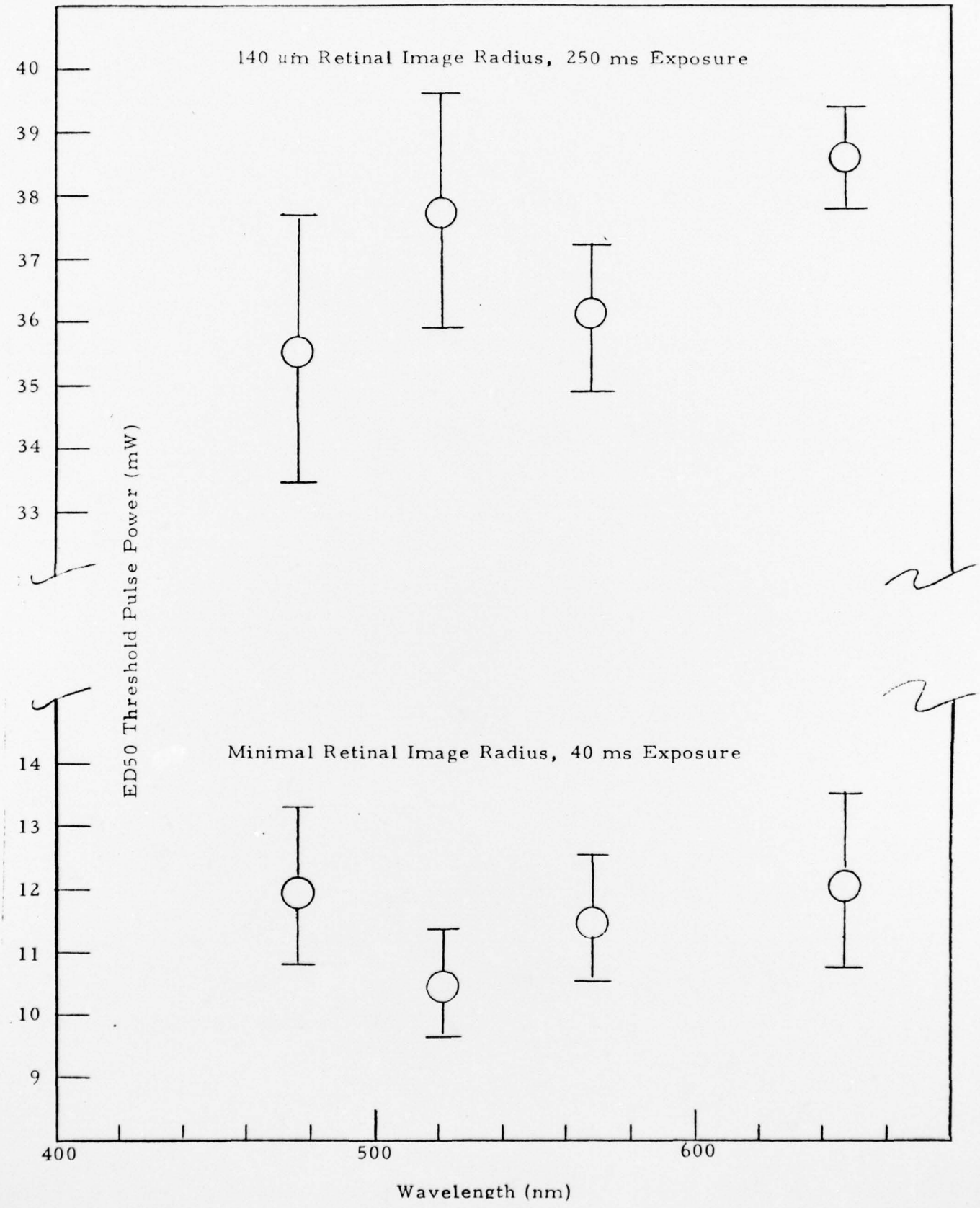


Figure V-7. ED50 Retinal Thresholds at Four Visible Wavelengths

these programs consist of tabulated temperature increases in the chorioretinal region as a function of space and time during and after a given exposure pulse.

Figure V-8 shows the retinal temperatures predicted by the TI model for the same exposure times, retinal image radii and wavelengths used in the experimental measurements. The peak temperatures are expressed degrees per mW of laser power at the cornea. In this model, the peak temperatures in the PE occur typically at a depth of 3 μm at the center of the laser image (R = 0, Z = 3μ). As shown in Figure V-8, the TI model predicts a small but distinct monotonic increase in peak temperature with increasing wavelength.

Current theories of thermal damage mechanisms hold that damage thresholds are closely related to the peak temperature increases. Thus the results of these TI model calculations predict a monotonic decrease in threshold with increasing wavelength. Assuming that the threshold is approximately inversely proportional to the peak temperature, then the threshold at 476.1 nm is predicted to be 20% higher than at 647.1 nm, for 140 μm retinal image radii and 250 ms exposures. Similarly, for a 25 μm retinal image radius and 40 ms exposures, the predicted threshold increase is about 16%.

The more advanced IITRI thermal model is capable of predicting both the temperature distributions and laser powers required to produce irreversible damage. Parameters representative of the large retinal image (140 μm) experiments together with the same values of ocular transmittance and retinal absorption used above were input to the IITRI program.

Table V-2 presents selected temperature increases at four locations in the PE for the four wavelengths predicted by the IITRI model. Calculated

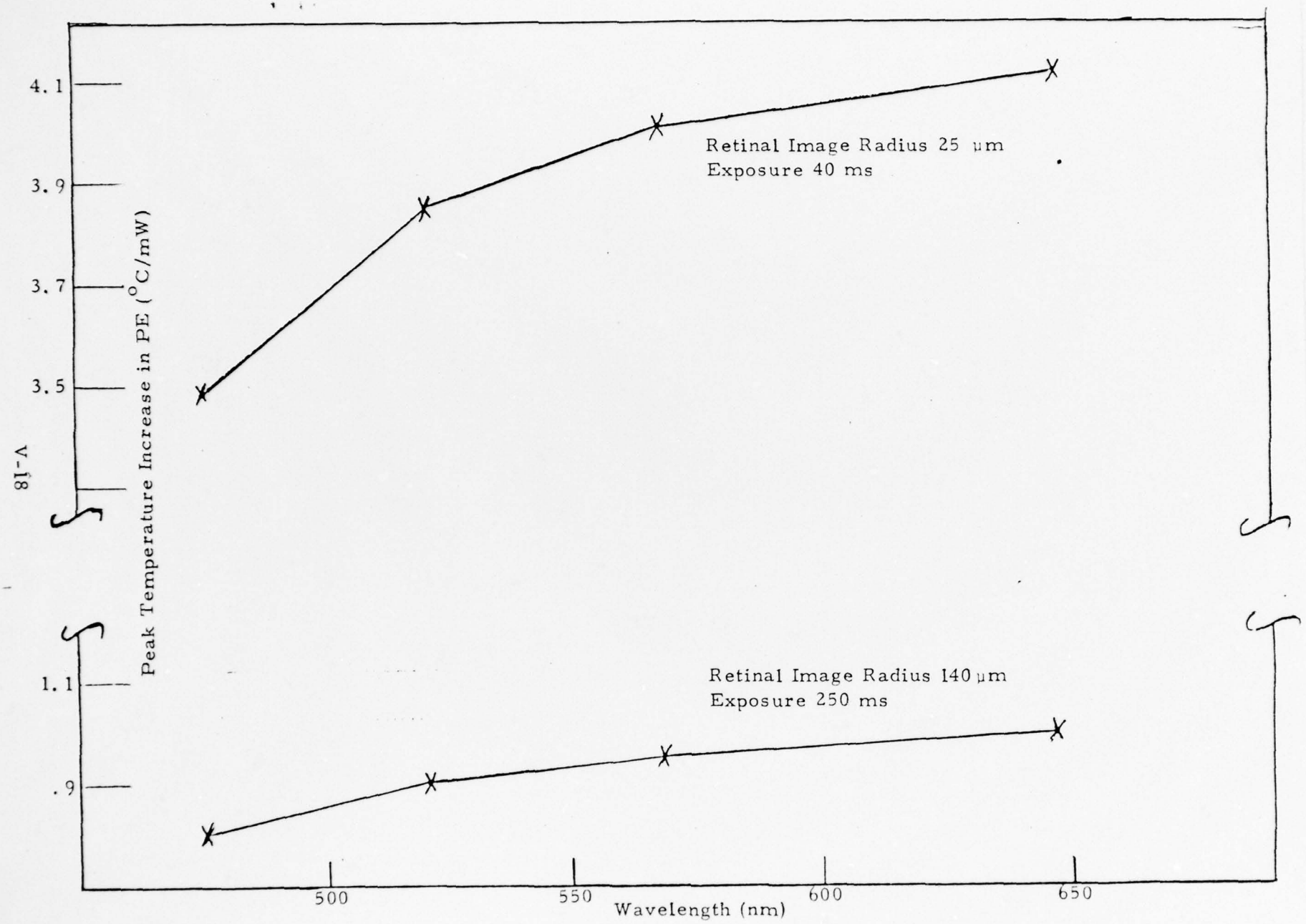


Figure V-8. Predicted Temperature Increase in Pigment Epithelium (TI Model)

TABLE V-2

Summary of IITRI Model Predictions

35 mW Beam Power, 140 μm Retinal Image Radius,
250 ms Exposure

Temperature Increase in PE (°C)

Wavelength (nm)→	647.1		568.2		520.8		476.1	
Depth in PE↓	R=0	R=50μm	R=0	R=50μm	R=0	R=50μm	R=0	R=50μm
z=6 μm	44.8	35.7	45.2	36.0	45.1	36.0	43.5	34.6
z=18 μm	37.8	30.3	37.8	30.4	37.6	30.2	36.2	29.0

Laser Power Required to Produce Damage at Center
of 140 μm Retinal Image (R = 0)

Wavelength (nm)	647.1	568.2	520.8	476.1
Laser Power (mW)	18.7	18.5	18.6	19.3

peak temperatures occur at a depth of 6 μm in the PE (Z = 6 μm) at the center of the retinal image (R = 0). These temperatures represent the increments induced by a fixed laser beam power of 35 mW and were not normalized to power as in the TI model. However, the precise magnitudes of the calculated temperatures are of less interest than the predicted trend as a function of wavelength. In this case the calculated peak temperature is not a monotonic function of wavelength. Rather the predicted temperatures are essentially constant, varying by only 4% from highest to lowest over this wavelength range. Similarly, the increase in beam power required to cause irreversible damage at the center of the 140 μm retinal image is also ~4%.

Referring to the experimental ED50 threshold values for the large retinal exposures (Table V-1 and Figure V-7), it is seen that the percentage increase from the lowest to highest threshold over the wavelength range is approximately 9%, in close agreement with the magnitude of variation predicted by the IITRI model. The functional dependence on wavelength of powers to produce minimum lesions (bottom of Table V-2) does not follow the pattern observed experimentally. However, these insignificant differences can be understood on the basis of the experimental errors in ocular transmission and retinal absorption measurements.

In summary, we have observed no significant wavelength dependence of retinal damage thresholds, either for minimal or large (140 μm) retinal images. These observations are consistent with predictions made using the IITRI thermal model.

REFERENCES

1. "Research on the Eye Effects of Laser Radiation", Technology Incorporated, Third Quarterly Report, Contract F41609-73-C-0017, USAF School of Aerospace Medicine, Brooks AFB, Texas (November 1973).

2. "Research on the Eye Effects of Laser Radiation", Technology Incorporated, Annual Report No. 1, Contract F41609-73-C-0017, USAF School of Aerospace Medicine, Brooks AFB, Texas (March 1974).

3. White, T.J., et al., "Model for Prediction of Retinal Temperatures", Technology Incorporated, Final Report, Contract F41609-68-C-0023, USAF School of Aerospace Medicine, Brooks AFB, Texas (November 1969).

4. Takata, A.N., et al., "Thermal Model of Laser-Induced Eye Damage", Illinois Institute of Technology Research Institute, Final Technical Report, Contract F41609-74-C-0005, USAF School of Aerospace Medicine, Brooks AFB, Texas (October 1974).

5. Coogan, P.S., W.F. Hughes and J.A. Mollsen, "Histologic and Spectrophotometric Comparisons of the Human and Rhesus Monkey Retina and Pigmented Ocular Fundus", Final Report, Contract F41609-71-C-0006, USAF School of Aerospace Medicine, Brooks AFB, Texas (January 1974).